

University of Windsor

Scholarship at UWindor

Electronic Theses and Dissertations

Theses, Dissertations, and Major Papers

2008

Numerical model development of a heavy mining vehicle multi-piece wheel assembly for structural analysis

Vivek Vijayan
University of Windsor

Follow this and additional works at: <https://scholar.uwindsor.ca/etd>

Recommended Citation

Vijayan, Vivek, "Numerical model development of a heavy mining vehicle multi-piece wheel assembly for structural analysis" (2008). *Electronic Theses and Dissertations*. 8053.

<https://scholar.uwindsor.ca/etd/8053>

This online database contains the full-text of PhD dissertations and Masters' theses of University of Windsor students from 1954 forward. These documents are made available for personal study and research purposes only, in accordance with the Canadian Copyright Act and the Creative Commons license—CC BY-NC-ND (Attribution, Non-Commercial, No Derivative Works). Under this license, works must always be attributed to the copyright holder (original author), cannot be used for any commercial purposes, and may not be altered. Any other use would require the permission of the copyright holder. Students may inquire about withdrawing their dissertation and/or thesis from this database. For additional inquiries, please contact the repository administrator via email (scholarship@uwindsor.ca) or by telephone at 519-253-3000ext. 3208.

**Numerical model development of a heavy mining
vehicle multi-piece wheel assembly for structural
analysis**

**by
Vivek Vijayan**

A Thesis

Submitted to the Faculty of Graduate Studies
through Mechanical, Automotive, and Materials Engineering
in Partial Fulfillment of the Requirements for
the Degree of Master of Applied Science at the
University of Windsor

Windsor, Ontario, Canada

2008

© 2008 Vivek Vijayan



Library and Archives
Canada

Published Heritage
Branch

395 Wellington Street
Ottawa ON K1A 0N4
Canada

Bibliothèque et
Archives Canada

Direction du
Patrimoine de l'édition

395, rue Wellington
Ottawa ON K1A 0N4
Canada

Your file *Votre référence*
ISBN: 978-0-494-82080-3
Our file *Notre référence*
ISBN: 978-0-494-82080-3

NOTICE:

The author has granted a non-exclusive license allowing Library and Archives Canada to reproduce, publish, archive, preserve, conserve, communicate to the public by telecommunication or on the Internet, loan, distribute and sell theses worldwide, for commercial or non-commercial purposes, in microform, paper, electronic and/or any other formats.

The author retains copyright ownership and moral rights in this thesis. Neither the thesis nor substantial extracts from it may be printed or otherwise reproduced without the author's permission.

In compliance with the Canadian Privacy Act some supporting forms may have been removed from this thesis.

While these forms may be included in the document page count, their removal does not represent any loss of content from the thesis.

AVIS:

L'auteur a accordé une licence non exclusive permettant à la Bibliothèque et Archives Canada de reproduire, publier, archiver, sauvegarder, conserver, transmettre au public par télécommunication ou par l'Internet, prêter, distribuer et vendre des thèses partout dans le monde, à des fins commerciales ou autres, sur support microforme, papier, électronique et/ou autres formats.

L'auteur conserve la propriété du droit d'auteur et des droits moraux qui protègent cette thèse. Ni la thèse ni des extraits substantiels de celle-ci ne doivent être imprimés ou autrement reproduits sans son autorisation.

Conformément à la loi canadienne sur la protection de la vie privée, quelques formulaires secondaires ont été enlevés de cette thèse.

Bien que ces formulaires aient inclus dans la pagination, il n'y aura aucun contenu manquant.


Canada

AUTHOR'S DECLARATION OF ORIGINALITY

I hereby certify that I am the sole author of this thesis and that no part of this thesis has been published or submitted for publication.

I certify that, to the best of my knowledge, my thesis does not infringe upon anyone's copyright nor violate any proprietary rights and that any ideas, techniques, quotations, or any other material from the work of other people included in my thesis, published or otherwise, are fully acknowledged in accordance with the standard referencing practices. Furthermore, to the extent that I have included copyrighted material that surpasses the bounds of fair dealing within the meaning of the Canada Copyright Act, I certify that I have obtained a written permission from the copyright owner(s) to include such material(s) in my thesis and have included copies of such copyright clearances to my appendix.

I declare that this is a true copy of my thesis, including any final revisions, as approved by my thesis committee and the Graduate Studies office, and that this thesis has not been submitted for a higher degree to any other University or Institution.

ABSTRACT

Over the past few decades, a significant number of incidents and fatalities have been associated with mining vehicle wheels. Correspondingly, a literature review was completed dealing with various topics associated with the mining wheels with specific attention to the incidents arising as a result of servicing multi-piece wheels. A detailed analysis of the obtained data indicated that three piece mining vehicle wheels were found to be most commonly involved in such incidents.

To assess the mechanical performance of three piece mining wheels, experimental testing was completed on such a wheel. Additionally, a numerical model of the wheel assembly used in the experimental testing was developed and simulated under similar loading conditions as in the experimental work. Predictions of the finite element model were in good agreement to the experimental findings with percentage errors typically in the range of 10% to 20%.

Numerical simulation of the SAE J1992 wheel cornering fatigue testing condition was completed on the numerical model of the wheel. The predictions from simulation were used to assess fatigue factors of safety utilizing the modified Goodman theory (von Mises and Sines approaches), simplified damage mechanics and critical plane approaches considering multi-axial loading. This predicts an infinite life for the wheel, whereas in practical applications, it is observed that the wheels do not usually have an infinite life as predicted. This contradiction in the numerical prediction is attributed to the wear and degradation of the mining wheel as a result of environmental effects and localized damage imparted onto a mining wheel during operation.

ACKNOWLEDGEMENTS

First of all, I would like to thank my academic supervisor, Dr. William Altenhof for his time, technical support and guidance all through the research. I would also like to thank Dr. Nader Zamani and Dr. Sreekantha Das for the knowledge they shared with me throughout my degree.

I am also grateful to Mr. Richard Banting from MASHA, who has given me insights into the project, and Mr. Patrick Skeldoch from J & M tires who has provided me with the three piece mining wheel for experimentation. I would also like to thank North Shore Industrial for providing me with CAD data of the wheel.

With regards to experimentation, I would like to acknowledge the support of Mr. Andy Jenner, Mr. Lucian Pop, Mr. Patrick Seguin and Mr. Neil Turton.

Finally, the financial assistance provided by WS&IB is greatly appreciated.

TABLE OF CONTENTS

AUTHOR’S DECLARATION OF ORIGINALITY	iii
ABSTRACT.....	iv
ACKNOWLEDGEMENTS	v
LIST OF TABLES	x
LIST OF FIGURES	xi
NOMENCLATURE.....	xiii
1. INTRODUCTION.....	1
1.1. Mining industry in Canada.....	1
1.1.1. Benefits of the mining industry.....	1
1.1.2. Revenue to the governments.....	2
1.1.3. Problems faced by the industry.....	3
2. LITERATURE REVIEW	6
2.1. Difference between a wheel and a rim.....	6
2.2. Difference between a typical road wheel and a mining wheel	7
2.2.1. Size of the tire	7
2.2.2. Wheel material	8
2.2.3. Application.....	8
2.2.4. Type of wheel	8
2.2.5. Difference in the procedure for fitting tires on wheels	11
2.3. Rules and regulations from health and safety organizations	11
2.4. Incidents from service and maintenance of wheels in mining industry.....	14
2.5. Fatigue in metals.....	17
2.6. Theories of fatigue failure under multi-axial stress states	18
2.6.1. Modified Goodman approach	18
2.6.2. Simplified Lemaitre’s approach.....	21
2.6.3. Critical plane approach	22

2.7. Wheel cornering fatigue test	24
2.8. Past numerical investigations on fatigue life assessment of wheels	26
3. RESEARCH OBJECTIVES	27
4. EXPERIMENTAL INVESTIGATIONS	29
4.1. Manufacture of auxiliary fixtures	29
4.1.1. Loading shaft	29
4.1.2. Adapter plate	30
4.1.3. Wheel supporting fixtures	31
4.2. Configuration of the data acquisition system	32
4.3. Strain gauge application	32
4.4. Setup of the ARAMIS system	33
4.5. Setup of the experimental test	35
4.6. Experimental results	36
4.6.1. Results from the data acquisition system	36
4.6.2. Discussions	39
4.6.3. Results from the ARAMIS system	41
4.6.4. Discussions	44
5. FINITE ELEMENT MODELING OF THE EXPERIMENTAL TEST	45
5.1. Numerical model development of the three piece wheel	45
5.1.1. Discretization of the wheel model	45
5.1.2. Material models	48
5.1.3. Contact definition	48
5.1.4. Application of boundary conditions	48
5.2. Simulation procedure	49
5.3. Results of the simulations	49
5.4. Discussions	52

6. VALIDATION OF THE FINITE ELEMENT MODEL.....	54
6.1. Comparison of numerical predictions with the experimental results.....	54
6.2. Discussions of strain versus load profiles from experiments and finite elements	55
6.2.1. Strain gauge location 2L1 on the shaft	56
6.2.2. Strain gauge location 2L2 on the shaft	56
6.2.3. Strain gauge location 1L1 on the mounting ring	57
6.2.4. Strain gauge location 1L2 on the mounting ring	58
6.2.5. Strain gauge location 1L3 on the mounting ring	59
6.2.6. Strain gauge location 1L4 on the flange	60
6.2.7. Strain gauge location H5 on the flange.....	61
6.2.8. Strain gauge location H6 on the flange.....	62
6.2.9. Strain gauge location H7 on the wheel base	63
6.2.10. Strain gauge location H8 on the wheel base	64
7. FINITE ELEMENT SIMULATION OF THE WHEEL CORNERING FATIGUE TEST.....	66
7.1. Finite element model development for fatigue simulation	66
7.1.1. Contact definition.....	67
7.1.2. Application of boundary conditions.....	68
7.2. Simulation procedure	68
8. RESULTS AND DISCUSSIONS OF WHEEL CORNERING FATIGUE TEST	71
8.1. Analysis of the results of wheel cornering fatigue test.....	71
8.1.1. Development of fatigue analysis software.....	71
8.1.2. Results from fatigue analysis software	72
8.1.3. Discussions	74
9. CONCLUSIONS	76

REFERENCES.....	78
APPENDIX A.....	86
APPENDIX B.....	89
APPENDIX C.....	93
APPENDIX D.....	95
VITA AUCTORIS	97

LIST OF TABLES

Table 4.1	Average strain results from the four experiments during peak load application.....	39
Table 4.2	Strains from the ARAMIS system	44
Table 5.1	Aspect ratios of elements in the model.....	46
Table 6.1	Comparison of average strain values from the four experiments and strain predictions of FEA at the peak load	54
Table 8.1	Finite elements with lowest four fatigue factors of safety predicted by each approach.....	73
Table 8.2	Comparison of fatigue factors of safety predicted by different approaches	73

LIST OF FIGURES

Figure 1.1	Contribution of the mining industry to Canada's GDP	2
Figure 1.2	Revenue to the governments from the mining industry	3
Figure 1.3	Fatalities in mining, quarrying and related industries	4
Figure 2.1	Difference between a wheel and a rim	7
Figure 2.2	A typical single piece road wheel.....	9
Figure 2.3	A three piece mining wheel.....	9
Figure 2.4	Single piece wheel.....	10
Figure 2.5	Multi-piece wheel.....	10
Figure 2.6	Incidents categorized based on rim type	16
Figure 2.7	Goodman, Gerber parabola, and Soderberg lines plotted on $\sigma_m - \sigma_a$ axes for fluctuating stress fatigue failure criteria.....	19
Figure 2.8	Wheel cornering fatigue test based on the SAE J1992.....	25
Figure 4.1(a)	Experimental setup illustrating the shaft, the fixtures and the point of load application.....	30
Figure 4.1(b)	Experimental setup illustrating the adapter plate.....	31
Figure 4.2	Positions of strain gauges on the testing apparatus	33
Figure 4.3	Location of strain observation by the ARAMIS system	35
Figure 4.4(a)	Strain versus load profiles for all ten strain gauge positions from the second experiment	37
Figure 4.4(b)	Strain versus load profiles for all strain gauge positions (wheel assembly) from the second experiment	38
Figure 4.5	Output from the ARAMIS system illustrating the method of strain measurement	41
Figure 4.6(a)	Strains versus length of the horizontal section from the second experiment.....	43
Figure 4.6(b)	Strains versus length of the vertical section from the second experiment.....	43

Figure 5.1	Discretized wheel model	47
Figure 5.2(a)	Strain versus load profiles from numerical predictions on the entire test apparatus	50
Figure 5.2(b)	Strain versus load profiles from numerical predictions on the wheel assembly.....	51
Figure 5.3	An effective strain distribution on the testing apparatus at maximum load.....	52
Figure 6.1	Strain versus load profile for shaft position 1 (2L1)	55
Figure 6.2	Strain versus load profile for shaft position 2 (2L2)	56
Figure 6.3	Strain versus load profile for mounting ring position 1 (1L1)	57
Figure 6.4	Strain versus load profile for mounting ring position 2 (1L2)	58
Figure 6.5	Strain versus load profile for mounting ring position 3 (1L3)	59
Figure 6.6	Strain versus load profile for flange position 1 (1L4)	60
Figure 6.7	Strain versus load profile for flange position 2 (H5).....	61
Figure 6.8	Strain versus load profile for flange position 3 (H6).....	62
Figure 6.9	Strain versus load profile for wheel base position 1 (H7).....	63
Figure 6.10	Strain versus load profile for wheel base position 2 (H8).....	64
Figure 7.1	Finite element model for fatigue analysis	67
Figure 7.2	P as an equivalent of P_y and P_z	69
Figure 8.1	1/20 th section of the wheel with 5048 elements considered for fatigue analysis.....	71
Figure 8.2	Elements with lowest four fatigue factors of safety predicted by each approach.....	74

NOMENCLATURE

d	wheel inset or outset
E	Young's modulus
l	length of moment arm
L	test load
L_R	load rating
n	factor of safety
n_{CP}	fatigue factor based on critical plane approach
n_{DM}	fatigue factor based on damage mechanics approach
n_S	fatigue factor based on Sines approach
n_{vM}	fatigue factor based on von Mises approach
P	rotating bending moment
P_Y	bending load in Y direction
P_Z	bending load in Z direction
r_s	largest static loaded radius
R_v	tri-axiality ratio
S	accelerated test factor
S_e	modified fatigue strength of the material
S_{ut}	ultimate tensile strength of the material
t	simulation time
$t_{A,B}$	fatigue strength in torsion (depending on crack case A or B)
$\bar{\epsilon}$	effective strain
ϵ_1	maximum principal strain
ϵ_2	2 nd principal strain
ϵ_3	minimum principal strain
ϵ_{EXP}	strain value from individual experiments at maximum loading
$\bar{\epsilon}_{EXP}$	mean value of strain from all four experiments at maximum loading
ϵ_{FEA}	strain value from numerical predictions at maximum loading
μ	coefficient of friction between tire and road

ν	Poisson's ratio
ρ	density
σ_a	alternating stress component calculated by von Mises and Sines methods
σ_{eq}	effective stress calculated by von Mises approach
$\sigma_{eff,max}$	maximum effective stress by simplified damage mechanics approach
σ_H	hydrostatic stress
$\sigma_{n,max}$	maximum normal stress in the maximum shear stress amplitude plane
$\sigma_{S,m}$	mean stress component calculated by Sines method
$\sigma_{vM,m}$	mean stress component calculated by von Mises method
σ_{xx}	normal stress in X direction
σ_{yy}	normal stress in Y direction
σ_{zz}	normal stress in Z direction
$\sigma_{xx,a}$	alternating normal stress in X direction
$\sigma_{yy,a}$	alternating normal stress in Y direction
$\sigma_{zz,a}$	alternating normal stress in Z direction
$\sigma_{xx,m}$	mean normal stress in X direction
$\sigma_{yy,m}$	mean normal stress in Y direction
$\sigma_{zz,m}$	mean normal stress in Z direction
$\sigma_{xx,max}$	maximum value of stress-time waveform on normal stress in X direction
$\sigma_{xx,min}$	minimum value of stress-time waveform on normal stress in X direction
τ_A	shear stress amplitude (crack case A)
τ_{ij}	shear stress in j direction on i face
$\tau_{xy,a}$	alternating shear stress in y direction on x face
$\tau_{yz,a}$	alternating shear stress in z direction on y face
$\tau_{zx,a}$	alternating shear stress in x direction on z face
$\tau_{xy,m}$	mean shear stress in y direction on x face
$\tau_{yz,m}$	mean shear stress in z direction on y face
$\tau_{zx,m}$	mean shear stress in x direction on z face
ω	angular velocity

1. INTRODUCTION

1.1. Mining industry in Canada

The presence of an established mining industry indicates the availability of plentiful natural resources in a country and hence a significant impact on the economic growth. In the last century, the mining industry has changed the complete phase of the world in a sense that, most of the technology being used today would not have been possible without mining facilities. With the availability of vast natural resources and the existence of a well developed mining industry, Canada remains one of the world's leading mining countries. Canada was the top most destination for global exploration spending in 2006, receiving 19% of world spending followed by Australia at 11% and the United States at 8%. In Canada, most of the mining activities occur in the northern and remote areas of the country. Canada ranks first in the world in potash and uranium production; second in nickel and cobalt; third in titanium concentrate, aluminum, magnesium, gypsum and platinum-group metals; fourth in chrysotile and cadmium; and fifth in zinc and molybdenum [1].

1.1.1. Benefits of the mining industry

Canada's mining industry plays a key role in the foundation of the country's economy by exporting 80% of its products accounting for 17% of annual Canadian exports. For example, in the year 1997, the minerals and metals industry contributed \$26.2 billion to the Canadian economy which equalled 3.8% of the national gross domestic product (GDP). Figure 1.1 illustrates the contribution of the mining industry to the Canadian GDP (in million dollars) from the years 2000 to 2006. Additionally, the industry provides employment opportunities to a significant number of people in the northern territories of Canada with relatively high wages compared to other industries. In the year 1997 alone, the mining and mineral processing industries employed 368,000 Canadian workers with average weekly wages being the highest in the country as compared to other industrial sectors at \$1013.13 [2]. In addition to the weekly wages employed, Canadian mining companies are also actively involved in research and development with approximately 4,600 research and development employees working in

the mining and minerals industry, the total being significantly higher than the number of research and development employees in the agri-food, oil and gas, electrical equipments, and automotive sector and almost close to the aerospace and pharmaceutical sectors. Products of the industry are utilized in building highways, electrical and communication networks, housing, automobiles, consumer electronics, various other products and infrastructure essential for modern life [1].

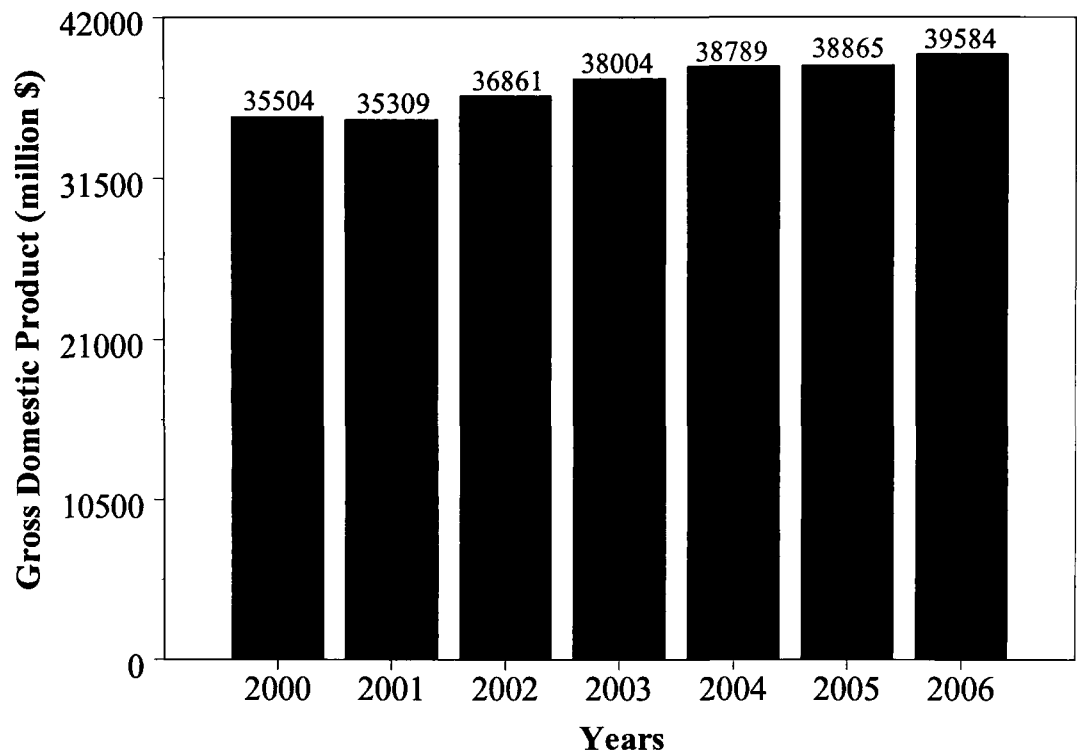


Figure 1.1. Contribution of the mining industry to Canada's GDP [1].

1.1.2. Revenue to the governments

The provincial and federal governments of Canada receive revenues from the mining industry in the form of royalties, mining taxes, corporate and personal income taxes. The total revenue including royalties and taxes generated by the mining industry every year is illustrated in Figure 1.2. Over this five year period from 2002 to 2006, government revenues from the industry have increased by approximately two-thirds [3].

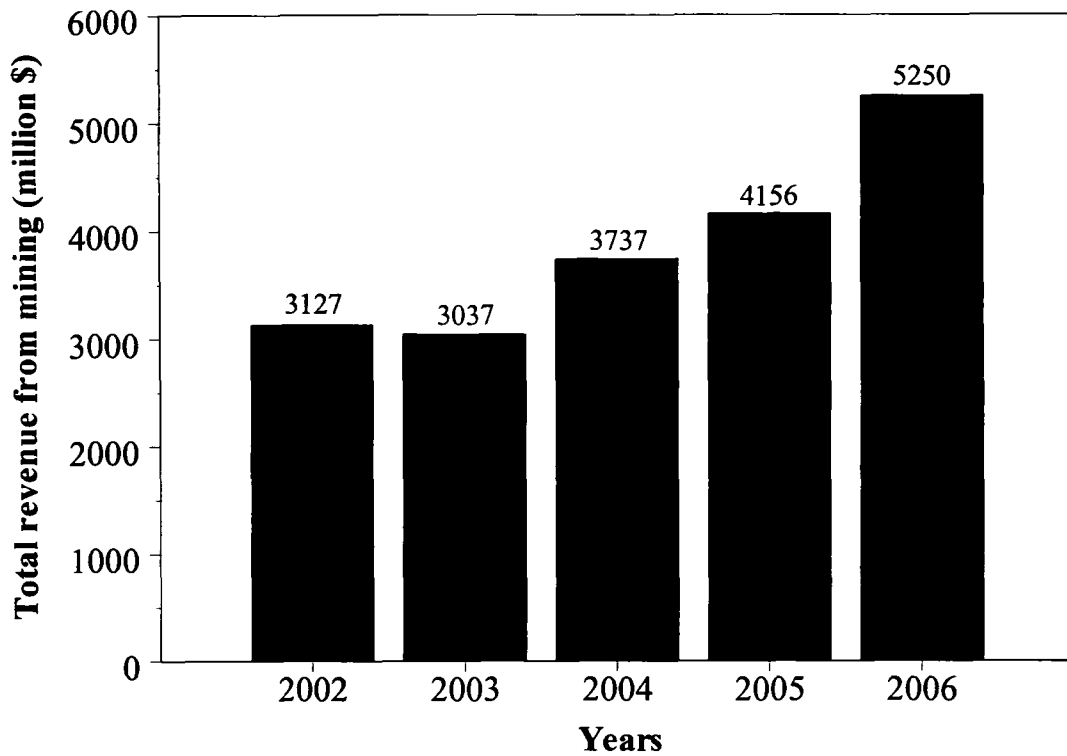


Figure 1.2. Revenue to the governments from the mining industry [3].

1.1.3. Problems faced by the industry

Although, there are numerous benefits received by a country from its mining industry, the fact remains that the workers are subjected to serious negative effects. Work associated in the mining industry poses serious occupational health hazards. First and foremost mining industry causes mental stress in people due to long hours of work, the nature of the work and finally, the nature of employee shift patterns. These irregular shift patterns lead to extreme fatigue in workers due to lack of sleep. Secondly, the repetitive nature of the job, high concentration demands at work and the after effects of job-related physical disabilities lead to mental depression. This high state of mental stress and depression leads to significant behavioural changes among the aboriginal workers of the northern communities of Canada. These behavioural changes can be attributed to high dosage of alcohol and nicotine, addiction to other harmful drugs (drug abuse) and lastly even prostitution [4]. Additionally, the most serious consequence is that, as with other industries, injuries and fatalities occur amongst workers throughout

any given year. In spite of the several improvements in the workplace safety that have occurred through technological innovations, safe work practices and policy regulations, injuries and fatalities still occur in the industry. However, these measures have resulted in a decrease in the annual fatality rate (deaths per 100,000 miners) from 329 (average rate from 1911 - 15) to 25 (1996 - 97). A summary of number of fatalities in the mining industry from year 2000 to 2006 is illustrated in Figure 1.3 [5 - 22]. Various causes behind these fatalities can be classified into (i) mine fires, (ii) falls, (iii) individual(s) run over by mining vehicles, (iv) individual(s) being caught in machinery, and (v) maintenance personnel(s) being struck by heavy objects with great forces.

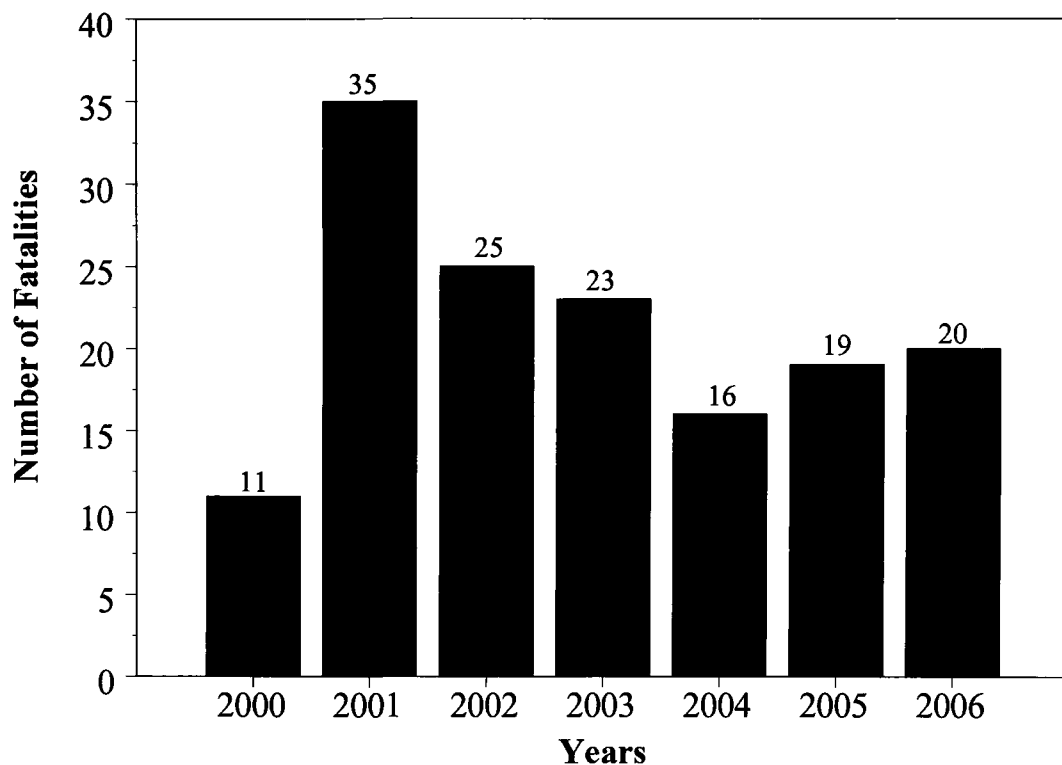


Figure 1.3. Fatalities in mining, quarrying and related industries [5 - 22].

Further investigation into the last classification indicates that a maintenance personnel working on mining vehicle wheels being struck by the wheel and its various components is common in the industry. In spite of the fact that human errors are

predominantly the reason for such incidents, at times, even mechanical wear and degradation of the wheels compound to result in a catastrophic failure.

2. LITERATURE REVIEW

An extensive literature review was completed focusing on the general topics of mining vehicles and the wheels used on mining vehicles, with an emphasis on multi-piece wheels and statistics of fatalities and injuries arising as a result of incidents that occur during maintenance of the multi-piece wheels. A thorough study was completed to understand (i) the technology behind multi-piece wheels and the need for such wheels in the mining industry, (ii) the differences between a typical road wheel and a multi-piece mining wheel, (iii) rules and regulations to be followed while installing or servicing multi-piece wheels, and (iv) fatalities and injuries associated with servicing and maintenance of the multi-piece wheels in places such as North America, Australia, parts of Asia and Africa with a particular focus on Canada and United States. Additionally, various standards related to experimental fatigue testing of wheels, state of the art techniques in numerical modeling of mining wheels and other relevant research topics were considered during the literature review part of this investigation.

2.1. Difference between a wheel and a rim

In the scope of the research presented in this thesis, ‘wheel’ and ‘rim’ are two different entities associated with a mining vehicle. Figure 2.1 illustrates the difference between a typical wheel and a rim. Wheel as illustrated in Figure 2.1(a) has a wheel base with an integrated flange, a removable side flange and a locking ring which holds the removable flange in position. Additionally, the wheel has an integrated mounting ring which is either welded or riveted to the wheel base. This mounting ring aids in fastening the wheel to the hub of the vehicle. However, a rim is made of a rim base, a removable flange and typically a locking ring (hidden in the presented configuration) as shown in Figure 2.1(b). A rim does not have an integrated mounting ring as in a wheel. To enable the rim to be mounted onto a vehicle, a spoke wheel as presented in Figure 2.1(c) has to be clamped to the center of the rim.

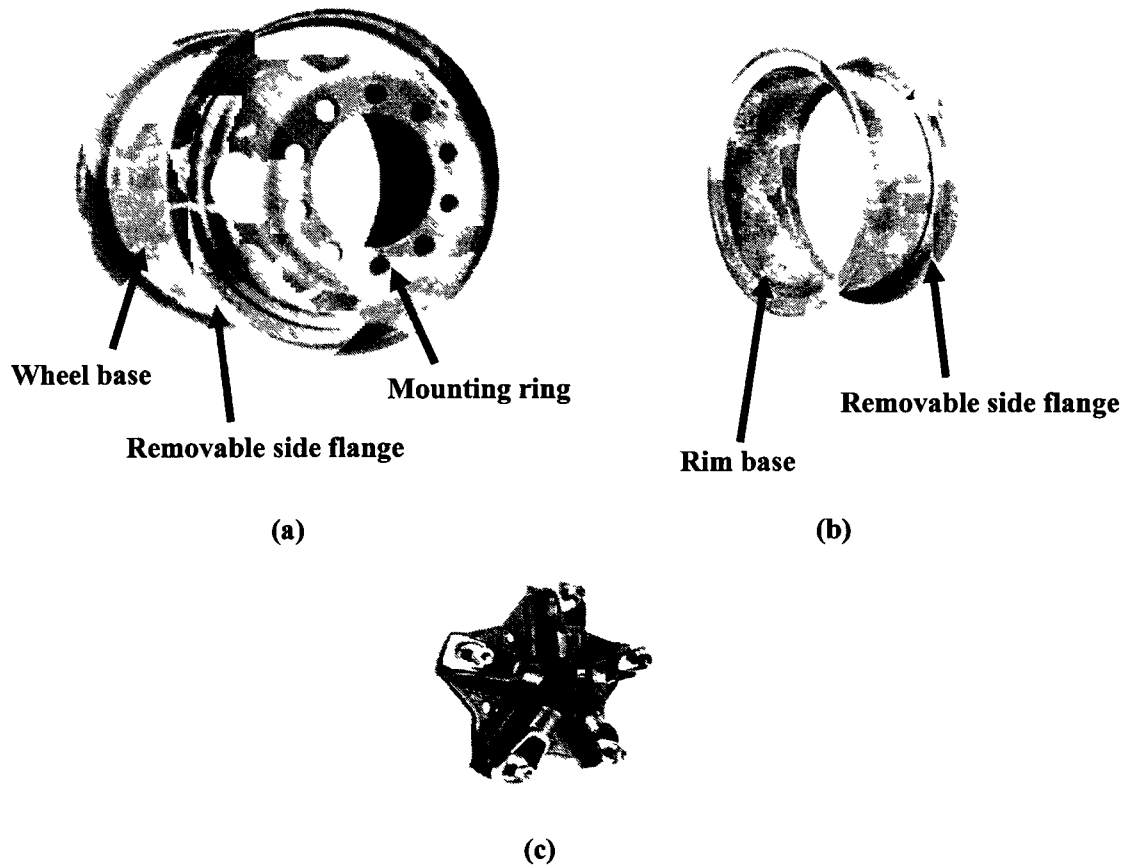


Figure 2.1. Difference between a wheel and a rim, (a) Wheel, (b) Rim, (c) Cast spoke wheel.

2.2. Difference between a typical road wheel and a mining wheel

Road wheels are generally referred to the wheels on road cars and pick-up trucks, whereas mining wheels are generally utilized by vehicles such as loaders, dump trucks, and graders, in the mining industry. Mining wheels differ from typical road wheels in a number of aspects including but not limited to size of tires, geometry, material, application, type of the wheel (single piece / two-piece / three-piece) and the procedure for fitting tires.

2.2.1. Size of the tire

The diameter of tires used on typical road wheels roughly varies from 0.45 to 0.60 metres, whereas for tires on mining wheels, the diameter may be between 1.22 and 3.66 metres.

2.2.2. Wheel material

Road wheels are usually made in a single piece through casting process either with magnesium or aluminum to improve fuel economy. Mining wheels are conventionally made of mild steel because of the weight of the vehicle and the payload they have to support during transportation.

2.2.3. Application

Conventional road wheels are meant to be used on smoothly paved roads at speeds up to approximately 120 km/hr, whereas mining wheels are used on sand, gravel, rugged and marshy terrains with relatively lower speeds of approximately 20 to 40 km/hr. The gross load on a typical road wheel from a road vehicle is approximately 1 to 3 tons whereas, in the case of mining vehicles, apart from the weight of the vehicle that the wheels have to support, they will be additionally subjected to payloads on the order of 30 tons on a surface mining vehicle to 45 tons on an underground mining vehicle.

2.2.4. Type of wheel

Road wheels are typically single piece, as illustrated in Figure 2.2. Mining wheels are usually multi-piece wheels as illustrated in Figure 2.3. The components of a three-piece wheel are the wheel base (consisting of a fixed flange and a mounting ring), the removable side flange, and a locking ring. The locking ring can be either continuous or split and availability of all the components of a multi-piece wheel is necessary to appropriately fit the tire onto the wheel. Proper positioning of all components is necessary to maintain the structural integrity of the wheel during operation and maintenance.

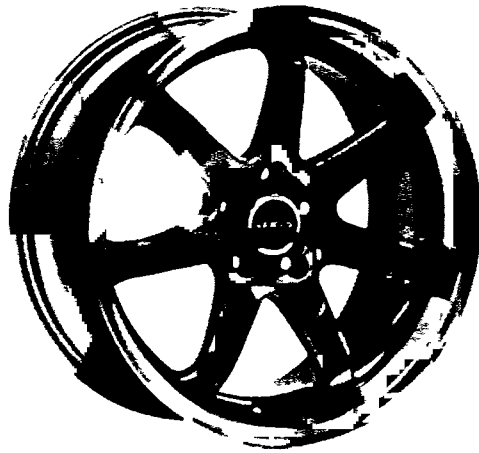


Figure 2.2. A typical single piece road wheel.

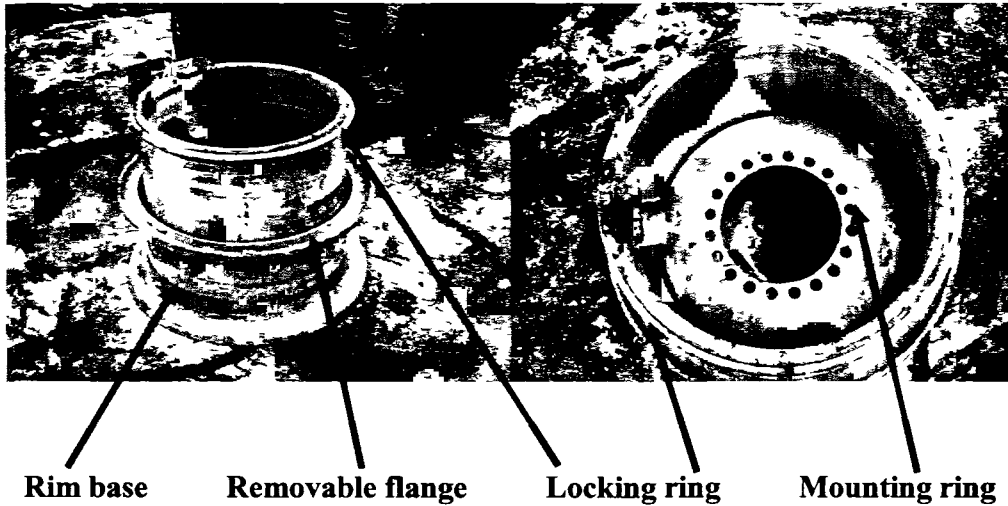


Figure 2.3. A three-piece mining wheel.

A cross-sectional view of a typical single piece wheel is provided in Figure 2.4 with annotations to indicate the rim width, rim diameter, and rim offset, which is defined as the distance between the bottom surface of the mounting ring and the horizontal centreline of the wheel. Figure 2.5(a) and (b) represent cross-sectional views of two-piece and three-piece wheel assemblies respectively. In a two-piece wheel, the gutter geometry of the rim base acts as a locking mechanism to hold the removable flange upon inflation of the tire, whereas in a three-piece wheel, the locking ring prevents the

outward motion of the removable flange when the tire is fully inflated. Any damage or misalignment between these contacting entities significantly increases the potential for incidents involving wheel assembly.

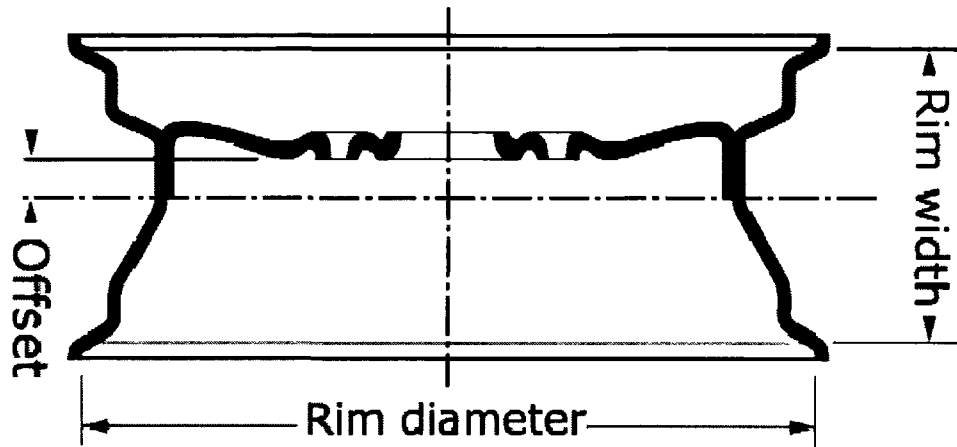
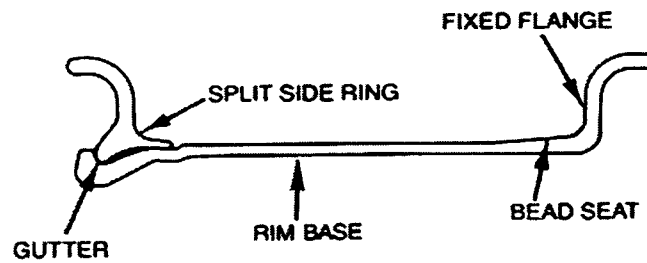
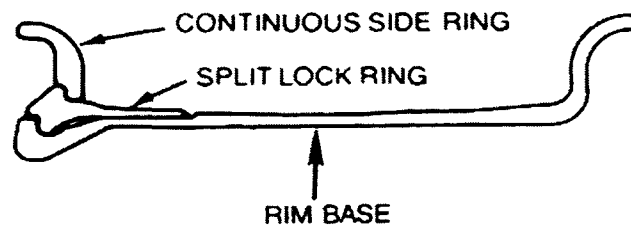


Figure 2.4. Single piece wheel.



(a)



(b)

Figure 2.5. Multi-piece wheel, (a) Two-piece wheel, (b) Three-piece wheel [29].

2.2.5. Difference in the procedure for fitting tires on wheels

There is a significant difference between the procedure for fitting a tire onto a mining wheel and a road wheel. Typically in conventional automobiles, as a result of the use of a single piece wheel, the bead of the tire is pushed onto the wheel from one side and the other bead is brought into the wheel by means of prying action. This procedure can be done either by manually prying the tire onto the wheel or the entire process of putting the tire on the wheel can be automated.

Due to the fact that a mining wheel has to support significantly high payloads and as a result of the high pressures that mining tires have to hold inside, the beads of the tires used on mining wheels are very stiff by having a significant tire side wall thickness. This large amount of rubber does not allow prying of the tire onto a single piece wheel as damage to either the wheel or tire will result. Therefore a multi-piece wheel is often used in the mining industry. As a first step in the procedure for fitting a tire onto a mining wheel, the wheel base is held without the removable side flange and the tire is pushed onto the wheel base. Afterwards, the removable side flange is placed on the wheel base / tire assembly and is maintained in place by insertion of the split locking ring and inflation of the tire. Once the wheel is pressurized, the removable flange is pushed against the locking ring and so the components of the tire are held in proper location to ensure the structural integrity of the wheel under operation. Rubber 'O' rings are used at the locking ring and wheel interface.

2.3. Rules and regulations from health and safety organizations

Inflating a truck tire appears simple and non-hazardous until one realizes that a 0.50 m tire inflated to 690 kPa can contain up to approximately 180 kN of explosive force [23]. A tire which has been properly maintained has the ability to handle that amount of pressure. However, a poorly maintained tire or a tire which has been run flat or under-inflated for a long period of operation has the potential for serious catastrophes. Operating the vehicles for a long duration with flat or under-inflated tires significantly increases the potential for damage or misalignment of various components of the wheel. Servicing or performing any maintenance operation on such wheels with misaligned components without completely deflating the tires paves the way for serious catastrophes

resulting due to tire explosions. In spite of the fact that the tire was run under-inflated, the pressure inside while servicing is more than sufficient to project various wheel parts, potentially causing serious injuries or death to nearby workers.

A number of different health and safety organizations throughout the world including, but not limited to, Occupational Safety and Health Administration (OSHA), National Institute of Occupational Safety & Health (NIOSH), Mines and Aggregates Safety and Health Administration (MASHA), and WorkSafe have framed a set of rules, regulations, and guidelines to be followed by individuals who are involved in service and maintenance of multi-piece wheels. It is the responsibility of every employer in the mining industry to ensure safety of all employees by exposing them to various regulations of the safety organizations. This can be achieved through the following methods:

- 1) Posting safety instructions for servicing in the area where service and maintenance of tires are performed.
- 2) Training new workers on safety procedures to handle such wheels and testing workers after the training to assess their level of understanding.
- 3) Lastly, documenting the training given to new workers.

SAFEWORK [24] specifically lists the following rules, which are to be abided by workers while servicing multi-piece wheels:

- 1) Tires must be completely deflated by removing the valve core prior to removal of the tire from the rim.
- 2) Tires must be mounted on compatible wheels of matching bead diameter and width. Care must be taken not to damage the bead while mounting the tire.

- 3) A non-flammable lubricant must be applied to the bead and wheel mating surfaces before mounting the bead.
- 4) The tire must be inflated only inside a restraining cage.
- 5) No tool other than the ones prescribed by the manufacturer should be used to work on the tire.
- 6) A clip on chuck with an in-line pressure gauge and a sufficient length of hose must be used while inflating the tire.
- 7) Tires must not be inflated to more than the recommended tire pressure.
- 8) Heat of any nature must not be supplied to the wheels. Cracked, broken, bent or otherwise damaged wheels must not be reworked, welded, brazed or heated.

Maintenance personnel who are involved in service and maintenance of multi-piece wheel are faced with a potential threat of serious injuries or even loss of life, if the rules dictated by various health and safety organizations are not properly followed.

An investigation into the statistics of fatalities and injuries in the mining industry as a result of incidents from servicing multi-piece wheels was completed. Identification of the causes of these incidents, the type of vehicle (or even specifically the wheel involved), and rationale for the failure of wheel components, and death / injury were completed. Causes of these incidents were identified to be mine fires, falls, individual(s) run over by mining vehicles, individual(s) being caught in machinery, and lastly, maintenance personnel(s) being struck by heavy objects. In the category of being struck by heavy objects, multi-piece wheels used on mining vehicles and their components were observed to be more commonly involved in incidents than any other heavy object utilized by the industry. In most of the documentation of such incidents, critical information pertaining to make of the wheel, tire or vehicle was maintained confidential. Published case studies for some of the incidents addressed a minimal amount of critical information

(as previously listed in the third and fourth lines of this paragraph). The remaining documentation did not make reference to any critical information associated with the incident. As a result of this lack of critical information in the published documentation, personal contact with associated personnel was attempted wherever possible. This information, either extracted from the published documentation, or obtained through personal contact is discussed in section 2.4.

2.4. Incidents from service and maintenance of wheels in mining industry

One incident associated with a single piece rim involving a tire failure, commonly addressed as a zipper type failure, was attributed to the weak side wall of the tire. The weakened sidewall significantly reduced the tire's ability to hold pressure and the tire failed upon inflation, leaving a zipper pattern on the tire. The failure caused an explosion, which hurled the tire against a nearby worker with excessive force causing fatal injuries [25].

Specific to the two-piece rim assembly, two incidents were noted in which the workers were young (aged 20 years and 24 years). Moreover, they were not appropriately trained enough prior to performing maintenance work on the wheels. The rationale behind these incidents was observed to be carelessness, and negligence in following the safety procedures prescribed by the wheel manufacturers. Additionally, improper tools (i.e., a pneumatic impact wrench) which were branded unsafe by the wheel manufacturers were used during wheel servicing [26 and 27].

Eleven incidents involved three-piece rim assemblies, and two cases out of the eleven employed young workers to service multi-piece rims [28 and 29]. The incidents resulted due to carelessness at work and lack of understanding the importance of adherence to maintenance procedures specified by the wheel manufacturers, as previously noted in the two cases involving two-piece rim assemblies. Two other incidents, where a worker failed to use an in-line pressure gauge [30] and another worker removed inappropriate bolts on the wheel causing the rim to explode [31], resulted in three fatalities. There was no reported evidence of documentation of the training given to the workers in the four incidents as per the references [28 - 31]. Six incidents were noted, in which inflation of tires that were run flat or under-inflated for a long period of

use caused the tires to explode projecting the wheel components against nearby workers, resulting in fatal injuries [25 and 32 - 36]. Two incidents revealed specific information such as the locking ring just being partially seated prior to inflation [32] and the locking ring not being fully engaged in the rim gutter because of a distorted side ring [25]. Most or all of the incidents noted above could have been prevented by proper use of a restraining cage during inflation of the tires. Another incident resulted only in injuries to two maintenance personnel [37]. While they were trying to remove the lug nuts from the wheel utilizing a socket wrench without completely deflating the tire, the removable flange projected off the wheel with great force and came in contact with the workers. Consequently both suffered lacerations.

One fatal incident involving a five piece rim assembly was noted from the reviewed literature. When the worker was removing the outer tire on a dual tire assembly, either a damaged component or some form of a misalignment in the inner wheel caused it to fail resulting in its explosion. The explosion propelled the outer wheel assembly along with the failed components of the inner wheel assembly [38].

Eleven incidents were noted in the category that had no specific reference made to the type of the rim assembly involved. Seven out of the eleven had fatalities owing to the same reasons mentioned in the previous paragraphs. A number of different causes associated to the damage imparted to the wheel assembly during operation were responsible for the incidents in the remaining four cases. It was noted that very old rims were still used in the industry and they were severely pitted and corroded owing to excessive usage. These rims were not strong enough to hold the tire during inflation and hence failed leading to a catastrophe [39 and 40]. As reported previously in most of the cases, the workers were very young and were found inflating the wheels without using a restraining cage. In one other incident, a young worker observed a crack appearing on the split rim while he started removing the bolts from the rim assembly without deflating the tire. As he continued further to remove the bolts, the assembly exploded resulting in the loss of the worker's life [41]. As per the report referenced in [33], an 85-ton truck traveled close to a 138 kV electrical line with its box elevated and as a result, six tires of the truck exploded due to pyrolysis. The first tire exploded after traveling approximately 300 metres and the remaining six tires exploded afterwards at 20 second intervals. The

explosion caused the components of the wheel assemblies to be sent to distances as far as 30 metres from the truck.

Although, it can be concluded that, for the majority of cases, the main rationale behind wheel assembly explosion resulting in injury or death was due to worker or maintenance personnel failing to follow appropriate safety procedures, a number of cases [25, 27, 28, 33, 37, and 39 - 41] existed where damage and reduced fatigue life of the rim assembly also contributed to failure. Additionally, amongst the entire range of multi-piece wheels used in the mining industry, three-piece wheels were more commonly involved in incidents as illustrated in Figure 2.6, which summarizes the number of incidents associated with each type of rim assembly. For this reason, a three-piece wheel was selected to complete the experimental and numerical investigations needed for this research.

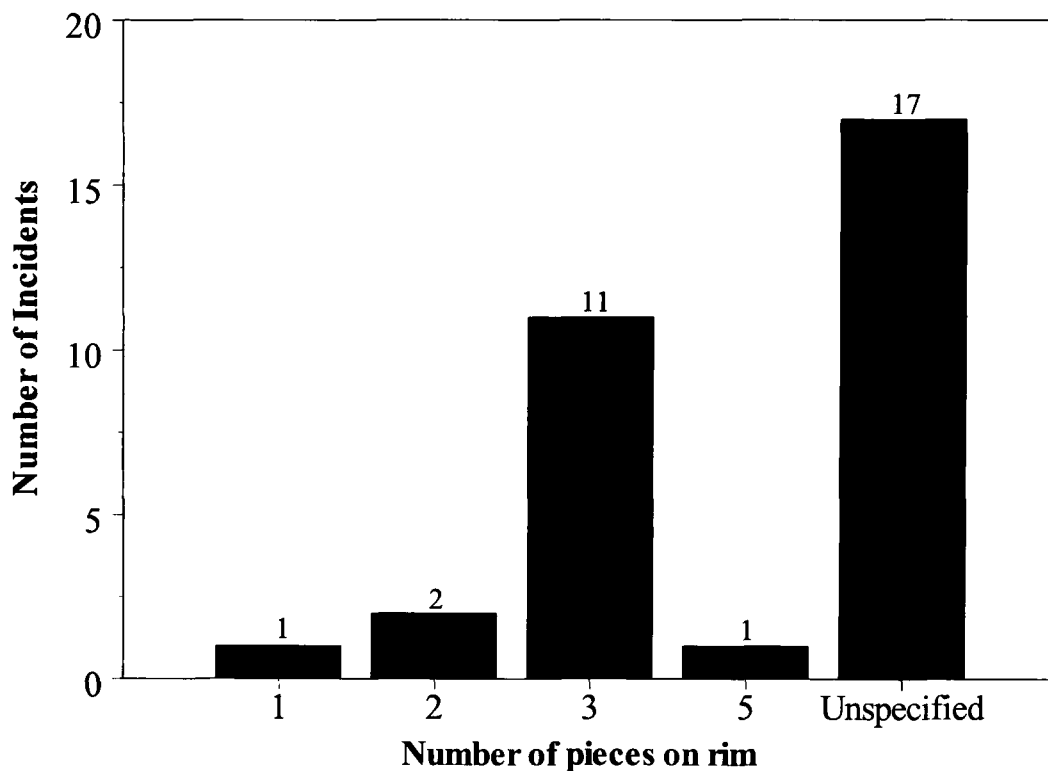


Figure 2.6. Incidents categorized based on rim type.

To the best of author's knowledge, no publications dealing with estimations of the fatigue life of multi-piece mining wheel assemblies exist. Moreover, from a thorough

review of the obtained literature, it was concluded that, no standard specific to the fatigue testing of a mining wheel exists. Hence, the SAE J1992 wheel cornering fatigue test protocol which was developed by the Society of Automotive Engineers (SAE) for assessing the fatigue performance of multi-piece bolted military vehicle wheel assemblies was applied in numerical investigations involved in this research.

2.5. Fatigue in metals

Many structures and machine components are often subjected to highly fluctuating stresses due to the nature of the cyclic loading they experience. These components have been found to fail even though they were subjected to stresses well below the ultimate tensile strength or in some cases even below the yield strength of the material. This nature of failure under the action of repeatedly occurring alternating or fluctuating stresses though within the yield stress is called fatigue failure. A fatigue failure in any component occurs as a three step process. The first stage is the initiation of one or more micro-cracks due to cyclic plastic deformation followed by crystallographic propagation. These cracks are not normally visible to a naked eye. In the second stage, propagation from micro-cracks to macro-cracks occurs. The final stage corresponds to an unstable crack growth and fracture occurs when the remaining material can no longer support the applied load [42]. Fatigue failure in metals can be divided into two classifications such as low cycle fatigue and high cycle fatigue, depending upon the number of load cycles they withstand before failure. In low cycle fatigue, the components do not last more than ideally 10^3 cycles due to the significant amount of plastic straining induced every cycle by the cyclic loading, whereas, in high cycle fatigue, a component typically lasts more than 10^3 cycles as the strains induced are well within the elastic range. The current investigation on mining wheels is a high cycle fatigue problem and out of the three major fatigue life classifications namely stress-life, strain-life, and linear-elastic fracture mechanics, the stress-life method based on the stress levels is the most appropriate method for this problem. In spite of being the least accurate method (especially for low cycle fatigue applications), it is the most traditional method, since it is the easiest to implement for a wide range of applications, has ample supporting data and represents high cycle applications adequately [42]. Additionally, the

state of stress experienced by the mining wheel under fatigue loading will be the same in any cycle, whereas the strains will keep increasing gradually with every cycle owing to the degradation of the material. Hence it is easy to get an estimate of the state of stress to calculate fatigue life of the wheel.

2.6. Theories of fatigue failure under multi-axial stress states

A structure or a mechanical component (multi-piece wheel in this current investigation) experiences periodic, time-varying, multi-axial stresses under the action of a fatigue load. The stress state of a particular location within a component at any instant of time can be completely described with a stress tensor involving all the normal and shear stresses ($\sigma_{xx}, \sigma_{yy}, \sigma_{zz}, \tau_{xy}, \tau_{yz}, \tau_{zx}$). The alternating ($\sigma_{xx,a}, \sigma_{yy,a}, \sigma_{zz,a}, \tau_{xy,a}, \tau_{yz,a}, \tau_{zx,a}$) and mean ($\sigma_{xx,m}, \sigma_{yy,m}, \sigma_{zz,m}, \tau_{xy,m}, \tau_{yz,m}, \tau_{zx,m}$) stresses which are significant in determining the fatigue life of a component can be calculated using equations (2.1) and (2.2). These equations are for normal x -axis stress component and the equations can be modified as needed to calculate the alternating and mean stresses for other components in the stress tensor.

$$\sigma_{xx,a} = \frac{\sigma_{xx,\max} - \sigma_{xx,\min}}{2} \quad (2.1)$$

$$\sigma_{xx,m} = \frac{\sigma_{xx,\max} + \sigma_{xx,\min}}{2} \quad (2.2)$$

2.6.1. Modified Goodman approach

Figure 2.7 illustrates a number of different fatigue failure theories utilizing the safe limit line for each theory plotted in the $\sigma_m - \sigma_a$ domain. The modified Goodman approach which has a linear profile in the $\sigma_m - \sigma_a$ domain is considered one of the most conservative approaches to fatigue life estimation [42] and is used in most design applications where components will be subjected to large number of load application cycles. The modified Goodman line is plotted with mean stresses on the abscissa and

alternating stresses on the ordinate. The line connects S_{ut} on the abscissa and S_e on the ordinate. The modified Goodman relation can be written as shown in equation (2.3).

$$\frac{\sigma_a}{S_e} + \frac{\sigma_m}{S_{ut}} = 1 \quad (2.3)$$

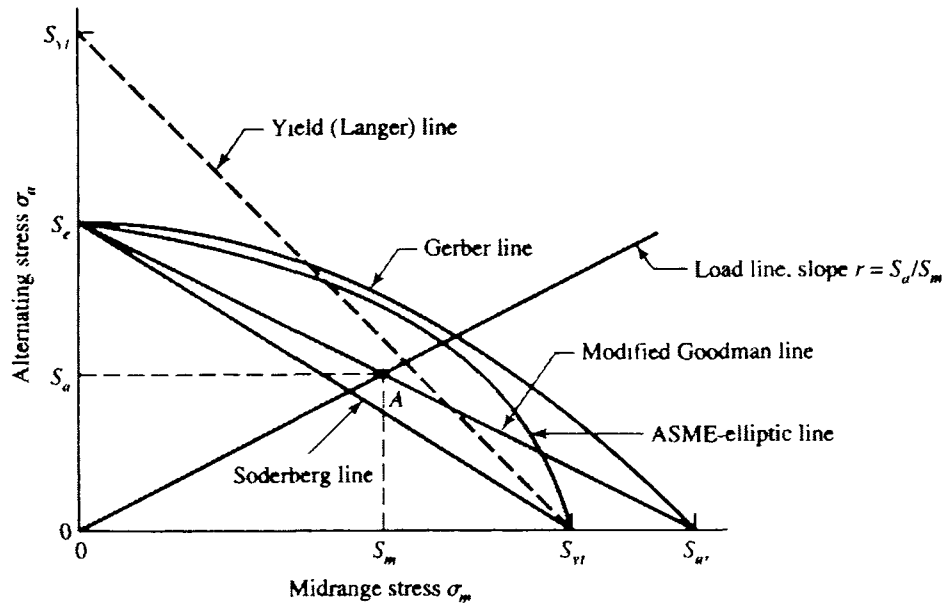


Figure 2.7. Goodman, Gerber parabola, and Soderberg lines plotted on $\sigma_m - \sigma_a$ axes for fluctuating stress fatigue failure criteria [42].

In order to utilize this relation in practical fatigue life assessments, a factor of safety needs to be considered. The alternating and midrange stresses σ_a and σ_m can be replaced with stresses $n\sigma_a$ and $n\sigma_m$ where n is the factor of safety and then the modified Goodman relation takes the form in equation (2.4).

$$\frac{\sigma_a}{S_e} + \frac{\sigma_m}{S_{ut}} = \frac{1}{n} \quad (2.4)$$

The distortion energy theory or von Mises theory of failure suggests that for a condition of fully reversed loading in ductile materials, this theory can be applied to convert a multi-axial stress state under a fatigue loading into an equivalent uni-axial situation, if the effective alternating stress is calculated based on the von Mises approach utilizing the alternating stress components as represented in equation (2.5) [43]. In cases where non-zero mean stresses exist, even the mean stresses play a significant part in the assessment of fatigue life and the effective mean stress based on von Mises approach can be estimated utilizing equation (2.6) which deals with the mean stress components [44 & 45].

$$\sigma_{vM,a} = \sqrt{\frac{(\sigma_{xx,a} - \sigma_{yy,a})^2 + (\sigma_{yy,a} - \sigma_{zz,a})^2 + (\sigma_{zz,a} - \sigma_{xx,a})^2 + 6(\tau_{xy,a}^2 + \tau_{yz,a}^2 + \tau_{zx,a}^2)}{2}} \quad (2.5)$$

$$\sigma_{vM,m} = \sqrt{\frac{(\sigma_{xx,m} - \sigma_{yy,m})^2 + (\sigma_{yy,m} - \sigma_{zz,m})^2 + (\sigma_{zz,m} - \sigma_{xx,m})^2 + 6(\tau_{xy,m}^2 + \tau_{yz,m}^2 + \tau_{zx,m}^2)}{2}} \quad (2.6)$$

Similar to the distortion energy theory, Sines theory of failure [46] can also be implemented to calculate effective alternating and mean stresses to assess fatigue life. The effective alternating stress calculated using the approach suggested by Sines is consistent with the von Mises definition of utilizing the alternating stress components as presented in equation (2.7). However, to calculate the effective mean stresses, unlike the von Mises approach, only normal stress components are employed as illustrated in equation (2.8). The theory does not incorporate mean components of shear stress in the effective mean stress definition, and it is consistent with experimental observations for multi-axial fatigue loading of smooth, polished, un-notched specimens [47].

$$\sigma_{S,a} = \sqrt{\frac{(\sigma_{xx,a} - \sigma_{yy,a})^2 + (\sigma_{yy,a} - \sigma_{zz,a})^2 + (\sigma_{zz,a} - \sigma_{xx,a})^2 + 6(\tau_{xy,a}^2 + \tau_{yz,a}^2 + \tau_{zx,a}^2)}{2}} \quad (2.7)$$

$$\sigma_{S,m} = \sigma_{xx,m} + \sigma_{yy,m} + \sigma_{zz,m} \quad (2.8)$$

The effective alternating and mean stresses calculated by von Mises and Sines approaches are used in the modified Goodman theory of failure to assess a fatigue factor of safety. Based on equation (2.4), fatigue factors of safety n_{vM} (von Mises approach) and n_S (Sines approach) were calculated utilizing the formulae presented in equations (2.9) and (2.10).

$$n_{vM} = \frac{S_e \cdot S_{ut}}{\sigma_{vM,a} \cdot S_{ut} + \sigma_{vM,m} \cdot S_e} \quad (2.9)$$

$$n_S = \frac{S_e \cdot S_{ut}}{\sigma_{vM,a} \cdot S_{ut} + \sigma_{S,m} \cdot S_e} \quad (2.10)$$

2.6.2. Simplified Lemaitre's approach

Material damage starts to occur at very early stages of fatigue loading and this initiates defects at micro and nano scales under cyclic stresses that are well below the engineering yield stress of the material as previously discussed [48]. As a result of this, failure due to fatigue is not easily identifiable in metals. Lemaitre provides a simplified approach to estimating the fatigue life under a fully reversed multi-axial stress state which states that the maximum effective stress ($\sigma_{eff,max}$) within the component should be ideally less than the modified fatigue strength (S_e) of the material. A fatigue factor of safety of the component utilizing this approach can be estimated based on equation (2.11).

$$n_{DM} = \frac{S_e}{\sigma_{eff,max}} \quad (2.11)$$

where $\sigma_{eff,max}$ is calculated as:

$$\sigma_{eff,max} = \sigma_{eq} R_v^{1/2} \quad (2.12)$$

where,

$$\sigma_{eq} = \sqrt{\frac{(\sigma_{xx} - \sigma_{yy})^2 + (\sigma_{yy} - \sigma_{zz})^2 + (\sigma_{zz} - \sigma_{xx})^2 + 6(\tau_{xy}^2 + \tau_{yz}^2 + \tau_{zx}^2)}{2}} \quad (2.13)$$

$$R_v = \frac{2 \cdot (1 + \nu)}{3} + 3(1 - 2\nu)(\sigma_H / \sigma_{eq})^2 \quad (2.14)$$

$$\sigma_H = \frac{\sigma_{xx} + \sigma_{yy} + \sigma_{zz}}{3} \quad (2.15)$$

σ_{eq} and σ_H are calculated utilizing the maximum values of all the components presented in equations (2.13) and (2.15) respectively. σ_{eq} is the equivalent stress calculated based on the von Mises approach and σ_H is the hydrostatic stress. The ratio of σ_H / σ_{eq} is called the stress triaxiality and R_v is called the triaxiality function. The knowledge of this stress triaxiality is very important as it partly governs the damage growth through the triaxiality function [48].

2.6.3. Critical plane approach

In addition to the above mentioned approaches of fatigue life estimation, a critical plane approach for estimation of fatigue life proposed by McDiarmid [49] was incorporated in this study. According to McDiarmid's theory, fatigue strength depends on the shear stress amplitude and the maximum normal stress on the plane of maximum shear stress amplitude (which is referred to as the critical plane). Based on data from a series of experimental fatigue tests conducted by McDiarmid on thin walled tubular specimens, he proposed a simplified general criterion of failure for high cycle multi-axial

fatigue (which is relevant to the current study involving multi-piece mining wheel) as presented in equation (2.16).

$$\tau_a = C_1 - C_2 \cdot \sigma_{n,\max} \quad (2.16)$$

In equation (2.16), the shear stress amplitude τ_a , is a function of $\sigma_{n,\max}$, which is the maximum normal stress (equal to the sum of alternating and mean components of the normal stress) on the critical plane of maximum shear stress amplitude. According to McDiarmid [49], for a reversed shear fatigue problem, the constant C_1 can be assumed to be equal to the reversed shear fatigue strength and C_2 equal to the reversed shear fatigue strength divided by twice the ultimate tensile strength of the material. The reversed shear fatigue strength ($t_{A,B}$) as presented in equation (2.17) depends on the crack type, either case A or B. Case A is a crack which initiates on the surface and subsequently propagates through the component, whereas the crack initiation site occurs within a component and propagates outward in case B. Upon incorporating the type of crack growth, the new criterion for failure can be written as in equation (2.17).

$$\tau_a = t_{A,B} - \frac{t_{A,B}}{2S_{ut}} \cdot \sigma_{n,\max} \quad (2.17)$$

To apply the failure criterion in practical design application, a factor of safety n_{CP} has been incorporated into the failure criterion and can be estimated utilizing equation (2.18). McDiarmid [50] proposed that for multi-axial loading conditions resulting in combined normal and shear stresses, value of the reversed shear fatigue strength can be assumed as the fatigue strength of the material in torsion which is estimated as 0.3 times the value of ultimate tensile strength of the material. This approximation has been used in this study.

$$n_{CP} = \frac{2S_{ut} \cdot t_{A,B}}{\tau_a \cdot 2S_{ut} + \sigma_{n,\max} \cdot t_{A,B}} \quad (2.19)$$

2.7. Wheel cornering fatigue test

There existed no specific standard to perform a fatigue test on a multi-piece mining wheel. In this current investigation, a wheel cornering fatigue test was performed on a three-piece wheel utilizing the procedure obtained from the Society of Automotive Engineers' standard SAE J1992, the testing methodology for a multi-piece bolted wheel used in military vehicles. Figure 2.8 illustrates the setup of wheel cornering fatigue test based on the SAE J1992 testing protocol.

According to the SAE J1992 protocol, the test is conducted by subjecting the wheel to a rotary fatigue load. This is achieved by either applying a rotating bending moment to a fixed wheel assembly or a fixed load which is capable of generating the corresponding bending moment, to a rotating wheel assembly. The shaft to which the load is applied is attached to the mounting ring of the wheel assembly utilizing the bolts specified by the wheel manufacturer. Correspondingly, the nuts have to be tightened to the torque levels suggested in the manufacturer's guidelines. The wheel under no load should not have an eccentricity of more than 0.254 mm in its clamped position. The test load is applied at the free end tip of the shaft in a position parallel to a plane through the centre of the wheel and the test load should be capable of maintaining the applied load within $\pm 3\%$ throughout the duration of the test [51]. Equation (2.20) can be used to calculate the test load ' L ' to be applied to the wheel assembly.

$$L = \frac{(\mu \cdot r_s + d) \cdot S \cdot L_R}{l} \quad (2.20)$$

where,

L is the test load to be applied to the wheel assembly

μ is the co-efficient of friction between the tire and the road

r_s is the static loaded radius of the largest possible tire for the wheel

d is the inset or outset on the wheel

S is the accelerated test factor

L_R is the load rating of the wheel as specified by the wheel manufacturer

l is the moment arm

In the current study, it was not possible to estimate the test load utilizing equation (2.20) due to the fact that this standard was not specific to a multi-piece mining wheel and as a result most of the above mentioned parameters were unavailable. However, based on the load rating of the wheel obtained from the wheel manufacturer, and the gross vehicle weight of the mining vehicle, an approximate value of the test load to be applied to the wheel during the experimental testing was calculated as 22 kN.

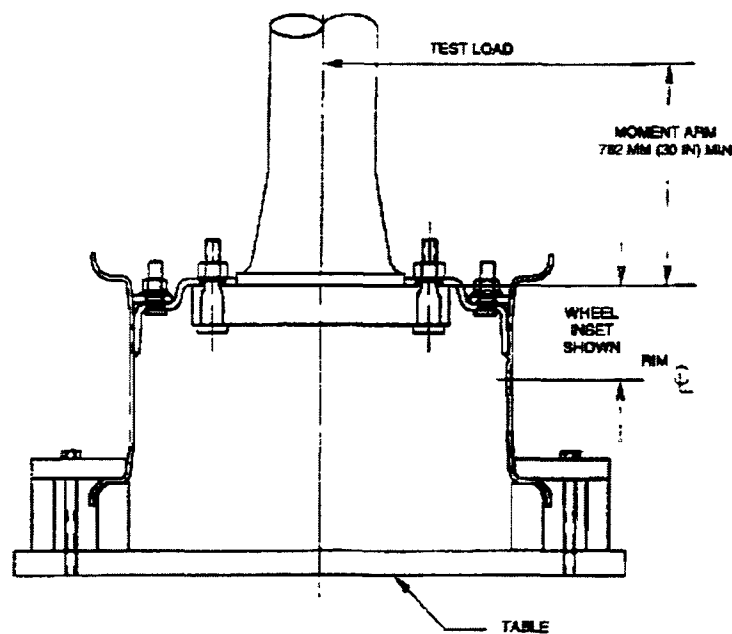


Figure 2.8. Wheel cornering fatigue test setup based on SAE J1992 [52].

The wheel assembly should be able to withstand a minimum of 20,000 cycles of the applied rotary fatigue load in order to pass the test. However, during the fatigue testing of the wheel, if the wheel assembly reaches a state where it cannot support the applied load any longer, (or) a visually detected crack appears and penetrates through any section of the wheel assembly (or) any of the wheel clamps break and separate from the wheel assembly, the test is terminated.

2.8. Past numerical investigations on fatigue life assessment of wheels

Shang [52] has previously completed numerical analysis involving dynamic impact and cornering fatigue conditions on magnesium road wheels in an effort to enhance their mechanical performance. Initially, a numerical model of a wheel and tire assembly incorporating material in-homogeneity within the wheel was developed to complete dynamic impact test simulations. Impact was investigated between a rigid striker and the wheel assembly. To reduce the complexity of the model and hence computational time for analysis, the tire was removed from the model and an approximate 20% reduction in the initial kinetic energy of the striker was considered to account for the tire removal. Experimental investigations for dynamic impact testing were completed on a similar magnesium road wheel and the observations from these experiments were utilized in validating the developed numerical model. Wheel cornering fatigue test simulations were performed utilizing two different approaches. In the first method involving static stress analysis, loads in different bending directions were applied to the hub, whereas in the second method with a dynamic stress analysis, a rotating bending moment was applied to the hub. Predictions from both the static and dynamic stress analyses were applied to the Goodman linear fatigue failure criterion for multi-axial stresses to assess the fatigue life of the wheel. The numerical model was capable of predicting exactly the location of fatigue crack growth. Design modifications were applied to the wheel model, which resulted in an improved fatigue performance of the forged magnesium wheel.

3. RESEARCH OBJECTIVES

Based upon a thorough analysis of the obtained literature, the following findings were obtained:

- 1) The mining industry demands the use of multi-piece wheels on mining vehicles due to various reasons discussed in chapter 2 of this thesis. Unfortunately, most of the incidents / fatalities that occur in the industry are found to be associated with multi-piece wheels and most specifically three-piece wheels as documented in the obtained literature.
- 2) The rationale associated for these incidents were maintenance personnel failing to follow safety guidelines. In some incidents, the mechanical degradation of the wheel as a result of impact or damage was found to initiate failure.
- 3) Numerical analyses to enhance the mechanical performance of road wheels have been previously completed. For mining wheels, no numerical investigations relating to the assessment of wheel performance under different loading conditions or rather enhancement of wheel's mechanical performance has been attempted. Additionally, to the best of author's knowledge, no finite element model of a multi-piece mining wheel has ever been developed.

To address the above findings from the literature review, various objectives for this current study were defined and are specified as:

- 1) A three-piece mining wheel assembly will be selected to complete the proposed experimental and numerical investigations of this study.
- 2) Experimental testing involving the application of a bending load on the mining wheel to follow the SAE J1992 protocol in static loading condition will be

completed at the University of Windsor to assess the mechanical performance of the wheel assembly.

- 3) A finite element model of the three-piece wheel incorporating all wheel geometry aspects, elastic material behaviour and proper contact between all wheel components will be developed. The experimental testing will be simulated on the developed model numerically using LS-DYNA.
- 4) Numerical predictions from the simulation of the experimental test will be compared to observations from the experiment to validate the numerical model.
- 5) The validated numerical model will be utilized to perform numerical analyses involving the SAE J1992 wheel cornering fatigue test. Predictions from these analyses will be used to assess the fatigue performance of the three-piece wheel assembly.

4. EXPERIMENTAL INVESTIGATIONS

Experimental testing with the application of a quasi-static loading through the mounting ring of the wheel was performed following the testing procedure prescribed in the wheel cornering fatigue test standard SAE J1992 to understand the state of stress on the wheel under simulated SAE J1992 tests. The entire testing procedure was repeated four times. The fatigue testing apparatus at the University of Windsor did not have the facility to apply the boundary conditions specified in the SAE J1992 protocol and as a result experiments were conducted under quasi-static loading condition in contradiction to the specified rotating dynamic bending loading. This experimentation necessitated the manufacture of auxiliary fixtures such as a shaft to apply the bending load onto the wheel, an adapter plate to fasten the shaft to the mounting ring of the wheel, and other wheel supporting fixtures to hold the wheel in position during experimentation. Additionally, to observe the strain distribution on the apparatus, ten strain gauges were mounted on different locations of the wheel and shaft as illustrated in Figures 4.2(a) and 4.2(b). These locations were selected based upon strain magnitudes and high strain gradients predicted by the numerical analyses of the experimental tests.

4.1. Manufacture of auxiliary fixtures

4.1.1. Loading shaft

The loading shaft was the structural member that transmitted the load from the hydraulic actuator to the wheel through the adapter plate. The shaft was manufactured from AISI 4140 [42] steel based upon design calculations (provided in Appendix A) to support a load of 22 kN, which is equal to the load on one of the rear axles of the mining vehicle the wheel is intended for use. The diameter of the shaft was 100 mm and the length of the shaft was 700 mm. The shaft was press fitted into the bore of the adapter plate and this assembly was fastened to the wheel utilizing one inch diameter bolts, in such a way that the centreline of the assembly was inline with the centreline of the wheel. A quasi-static bending load was applied in a direction perpendicular to the centreline of the wheel and shaft assembly at the far end tip of the shaft as illustrated in Figure 4.1(a).

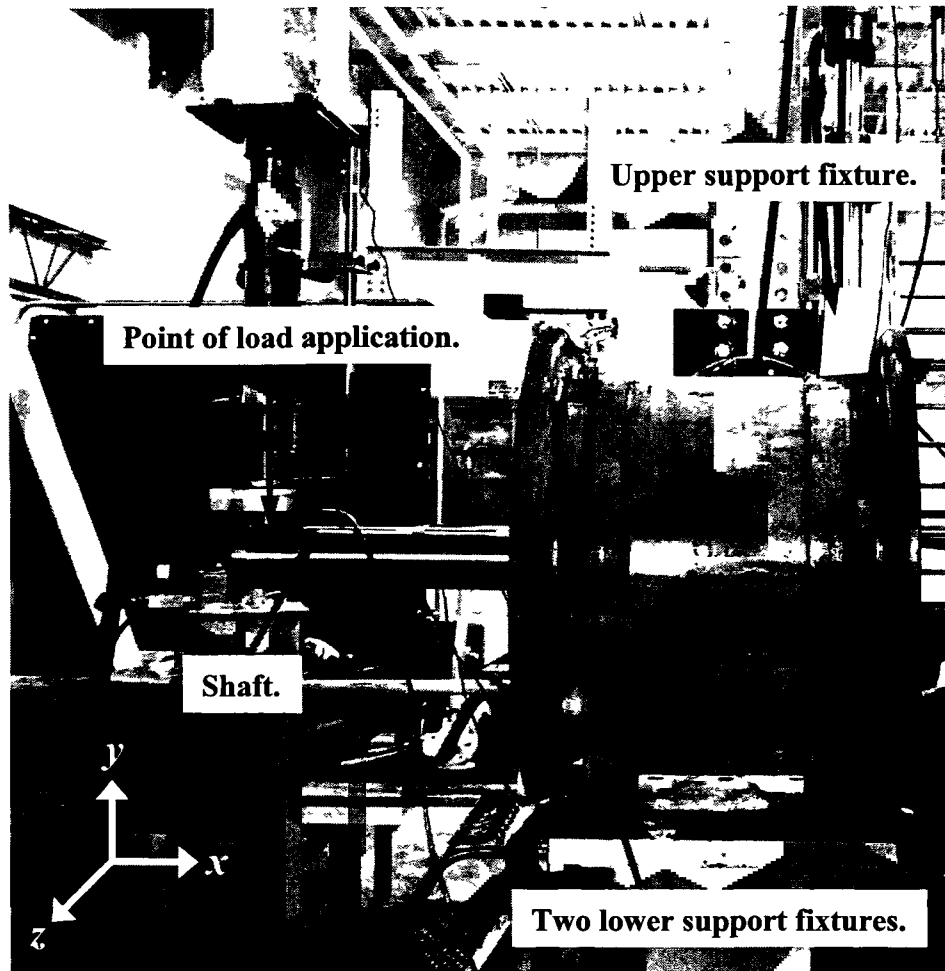


Figure 4.1(a). Experimental setup illustrating the shaft, the fixtures and the point of load application.

4.1.2. Adapter plate

The adapter plate was manufactured to transmit the applied load from the shaft to the wheel assembly. The adapter plate was a thick cylindrical plate, 350 mm in diameter, slightly larger than the bolt circle diameter of the mounting ring. The adapter plate had a thickness of 120 mm and was constructed of AISI 1018 steel [42]. The dimensions of the plate were based on design considerations mentioned in Appendix A. The adapter plate had twenty holes (one inch diameter) threaded in an identical pattern to that of the mounting ring. A bore with a diameter of 100 mm was manufactured into the centre of the adapter plate to accommodate the shaft. Figure 4.1(b) illustrates the position of the adapter plate in the testing apparatus. Additionally, the positioning of the shaft in the centre of the adapter plate can be observed.

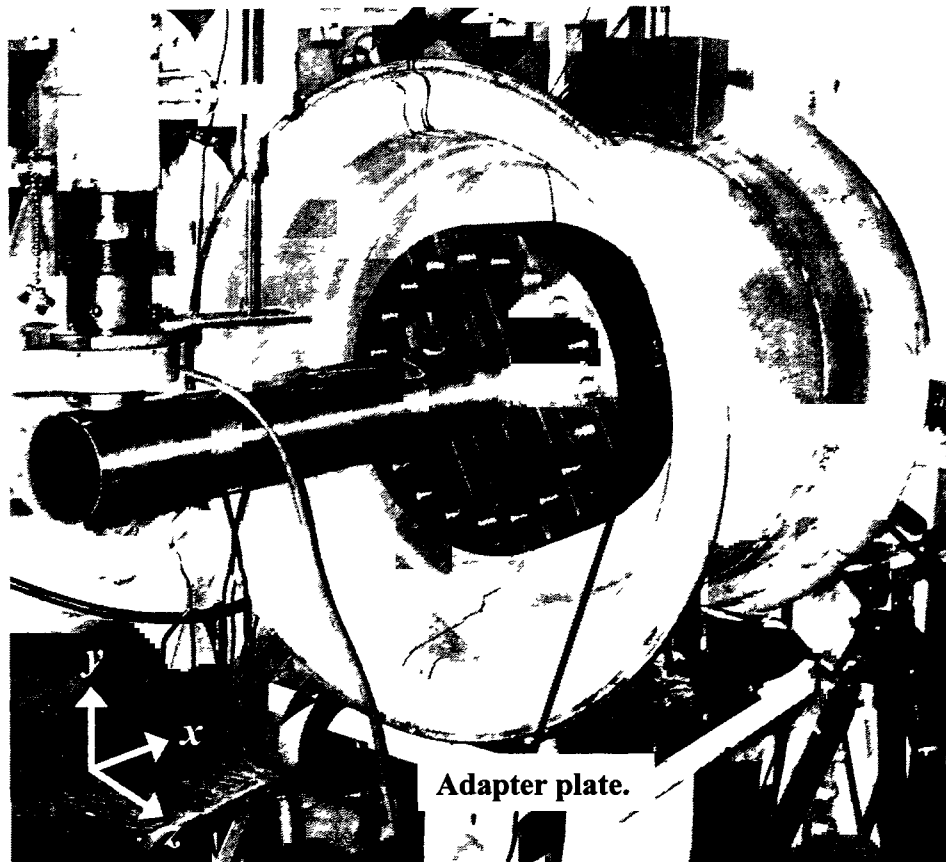


Figure 4.1(b). Experimental setup illustrating the adapter plate.

4.1.3. Wheel supporting fixtures

Three wheel supporting fixtures were manufactured to maintain the wheel in a fixed position during testing. Two lower support fixtures to support the wheel from the bottom, on the two flanges and one upper support fixture to hold the upper portion of the flange which is furthest from the point of load application, were constructed. The fixtures were flat on one side and had a curved profile on the other side to exactly match the curvature on the flanges of the wheel. The fixtures were manufactured out of AISI 1018 steel [42]. Calculations used to design the wheel supporting fixtures are provided in Appendix A.

4.2. Configuration of the data acquisition system

The data acquisition system (DATASCAN) was setup to accommodate ten strain gauges, a load cell and a linear variable differential transformer (LVDT). The load cell and the LVDT were mounted on the enerpac hydraulic cylinder, to measure the load on the wheel and the displacement of the shaft respectively. The resistance on the load cell was 350Ω and voltage rating was 2 mV. The load cell had a measurement range of 110 kN and after connecting the load cell to the data acquisition system, it was calibrated using a Tinius Olsen compression testing machine. The measuring range of the LVDT utilized was 150 mm. The system was capable of recording data at 1 Hz.

4.3. Strain gauge application

The strain gauges used in this experimentation were Omega precision strain gauges with serial number SGD-3/350-LY11. The strain gauges had a nominal resistance of 350Ω and a maximum voltage rating of 9.5 V. The strain gauges were adhered to the testing apparatus through the following process; grinding of the auxiliary fixtures and the wheel components was first completed to remove any form of paint; the surface was then treated with isopropyl alcohol to remove any grease or oily content on the surface; the surface was cleaned by gently rubbing with mild acetic acid after which a neutralizer was applied to remove any moisture present. The strain gauges were carefully removed from the packaging and fastened to the wheel with a small amount (one drop) of M-Bond 200 adhesive manufactured by Davidson Measurement Pty. Ltd. The adhesive selected has been certified by VISHAY Micro-Measurements for large deformations on the order of 60,000 microstrain if utilized with appropriate strain gauges. The accuracy of the measured strains depended on the thickness of the adhesive layer that existed between the strain gauges and the wheel and hence it was ensured that just a thin layer of adhesive existed. Figures 4.2(a) through 4.2(c) illustrate the positions of the strain gauges on the testing apparatus.

Three strain gauges (1L1, 1L2 and 1L3) were mounted on the outer surface of the mounting ring, three strain gauges (1L4, H5 and H6) on the removable side flange and two strain gauges (H7 and H8) on the fixed flange of the wheel base. The strain gauges on the mounting ring were mounted along the direction of the y -axis; whereas, the

strain gauges on the flanges of the wheel were mounted in a radial direction. Additionally, two strain gauges (2L1 and 2L2) were fastened to the shaft to measure strains in the axial direction along the x -axis.

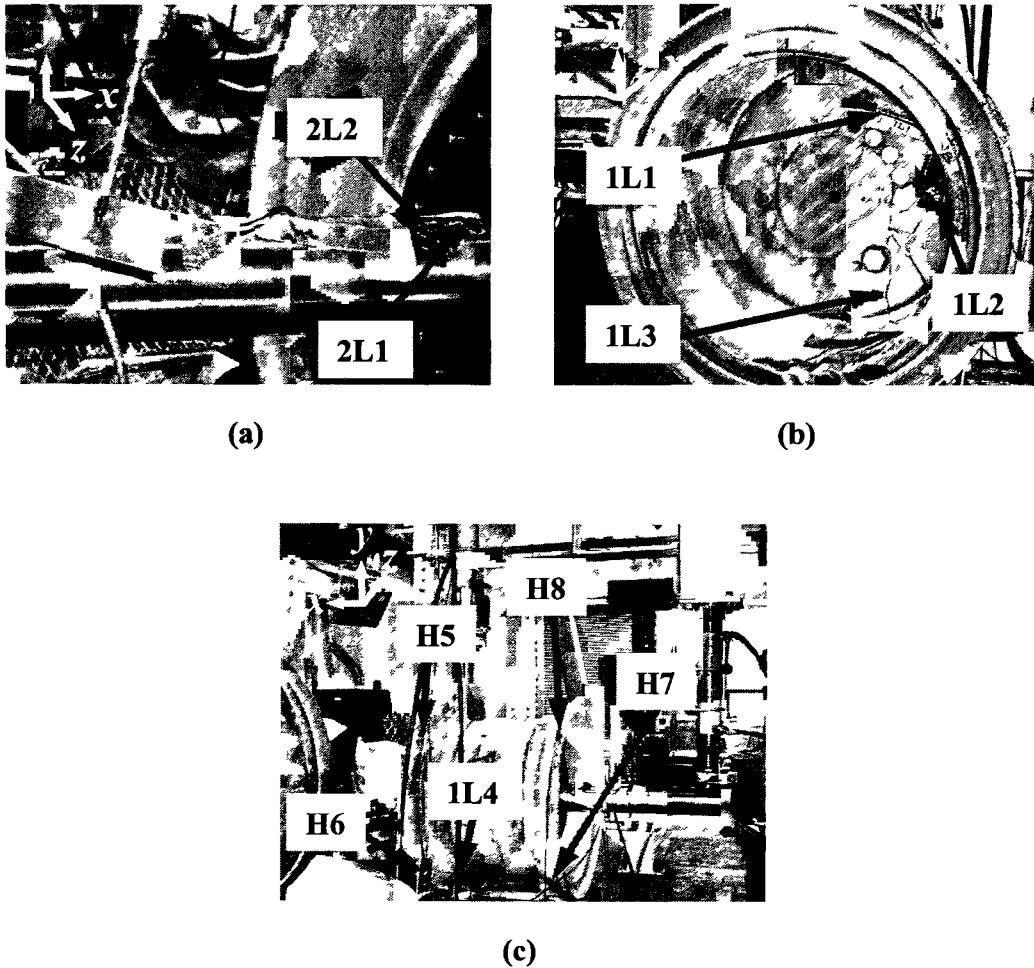


Figure 4.2. Positions of strain gauges on the testing apparatus, (a) Positions of strain gauges on the shaft, (b) Positions of strain gauges on the mounting ring, (c) Positions of strain gauges on the wheel base and the removable side flange.

4.4. Setup of the ARAMIS system

ARAMIS is a non-contact optical three dimensional large deformation measurement system developed by GOM mbH, Germany. The ARAMIS system is particularly suitable for three-dimensional deformation measurements under static and dynamic loads in order to analyze deformations and strains [53]. The system is capable

of analyzing, calculating and documenting material deformations and the ability of the system to graphically represent the measured results provides an optimum understanding of the behaviour of the object to be studied. ARAMIS recognizes the surface structure of the object through digital camera images and allocates coordinates to the image pixels. The initial condition of an apparatus where typically no load exists is referred to as the reference condition and the first coordinates are assigned when recording the reference condition. With relevance to the current investigation, the position where the mining wheel was not subjected to any bending load was recorded as the reference condition. When the actual loading begins, ARAMIS records further series of images depending upon a preset frequency. The ARAMIS system compares the digital images at different steps and calculates the displacement and the deformation in the region of a testing apparatus prepared for the optical strain evaluation.

The region of the mounting ring symmetric to the vicinity of strain gauge 1L2 as illustrated in Figure 4.3 was selected within the wheel assembly for optical strain measurement. The mining wheel investigated in this research had a homogeneous surface and as a result of that, the region to be observed with the ARAMIS system had to be painted white followed by spots of black sprayed on the white background for the camera to be able to recognize and allocate coordinates to the image pixels. A typical black spot in this region was approximately the size of one pixel.

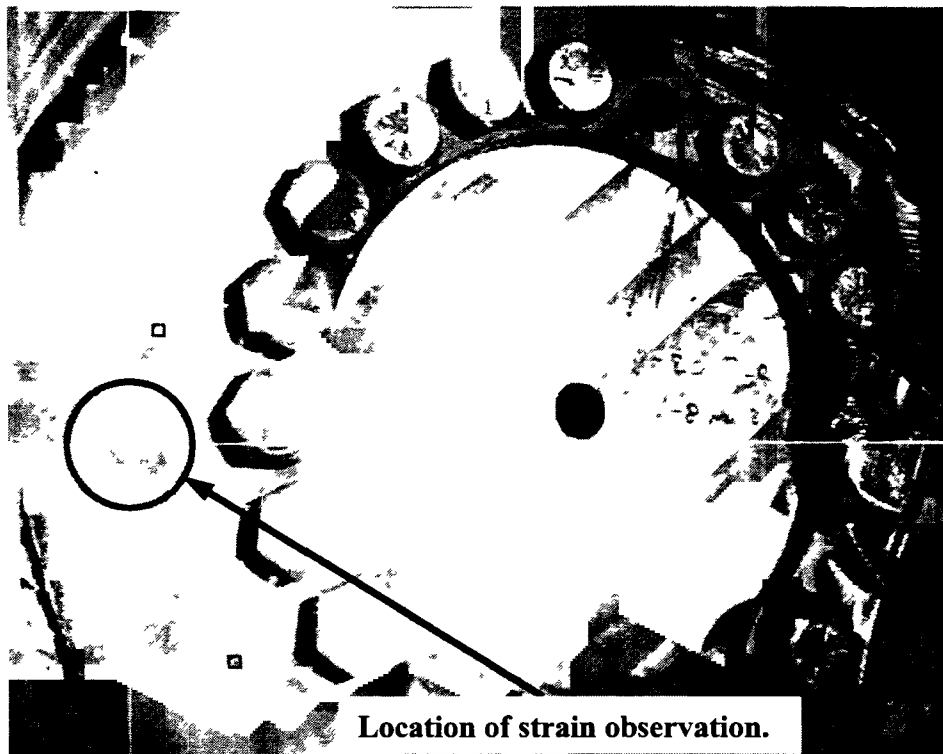


Figure 4.3. Location of strain observation by the ARAMIS system.

The region of the wheel selected for optical strain investigation measured approximately 300 mm in length and 250 mm in width. Hence, in order to calibrate the ARAMIS system for this field of view, a calibration panel of dimensions 350 mm in length and 280 mm in width was used which led to a total measuring volume of $350 \times 280 \times 280 \text{ mm}^3$. The focal length of the lens used in the cameras was 12 mm with a fully closed aperture. The cameras were at a distance of 280 mm apart and at an angle of 25° . The measuring distance, which is the distance between the front face of the camera support bar and the object of measurement, was set at 570 mm based on the ARAMIS manual. Specimen lighting was provided by a 650 watt halogen lamp. The system was configured to capture data every 5 seconds.

4.5. Setup of the experimental test

The experimentation was completed in the structural laboratory at the University of Windsor. The capacity of the loading frame utilized in this study to apply the load on the wheel assembly was approximately 900 kN. A large steel column was bolted to the

concrete floor of the laboratory, and the supporting fixtures that were utilized to hold the wheel in position from the bottom of the wheel were welded to this column. The upper support fixture was placed on top of the flange, farthest from the point of application of the load and the support's motion was arrested to ensure negligible movement of the flange. Figure 4.1 illustrates the setup utilized for this experimental testing. An enerpac hydraulic cylinder with a stroke of approximately 250 mm and a loading capacity of 900 kN was positioned at the far end tip of the shaft to load the system up to 22 kN. The load was gradually applied from 0 to 22 kN in a span of approximately 7 minutes. After reaching that maximum load, the system was held undisturbed in that state for approximately one minute after which the system was unloaded. All strain gauges connected to the data acquisition system along with the load cell and LVDT were recording data at the rate of 1 Hz and ARAMIS was recording data at the rate of 0.2 Hz. The entire experimental testing was captured using a Sony (HDR-SR10) high definition camcorder.

4.6. Experimental results

4.6.1. Results from the data acquisition system

Strains measured at various locations of the wheel were plotted against bending load to establish the relation between the two parameters. A linear relationship existed between the strains measured at all ten locations on the wheel and the bending load. This linear relationship between the strains and the bending load was expected as the wheel was loaded within the elastic limit of the material throughout the period of testing. Observations from test to test were generally consistent and hence a good repeatability was established. Observations from the second test were calculated and graphed as a representative of all four tests and are presented in Figure 4.4(a). Strain versus bending load profile for all the four experimental tests are presented in Appendix B.

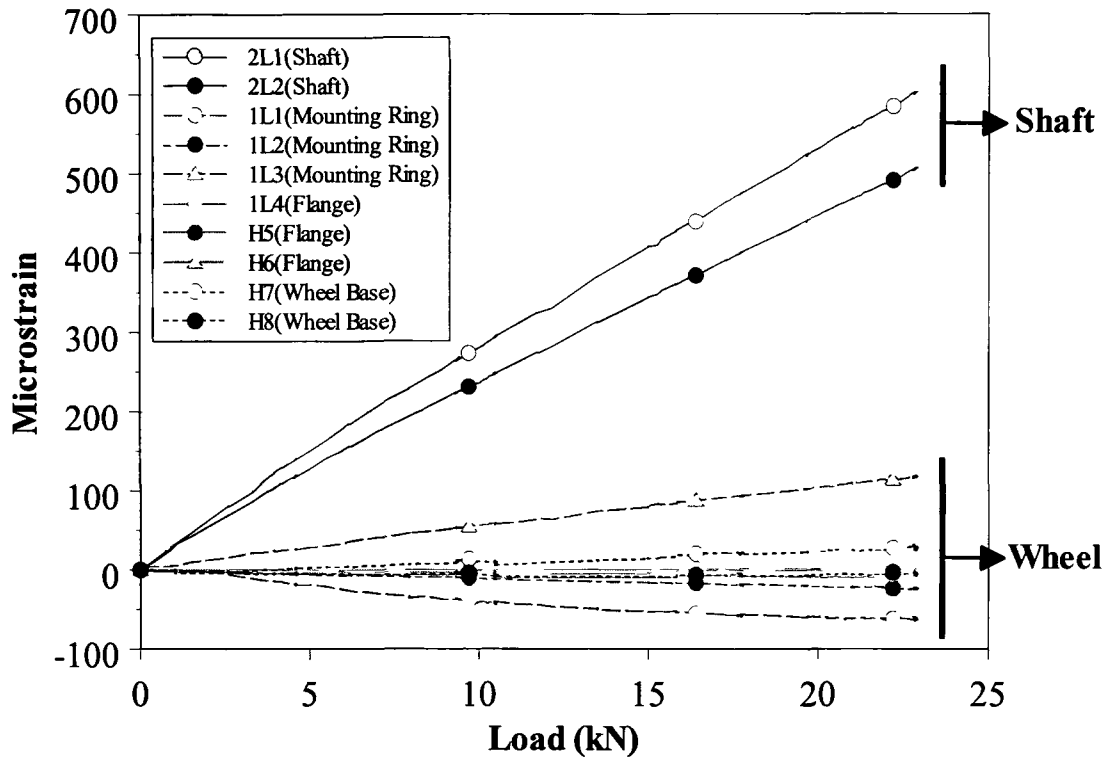


Figure 4.4(a). Strain versus load profiles for all ten strain gauge positions from the second experiment.

The strains measured at different locations on the testing apparatus are illustrated in Figure 4.4(a). The two curves 2L1 and 2L2 correspond to the two strain gauge positions on the shaft. The remaining eight curves (1L1, 1L2, 1L3, 1L4, H5, H6, H7, and H8) represent the strains measured at different locations within the wheel assembly. In an effort to provide better readability of the strains measured within the wheel assembly, the eight curves corresponding to the wheel assembly are presented in Figure 4.4(b).

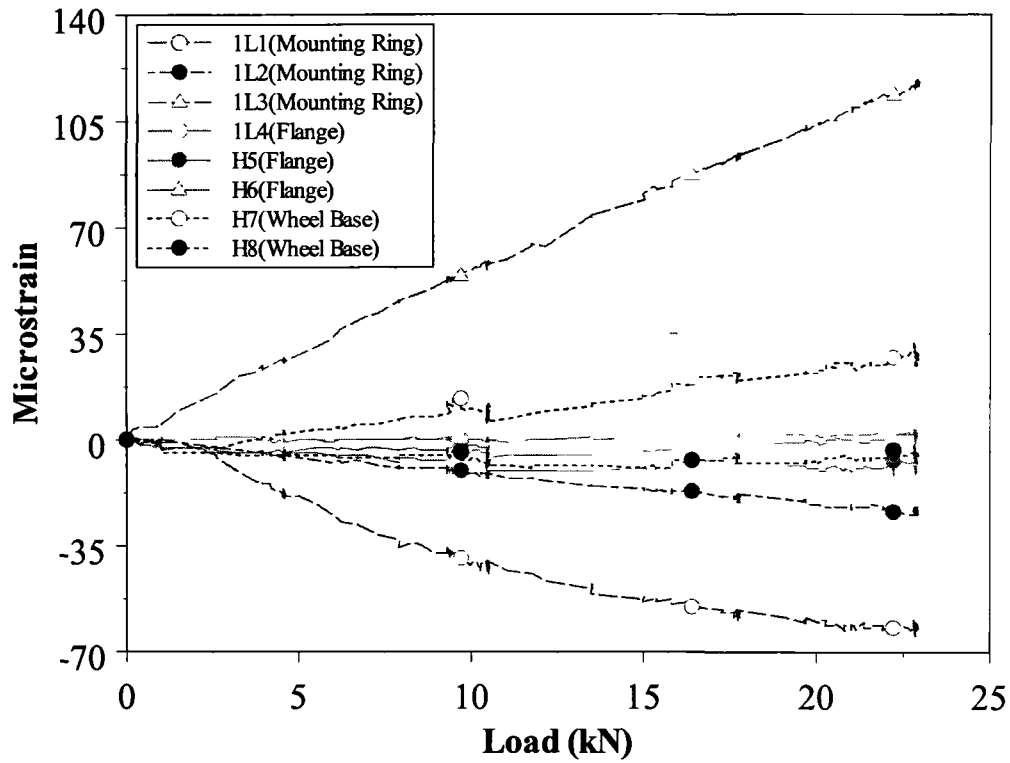


Figure 4.4(b). Strain versus load profiles for strain gauge positions (wheel assembly) from the second experiment.

An average of the maximum strain values for all ten positions of the strain gauges from all four experiments, which typically occurred at the peak load was calculated and are provided in Table 4.1.

Table 4.1. Average strain results from the four experiments during peak load application.

<i>Strain gauge positions on the wheel assembly</i>	<i>Strain from data acquisition device (microstrain)</i>	<i>Position on the wheel based on component of the wheel assembly</i>
2L1	592	Shaft position 1
2L2	494.75	Shaft position 2
1L1	-61.25	Mounting ring position 1
1L2	-20.5	Mounting ring position 2
1L3	104.25	Mounting ring position 3
1L4	3.25	Removable flange position 1
H5	-4.75	Removable flange position 2
H6	3.25	Removable flange position 3
H7	29	Wheel base position 1
H8	-2	Wheel base position 2

4.6.2. Discussions

Maximum strains were found to occur in the shaft, which is expected, due to the fact that, shaft acted as the method of transfer of load to the wheel. The shaft was subjected to significantly high bending, shear, and transverse shear stresses. These high stresses were a result of the positioning of the shaft in the load path and the considerably smaller geometry as compared to the adapter plate and other wheel components. Additionally, strain gauges were mounted at a significant distance from the neutral axis of the shaft. A maximum strain of approximately 600 microstrain was measured by the strain gauge at position 2L1. The strain gauge at position 2L2 observed a slight reduction in the measured strain from approximately 600 microstrain to 500 microstrain. The reason for the reduction of measured strain values from 2L1 to 2L2 is that, 2L1 appeared farther from the point of load application than 2L2 and hence 2L1 was subjected to a greater bending moment in comparison with 2L2. Both the strain gauges measured strains on the upper fibres of the shaft in the axial direction (along x -axis) and hence the tensile nature of the measured strains is justified.

The load is transferred from the shaft to the wheel assembly through the mounting ring. The strain gauges mounted on the mounting ring 1L1, 1L2, and 1L3 measured strains along y -axis. The strain gauge at location 1L3 measured the highest strain of approximately 100 microstrain within the wheel assembly, but was significantly lower than the strains measured in the shaft and this is expected due to the position of its occurrence (next to the shaft) in the load transfer path. The nature of the loading applied to the wheel assembly is expected to cause tensile strains in the y -axis direction on the outer surface of the mounting ring. However the positioning of the upper support fixture on top of the removable side flange restricted the wheel from moving upwards. This causes the strains to gradually shift from tensile to compressive (on the outer surface of the mounting ring) when moved upward on the mounting ring. Hence the strain gauge at location 1L2 measured a strain of approximately 20 microstrain (compressive) as it is above the neutral axis of the wheel assembly. Additionally, the magnitude of strain is low as a result of this position being located close to the neutral axis (approximately 10 mm upward from the neutral axis). The trend in variation of the nature of strain measured on the outer surface of the mounting ring from bottom upward is clearly evident from the strain measured at location 1L1. The measured strain at 1L1 was approximately 60 microstrain (compressive) as a result of the completely arrested translational degree of freedom of the wheel in y -direction.

The loads transferred to the flanges of the wheel were not enough to cause significant strains. Hence the strains measured by the strain gauges located on the flanges of the wheel were low with the strain gauges on the removable side flange 1L4, H5, and H6 measuring strain values of 3.25 (tensile), 4.75 (compressive), and 3.25 (tensile) respectively. Nonetheless, the nature of the strains was compressive on the upper portion of the flange and tensile on the lower portion which is consistent with the mounting ring strain observations.

Within the fixed flange of the wheel assembly, the strain at location H7 was measured as 29 microstrain (tensile). This strain gauge was located in the vicinity of the lower support fixture closest to the point of load application. The nature of the applied bending load along with the resistance offered by the lower support fixture from the bottom caused a considerable elongation of the flange along the radial direction which

resulted in a tensile strain as would be expected. The strain gauge at location H8 measured a value of 2 microstrain (compressive) which was negligible compared to the strain at other locations.

4.6.3. Results from the ARAMIS system

Figure 4.5 illustrates the output from the ARAMIS system. The intersection of the horizontal section and the vertical section is the location which is symmetric to position 1L2 about the yz plane.

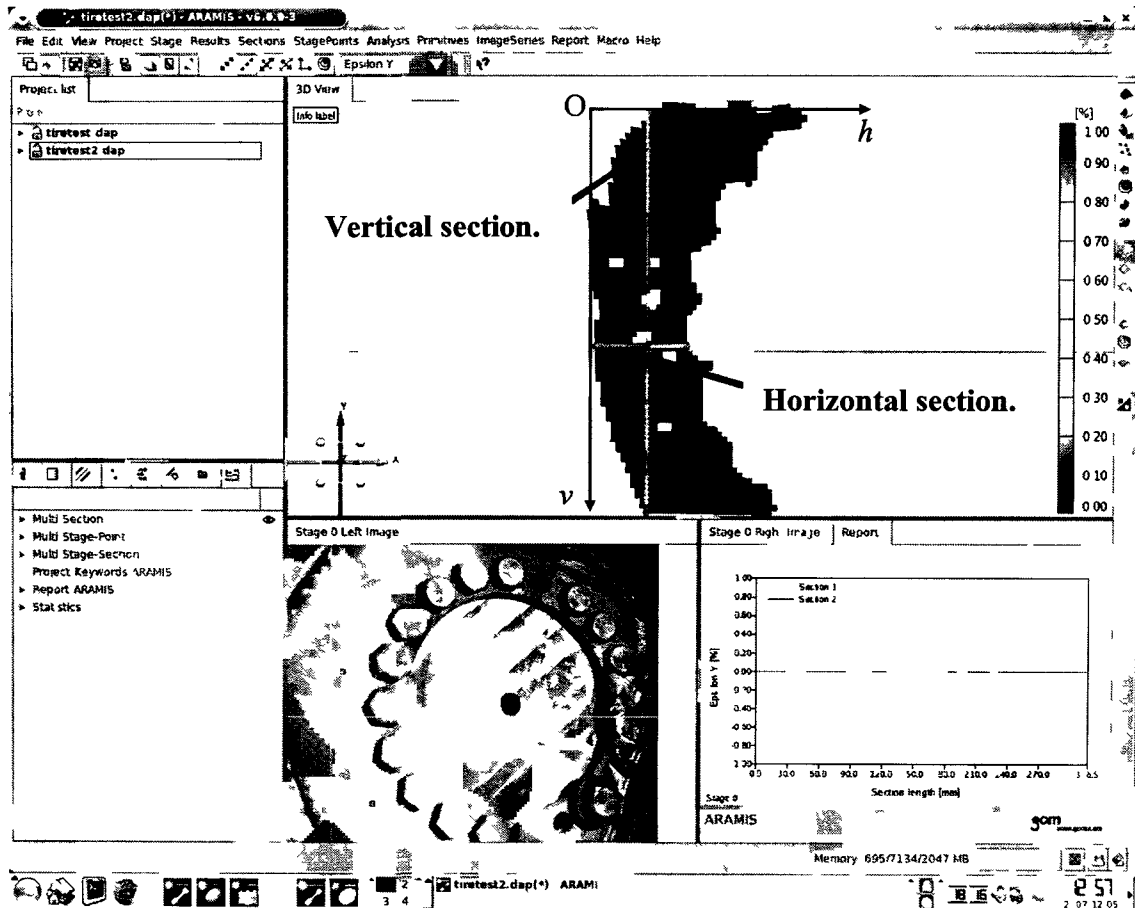


Figure 4.5. Output from the ARAMIS system illustrating the method of strain measurement

Technical strains along the horizontal and the vertical sections for all the four experiments were observed. The effective strain, as presented in equation (4.1), has been

used to assess the results from the ARAMIS system. ε_1 , ε_2 , and ε_3 are the principal strain values of the measured technical strains.

$$\bar{\varepsilon} = \frac{\sqrt{2}}{3} \cdot \sqrt{(\varepsilon_1 - \varepsilon_2)^2 + (\varepsilon_2 - \varepsilon_3)^2 + (\varepsilon_3 - \varepsilon_1)^2} \quad (4.1)$$

Observations from the ARAMIS system for the second experiment are provided in Figure 4.6(a) for the horizontal section and Figure 4.6(b) for the vertical section. It was expected that the strains measured at peak load (22 kN), on the horizontal and the vertical sections at the point of intersection would be identical and approximately correspond to the strain measured by strain gauge 1L2. The point of intersection existed at 40 mm from the reference point 'O' measured along the h -axis on the horizontal section and 190 mm measured along the v -axis on the vertical section. Strains measured at the corresponding points on the horizontal and vertical sections during the peak load were -30.3 microstrain and 249.7 microstrain respectively. Strain values at the intersection point in other experiments were also calculated utilizing the same approach and are presented in Table 4.2.

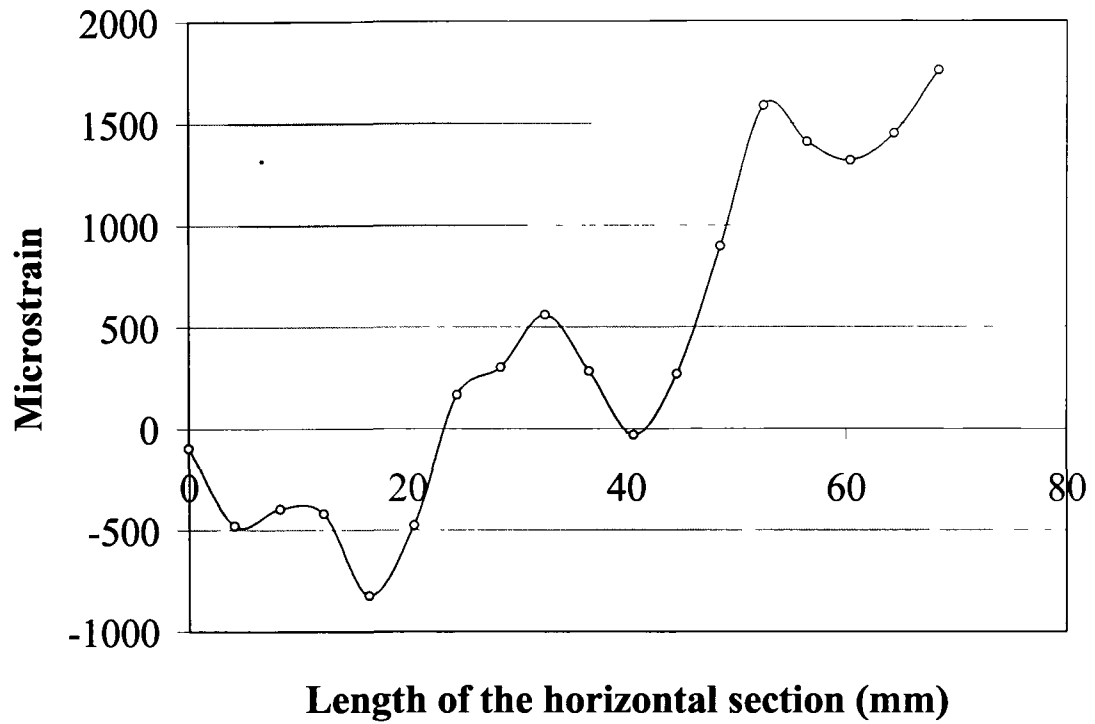


Figure 4.6(a). Strain versus length of the horizontal section from the second experiment.

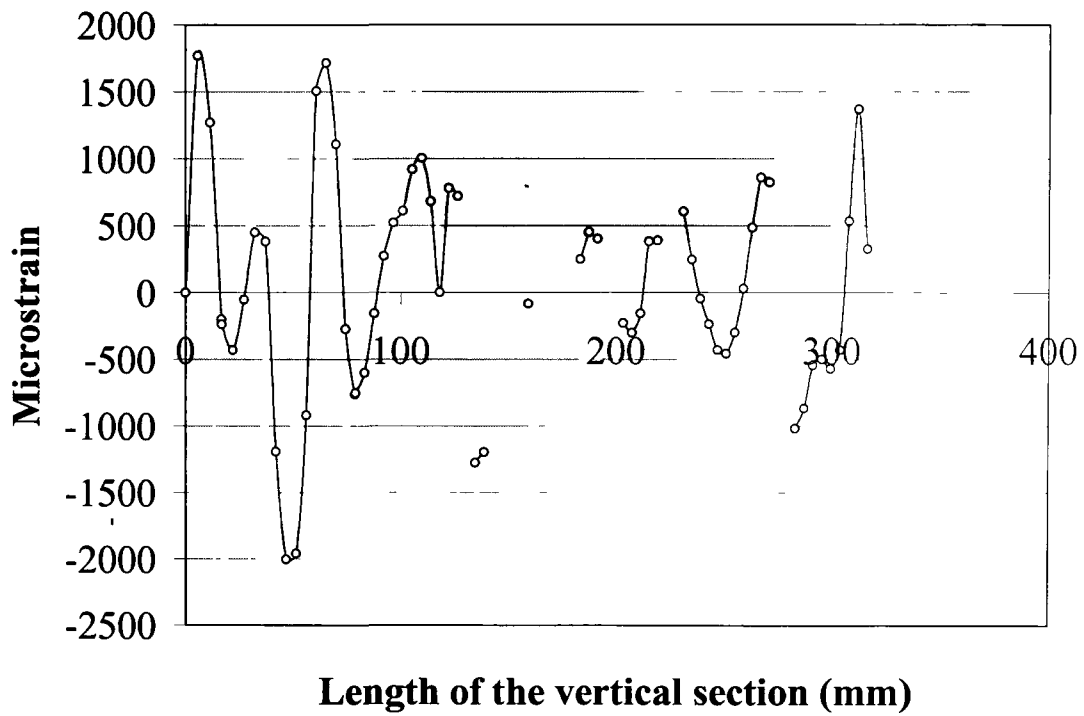


Figure 4.6(b). Strain versus length of the vertical section from the second experiment.

Table 4.2. Strains from the ARAMIS system.

Strains (in microstrain) from ARAMIS corresponding to mounting ring position 2							
Experiment 1		Experiment 2		Experiment 3		Experiment 4	
Horizontal	Vertical	Horizontal	Vertical	Horizontal	Vertical	Horizontal	Vertical
-162.84	-129.17	-30.30	249.67	0.00	-0.34	326.07	323.53

4.6.4. Discussions

Although it was expected that the strains measured from the horizontal and the vertical sections at the point of intersection should be closely coinciding with each other, the values from Table 4.2 indicate that there existed a significant variation between these two values. Moreover the results from all the four experiments varied significantly and as a result no repeatability of strain measurement could be established from test to test. Additionally there is no consistency among the strain values measured by the ARAMIS system and the measured strain at strain gauge position 1L2. This discrepancy in the results necessitated further investigation into issues related to application of the ARAMIS system for strain measurement in this current work. Upon a thorough investigation, it was established that the paint spray pattern used on the wheel was not appropriate for the selected field of view. For the field of view utilized in this testing, a typical black spot in the region of strain observation should have covered at least three to four pixels of the camera image. Unfortunately, after a thorough post processing of the results from the ARAMIS system, it was observed that the black spots in the region of concern were approximately just one pixel size and as a result of this, the system was not able to allocate co-ordinates to the pixels properly. This was concluded to be the reason behind inaccurate strain measurements. A significant variation in measurement (noise in the graphs) and the lack of data at some positions observed in Figures 4.6(a) and 4.6(b) is also attributed to the same reason that the ARAMIS system was not able to appropriately locate black spots in the area of observation. Repeating the entire experimental testing procedure with a properly prepared specimen to obtain meaningful results necessitated further investigations into the preparation aspects of the specimen which was beyond the scope of this thesis. As a result, strain measurements from the ARAMIS system were not considered in any of the further investigations performed in this study.

5. FINITE ELEMENT MODELING OF THE EXPERIMENTAL TEST

5.1. Numerical model development of the three-piece wheel

5.1.1. Discretization of the wheel model

Computer Aided Design (CAD) data of the wheel were obtained from North Shore Industrial, through J & M Tires to develop a finite element model of the three-piece wheel assembly. All unnecessary entities from the CAD model were removed and the resultant cross-section of the wheel was imported into Finite Element Model Builder (FEMB), a finite element pre-processing software from Engineering Technology Associates Inc. (ETA). Taking advantage of the axi-symmetric nature of the wheel problem considered here, the obtained cross-section of the wheel was meshed with two dimensional shell elements and finally shell elements were revolved around the axis of the wheel to generate three dimensional hexahedral elements for the whole wheel model. All orthographic views and an isometric view of the completely discretized finite element model of the three-piece wheel are illustrated in Figure 5.1.

The model had 9 parts in total including the loading shaft, adapter plate and the supporting fixtures. All parts were assigned a solid section property with a fully integrated selectively reduced element formulation (element formulation #2 in LS-DYNA). Additionally, a simulation was repeated with a constant stress element formulation (reduced element formulation, element formulation #1 in LS-DYNA) specified to all components of the model except the mounting ring. This was conducted to assess the influence of element formulation on the observations obtained in the numerical simulations. The total number of nodes in the entire model was 169,884. The total number of elements in the model was 135,310, with 132,334 elements being hexahedral in geometry and the remaining 2,976 elements being pentahedral. Among these total number of elements, 108,128 elements belonged to the wheel assembly with 106,672 hexahedral elements and 1,456 pentahedral elements. The smallest element existed in the locking ring with a dimension of 1.3 mm. The largest element dimension which existed in the mounting ring near the bolt holes was equal to 18 mm. The discretized model had a high element quality with the largest aspect ratio being 7.45. An approximate estimation of the aspect ratios of the elements in the model was estimated

and is provided in Table 5.1. Approximately 17 % of the total number of elements with aspect ratios greater than 5 existed and that was considered acceptable. Warpage in elements was typically less than 5 degrees and the value of Jacobian of transformation from local to the global coordinate system was greater than 0.535.

Table 5.1. Aspect ratios of elements in the model.

Aspect Ratio	Number of elements
1.0 – 1.5	41222
1.5 – 2.0	6894
2.0 – 2.5	4920
2.5 – 3.0	4152
3.0 – 3.5	27320
3.5 – 4.0	22064
4.0 – 4.5	5684
4.5 – 5.0	-
5.0 – 5.5	14470
5.5 – 6.0	-
6.0 – 6.5	
6.5 – 7.0	6954
7.0 – 7.5	1630

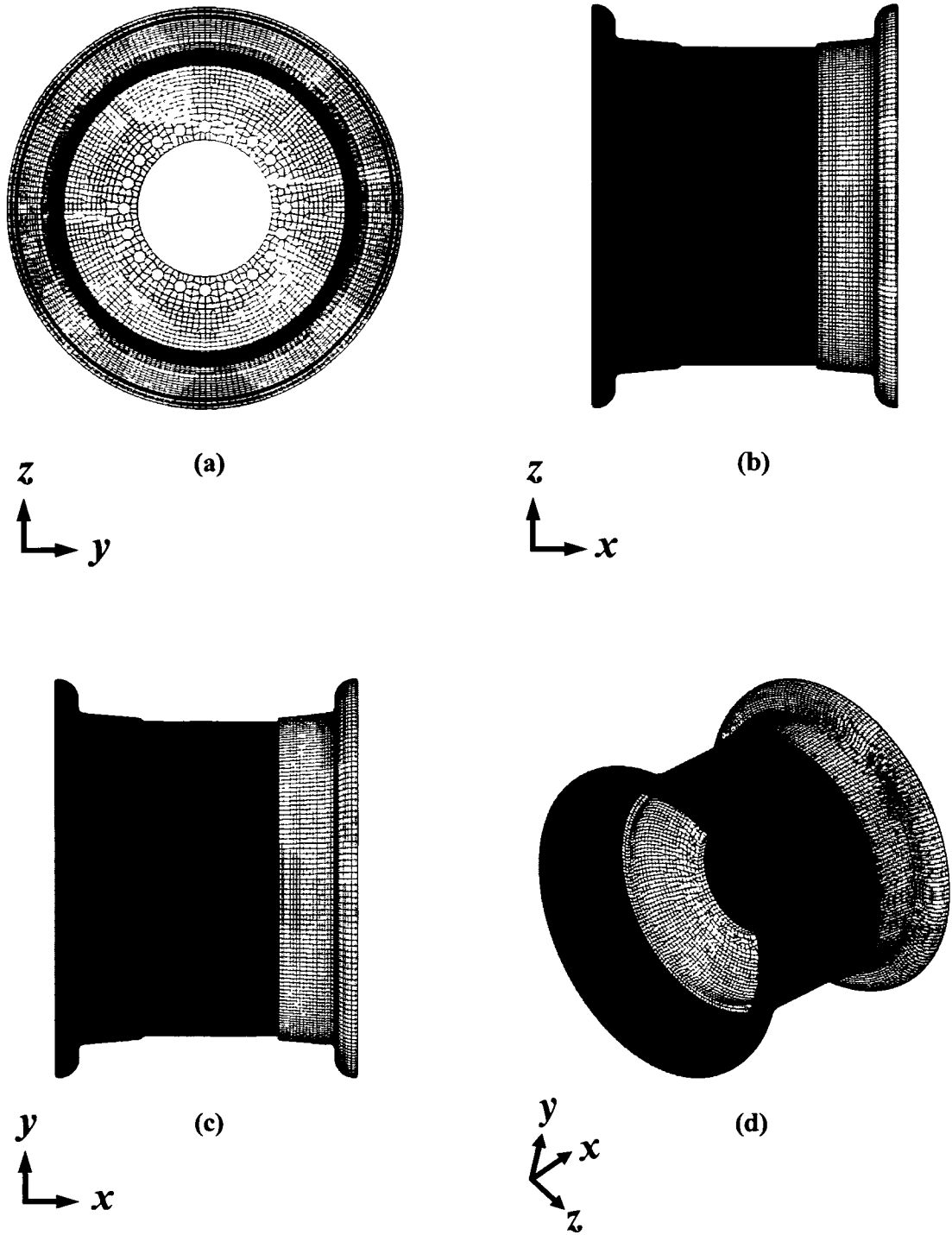


Figure 5.1. Discretized wheel model, (a) Front view of the discretized model, (b) Left side view of the discretized model, (c) Top view of the discretized model, (d) Isometric view of the discretized model.

5.1.2. Material models

An isotropic fully elastic material model was chosen for all components of the wheel and all auxiliary fixtures. ASTM A40 [54] is a general grade of steel used for mining vehicle wheels and its mechanical properties were specified in various input parameters of the material model. Mechanical properties of ASTM A40 [54] such as density, elastic modulus, and Poisson's ratio are 7870 kg/m^3 , 200 GPa, and 0.3 respectively. Values of the elastic material properties were assumed identical for all other steels used in the experimentation.

5.1.3. Contact definition

The contacting interfaces within the wheel model were modeled using a penalty based contact algorithm. This method places interface springs between the penetrating nodes and the contact surface in order to avoid penetration of the contacting interfaces. The static and dynamic coefficients of friction were specified as 0.35 and 0.25 respectively. The penalty scale factors were maintained at default values of unity. Throughout the entire simulation, there was no indication of nodal penetrations in all contact definitions. Additionally, to constrain the loading shaft to the adapter plate, and adapter plate to the mounting ring of the wheel, a penalty based tied contact algorithm was used in each case.

5.1.4. Application of boundary conditions

The lower support fixtures were fully restrained and a downward force of approximately 22 kN at maximum load was applied to the upper most nodes of the upper support fixture to simulate the boundary conditions from the experimental setup. Bolt holes of the mounting ring were constrained in all degrees of freedom. This was achieved by constraining all the nodes on the circumference of bolt holes to a central rigid shaft. A load of 22 kN was applied at the far end tip (same position as the experiment) of the shaft.

5.2. Simulation procedure

This problem was solved using an implicit time integration scheme as discussed in Appendix C. A static solution was considered with values for the displacement and energy convergence tolerances specified as 0.005 and 0.05 respectively. Simulations were completed on dell computer with an Intel Pentium T2300 dual core processor. The internal clock speed of the processor was 1.66 GHz. The computer had one gigabyte of RAM and sixty gigabytes of hard disc space. The simulations took approximately 4 hours each for completion.

5.3. Results of the simulation

Results from the simulation with selectively reduced element formulation and constant stress element formulation were observed to be consistent. As a result, results of the simulation with selectively reduced element formulation alone are provided in this section. Strains at element positions corresponding to each and every strain gauge was observed throughout the entire duration of the simulation. Strains for all these elemental positions were transformed to directions corresponding to strain gauges in the experiment. As completed for the experimental strain results, these transformed strain values from finite elements corresponding to every strain gauge location was plotted against applied bending load and illustrated in Figure 5.2(a). A linear relationship between strains and the bending load as seen in the experimental results was observed in all locations as expected because the system was subjected to the same load as in the experiment and additionally material model used was a fully isotropic elastic material model.

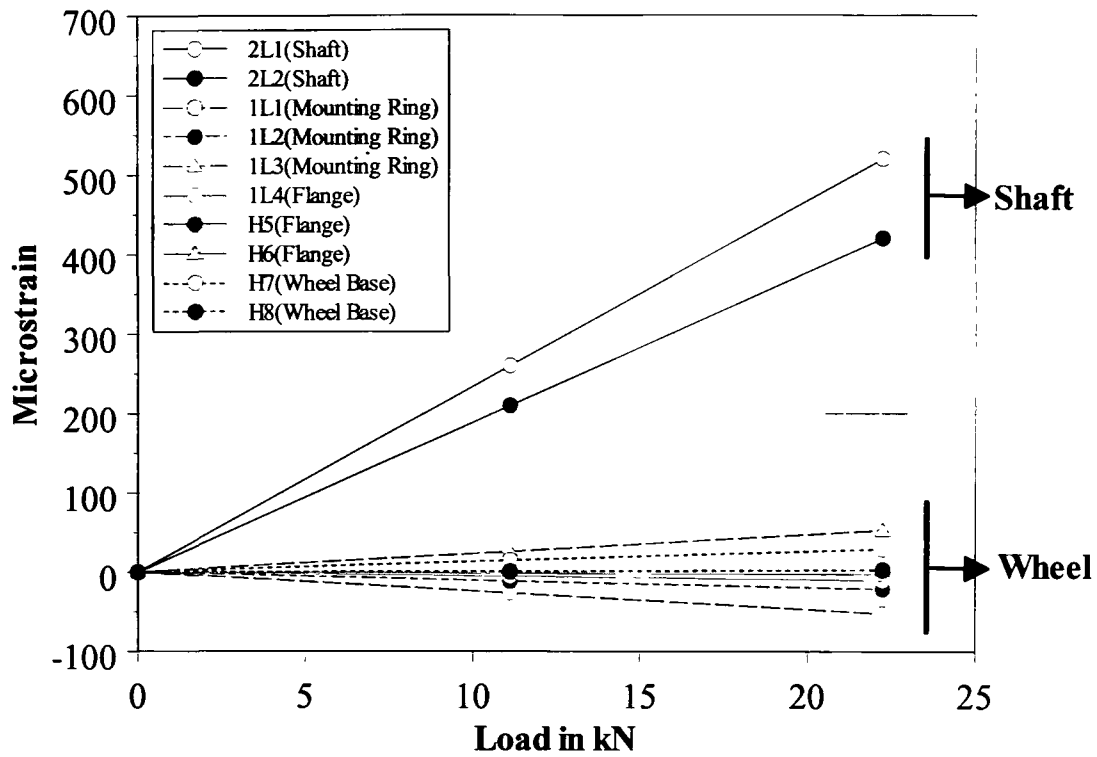


Figure 5.2(a). Strain versus load profiles from numerical predictions on the entire test apparatus.

As previously presented in the experimental results section, the strain curves corresponding to strain gauges on the wheel assembly alone are presented in Figure 5.2(b) in an effort to provide better clarity to the readers.

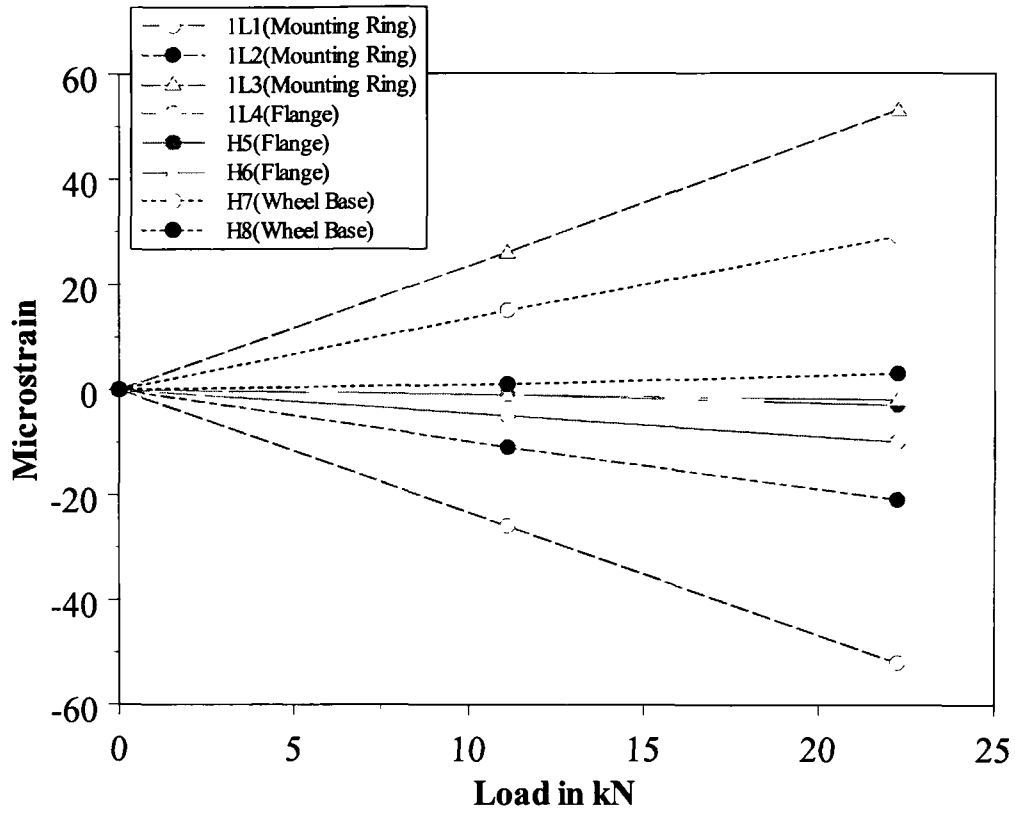


Figure 5.2(b). Strain versus load profile from numerical predictions on the wheel assembly.

An effective strain distribution state at peak loading on the testing apparatus, under bending loading is presented in Figure 5.3.

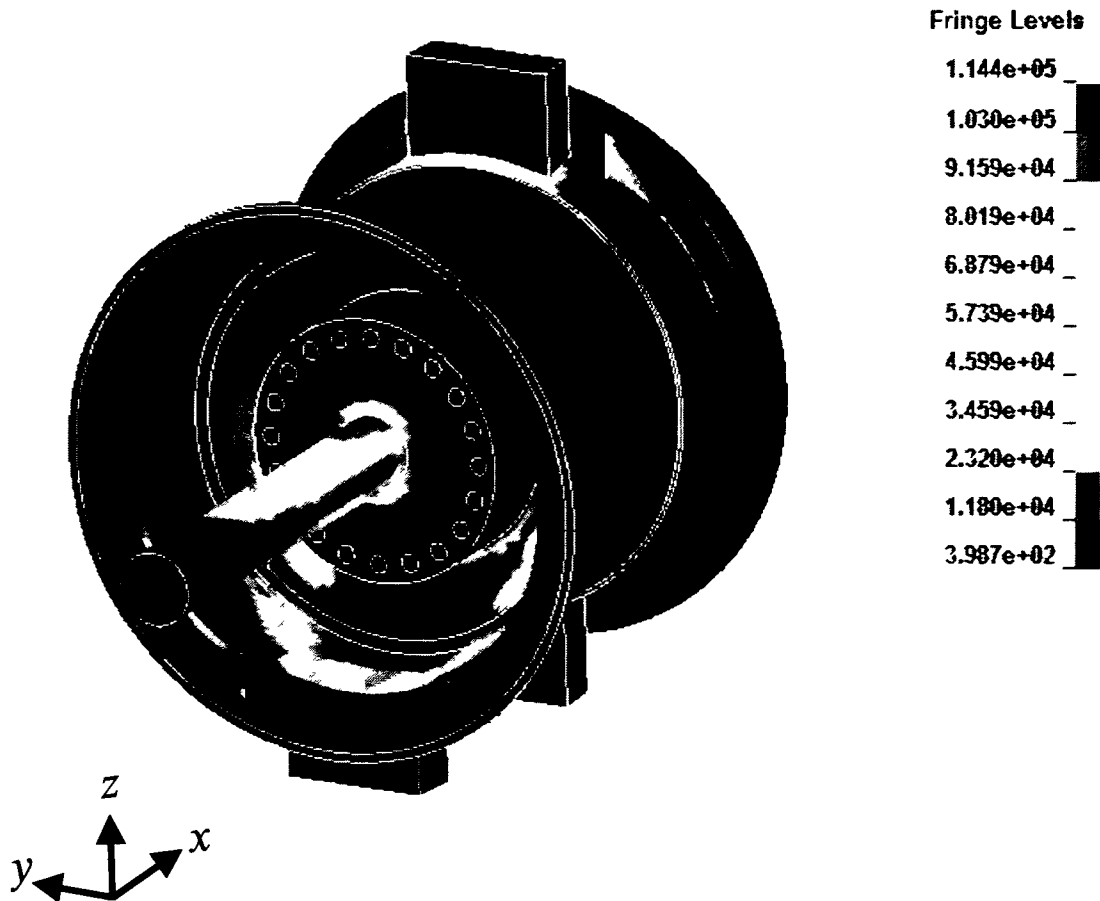


Figure 5.3. An effective strain distribution on the testing apparatus at maximum load.

The location of maximum strain occurred at the contact location between the wheel base and the support fixture closest to the end tip of the shaft where the bending load was applied. This location of maximum effective strain coincided with the location of maximum effective stress, which was observed to be approximately 114 MPa. Within the wheel assembly, the maximum strain was observed in the mounting ring and the corresponding stress was approximately 77 MPa. The stresses corresponding to the maximum strain locations were well below the yield strength of the material.

5.4. Discussions

Strains were generally under predicted by FEA when compared to the experimental observations. A maximum strain of approximately 520 microstrain (tensile)

was observed in the elements corresponding to the shaft position 2L1, followed by the shaft position 2L2 at 420 microstrain (tensile). This observation is consistent with the experimental observations. This consistency in observations is also found in strains measured at the mounting ring. The strains measured in different elemental positions corresponding to 1L1, 1L2, and 1L3 of the mounting ring were 52 microstrain (compressive), 21 microstrain (compressive), and 53 microstrain (tensile). Strains measured at elements corresponding to other locations on the wheel assembly were negligible compared to the strain at other locations.

6. VALIDATION OF THE FINITE ELEMENT MODEL

6.1. Comparison of numerical predictions with the experimental results

An average of maximum strain from all the four experiments for all the ten strain gauge positions was computed and is listed in Table 6.1. Additionally, for every strain gauge position, corresponding element strains from FEA, measured in the same direction as the strain gauge are provided. FEA was generally observed to under predict the strains in this study.

Table 6.1. Comparison of average strain values from the four experiments and strain predictions of FEA at the peak load.

<i>Strain gauge positions on the wheel assembly</i>	<i>Strain from the data acquisition system (microstrain)</i>	<i>Strain from FEA (microstrain)</i>	<i>Percentage error in strains (%)</i>
2L1 (shaft position 1)	592	520	12.16
2L2 (shaft position 2)	494.75	420	15.11
1L1 (mounting ring position 1)	-61.25	-52	15.10
1L2 (mounting ring position 2)	-20.5	-21	2.44
1L3 (mounting ring position 3)	104.25	53	49.16
1L4 (removable flange position 1)	3.25	-10	407.69
H5 (removable flange position 2)	-4.75	-3	36.84
H6 (removable flange position 2)	3.25	-2	161.54
H7 (wheel base position 1)	29	29	0
H8 (wheel base position 1)	-2	3	250

The percentage error in the strains measured by FEA as compared to experiments for each strain gauge position presented in the table was estimated utilizing the equation (6.1).

$$\text{Percentage error} = \frac{(\epsilon_{FEA} - \bar{\epsilon}_{EXP})}{\bar{\epsilon}_{EXP}} \cdot 100\% \quad (6.1)$$

where,

$$\bar{\epsilon}_{EXP} = \frac{\sum_{i=1}^4 \epsilon_{EXP}}{4} \quad (6.2)$$

The strains measured from experiments as well as the strains observed from FEA used in the calculation of percentage error correspond to the strain at peak load (22 kN).

6.2. Discussions of strain versus load profiles from experiments and finite elements

Strain versus bending load from all four experiments and finite elements for all strain gauge positions was compared and Figures 6.1 through 6.10 illustrate these comparisons for all strain gauge locations.

6.2.1. Strain gauge location 2L1 on the shaft

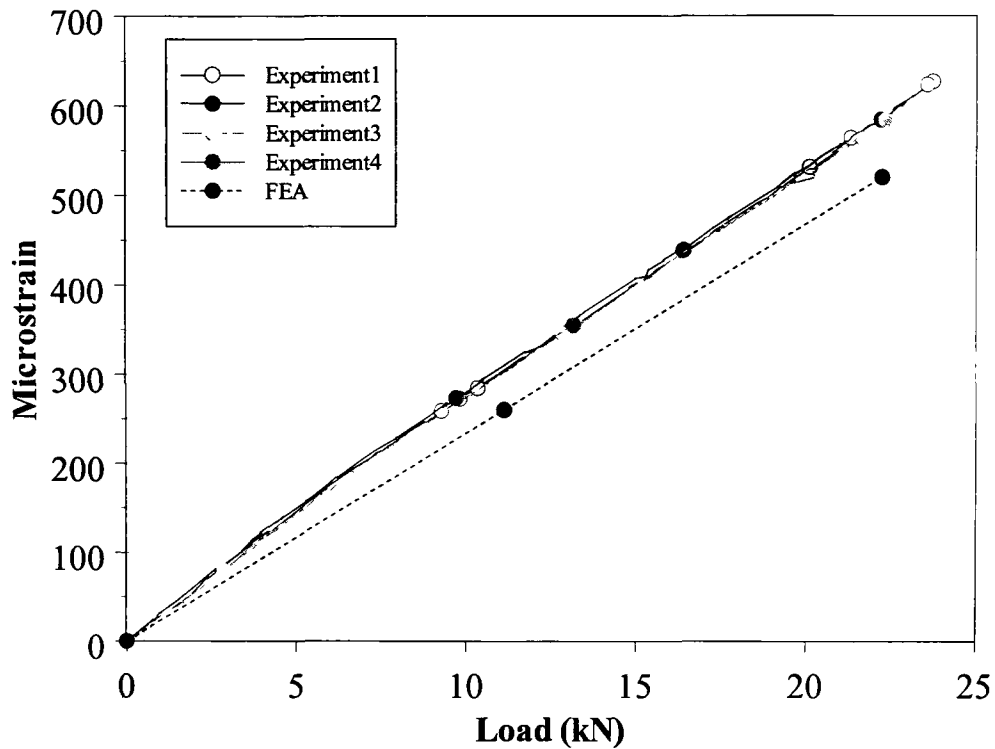


Figure 6.1. Strain versus load profile for shaft position 1 (2L1).

Strains measured from all four experiments were observed to compare very well and illustrated a linear profile which was expected. Findings of finite elements were consistent with experimental results up to 3 kN after which the results of FEA generally under predicted the experimental finding. The percentage of error was observed to gradually increase with loading and a maximum error of approximately 12% was found to occur at the peak loading of 22 kN.

6.2.2. Strain gauge location 2L2 on the shaft

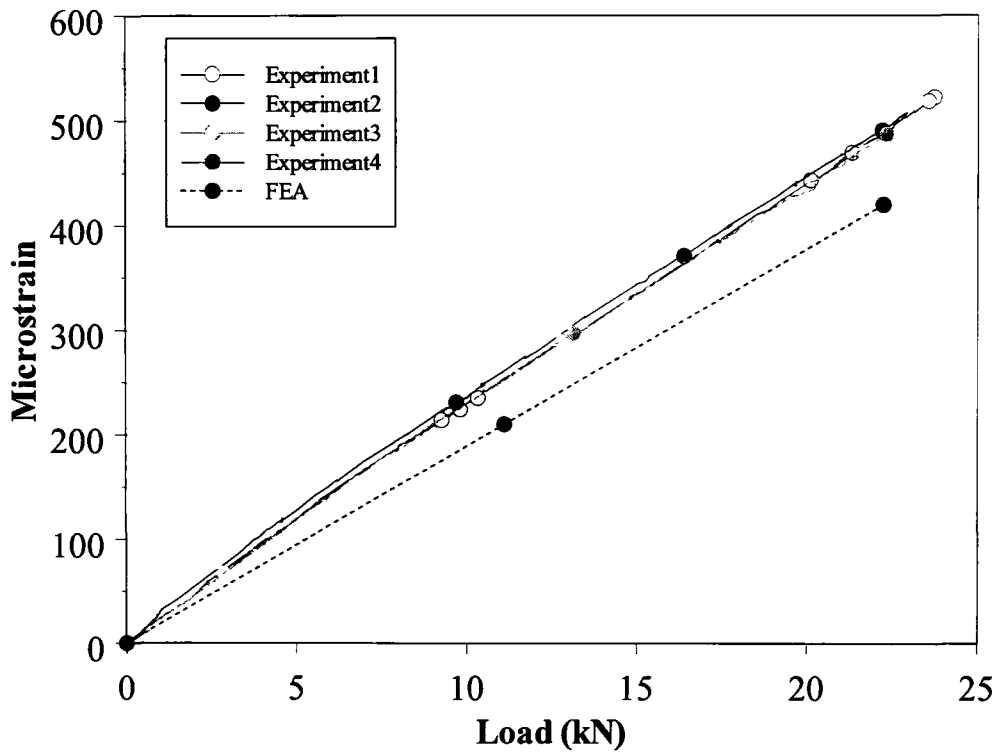


Figure 6.2. Strain versus load profile for shaft position 2 (2L2).

As observed with position 2L1, experimental findings of all four experiments were consistent. FEA's predictions were generally lower than the experiments with the percentage of error gradually increasing with loading. At peak loading, the variation between experimental results and FEA's predictions was maximum and was noted to be an approximate 15%.

6.2.3. Strain gauge location 1L1 on the mounting ring

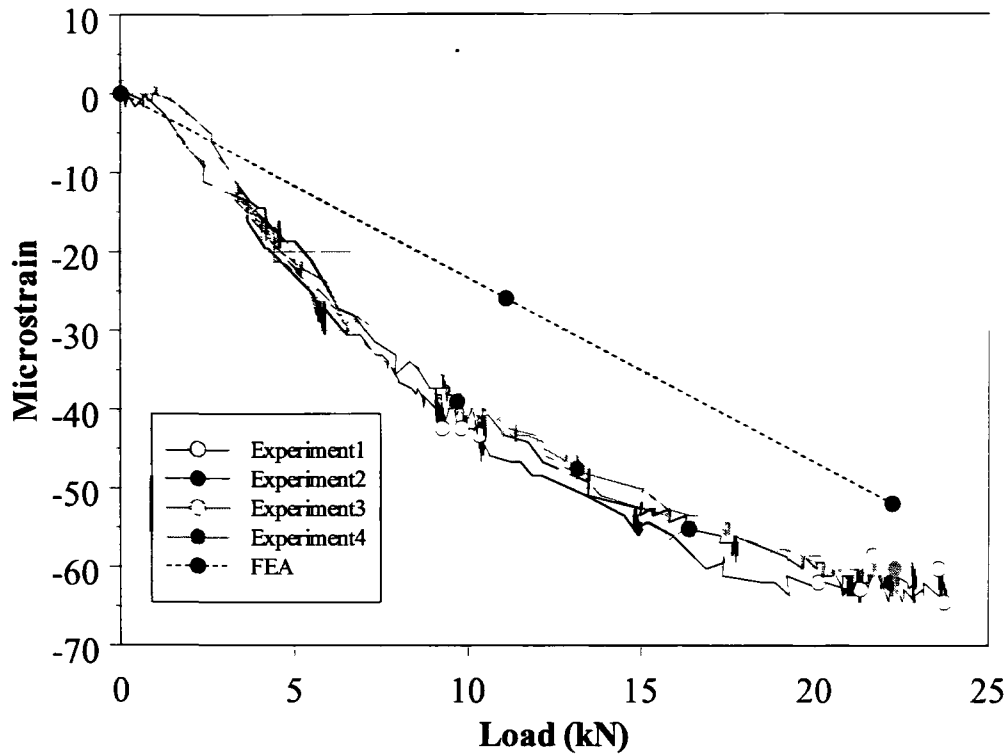


Figure 6.3. Strain versus load profile for mounting ring position 1 (1L1).

A good repeatability was observed from results of all the four experiments, in spite of the fact that, the results did not predict an exact linear response. Strain as measured from FEA lay within the experimental scatter up to approximately 3 kN, after which the results from FEA significantly vary from experimental observations. An error of approximately 15% was observed between experiments and FEA at the peak load.

6.2.4. Strain gauge location 1L2 on the mounting ring

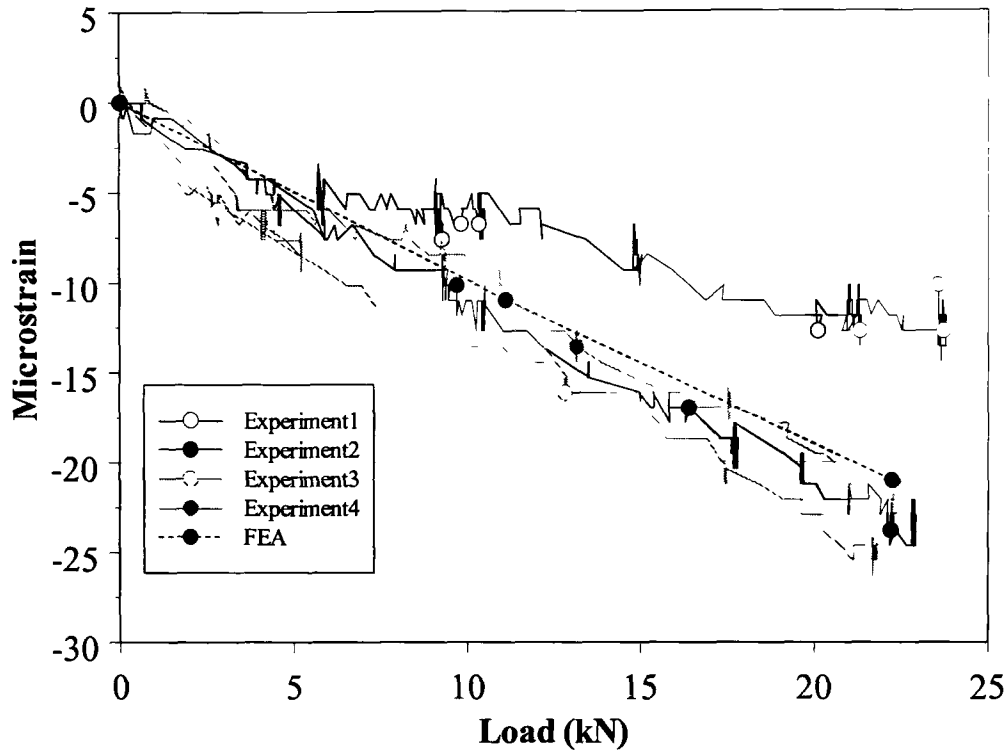


Figure 6.4. Strain versus load profile for mounting ring position 2 (1L2).

Strain results from the second, third, and fourth experiments had a good consistency, but first experiment had a significant variation from the other three, after approximately 5 kN of applied load. A considerable linearity in the results was observed in the second, third and fourth experiments. Results from FEA were within the range of experimental observations during the entire period of loading, with a minimum error in prediction of 2.5%.

6.2.5. Strain gauge location 1L3 on the mounting ring

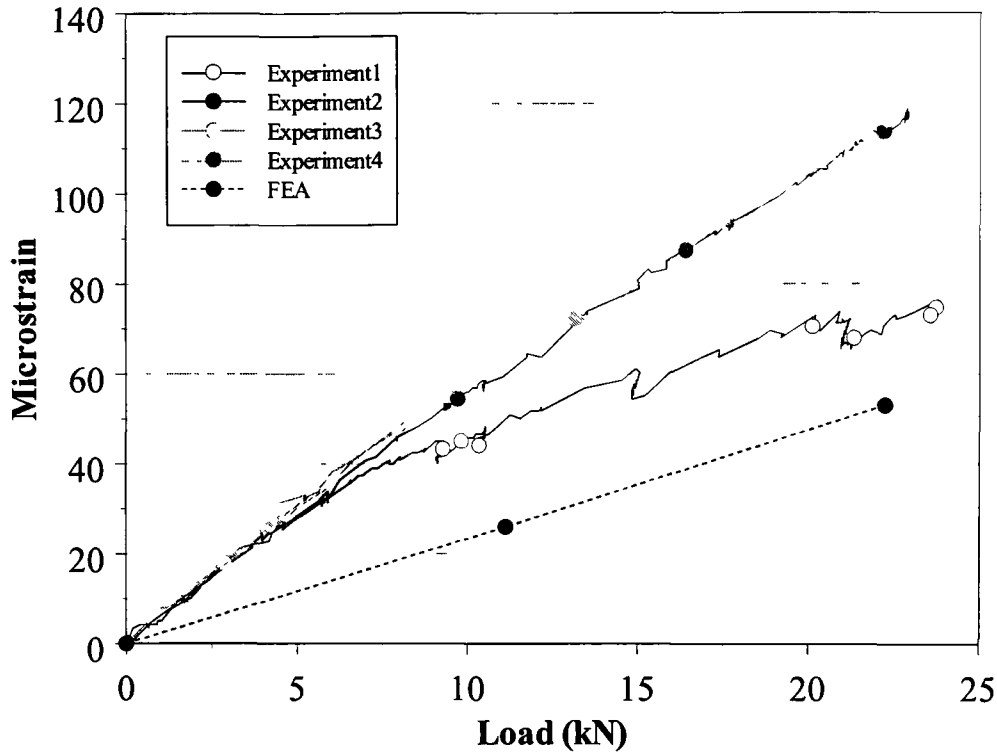


Figure 6.5. Strain versus load profile for mounting ring position 3 (1L3).

Similar to the results from position 1L2, a good consistency between experiments two, three, and four existed. After approximately 6 kN load, results of the first experiment significantly varied from the rest of the experiments. The strain values from FEA were generally under predicted as compared to the experimental values as discussed in most of the previous positions. The percentage of error between the experimental findings and numerical predictions was on the order of 50%.

6.2.6. Strain gauge location 1L4 on the removable flange

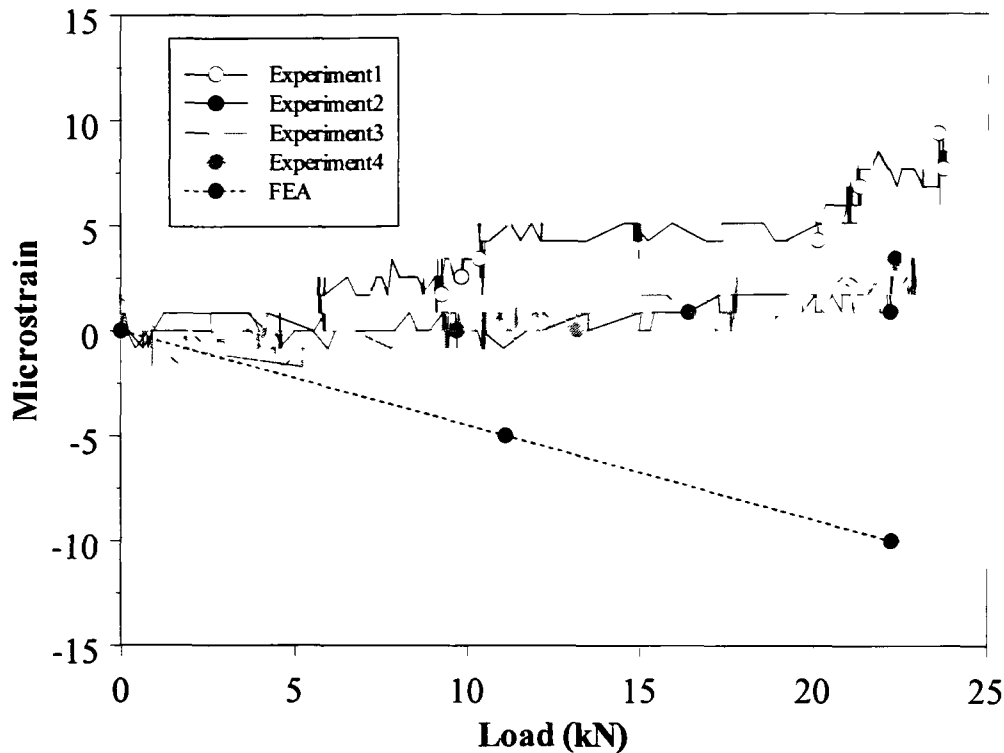


Figure 6.6. Strain versus load profile for flange position 1 (1L4).

Linearity in the results was not observed, but, strains measured from experimental tests two, three, and four compared very well. Strains observed from the first experiment were consistent with the other experiments up to a load of 6 kN. after which the results from experiment one significantly varied from the other tests. This could be attributed to the fact that, potential settling of the wheel might have occurred after the first experiment. Though linearity was observed in the predictions of FEA, the results of FEA were significantly under predicted in comparison to the experimental values. Strains observed from the experiments and FEA were opposite in nature and hence an error of close to 400% was noted.

6.2.7. Strain gauge location H5 on the removable flange

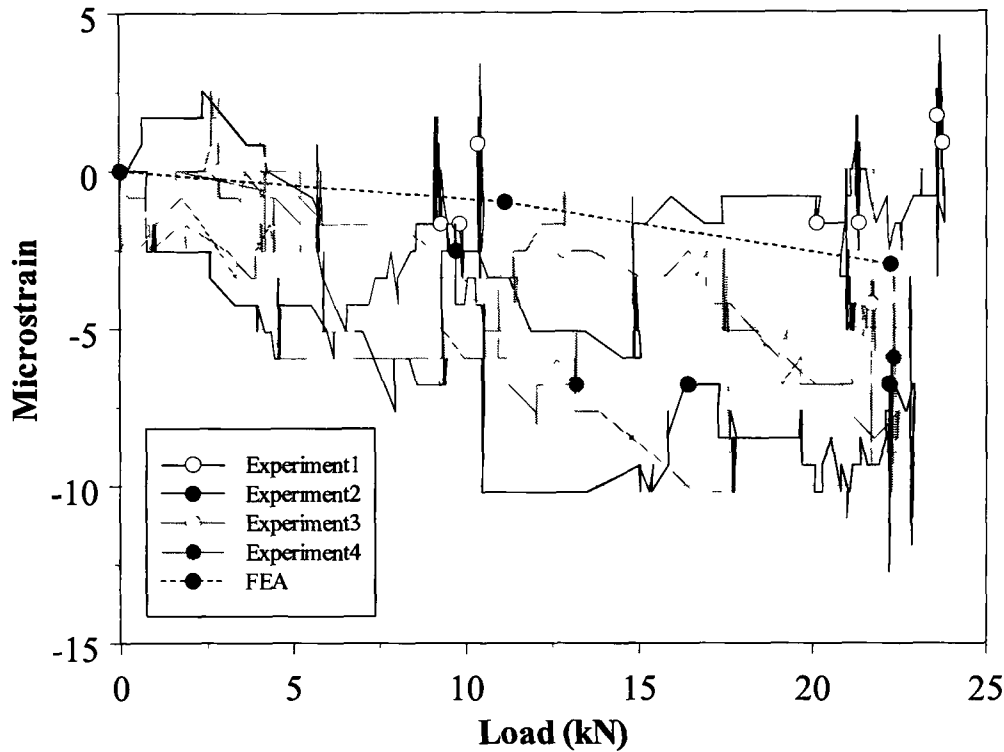


Figure 6.7. Strain versus load profile for flange position 2 (H5).

The strains measured in the strain gauge position both from experiments and FEA were low in magnitude. As a result these low strains, small variations in the measured values led to a significant increase in the percentage of error between experimental observations and numerical findings. Numerical predictions were found to be within the scatter of experimental findings. A percentage error of approximately 37% was observed. The reason behind the discontinuous nature (significant noise) of the curve is the low measured strains in the vicinity of the resolution of the measurement system.

6.2.8. Strain gauge location H6 on the removable flange

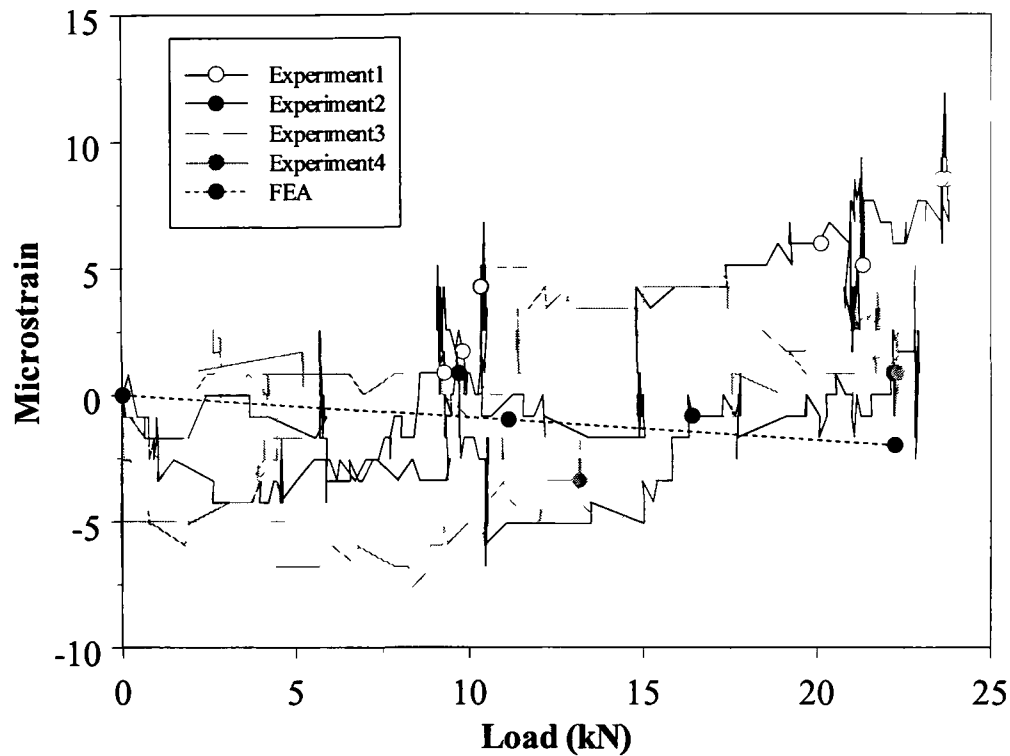


Figure 6.8. Strain versus load profile for flange position 3 (H6).

No consistency was observed in the results of all the four experiments. However predictions of FEA were within the experimental scatter. The strains measured by experiments were generally tensile in nature while FEA predictions were compressive. This difference resulted in a percentage error of 161.54%.

6.2.9. Strain gauge location H7 on the wheel base

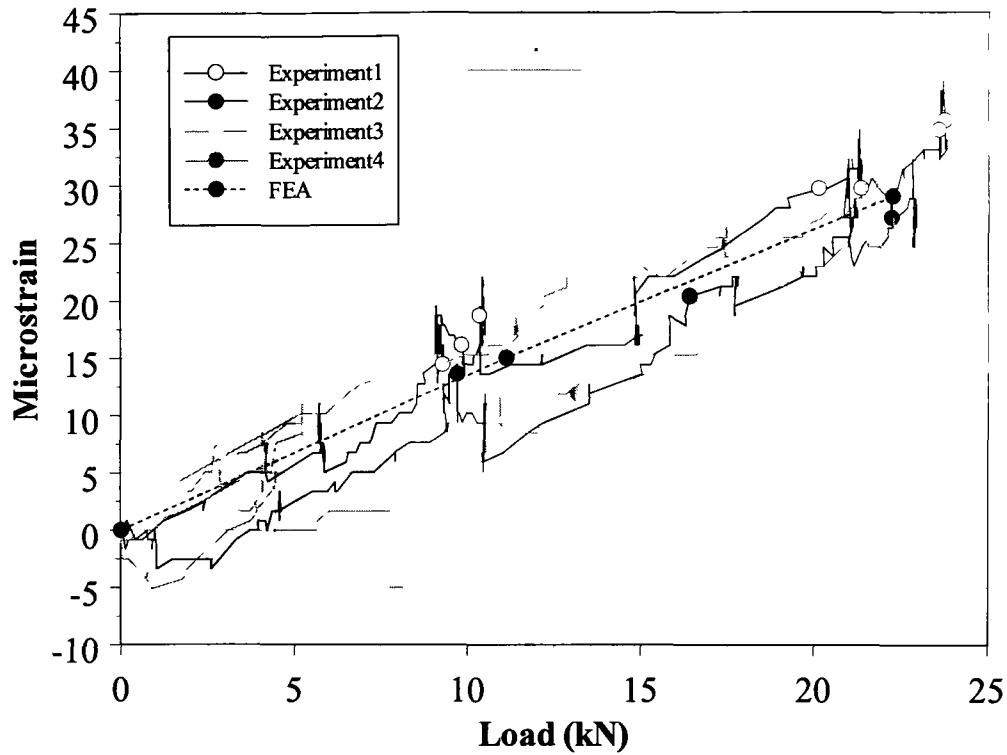


Figure 6.9. Strain versus load profile for wheel base position 1 (H7).

The results from experiments as well as FEA illustrate a considerable linear response in the strain versus load plot. Numerical findings were consistent with the experimental observations in this position with a negligible percentage error.

6.2.10. Strain gauge location H8 on the wheel base

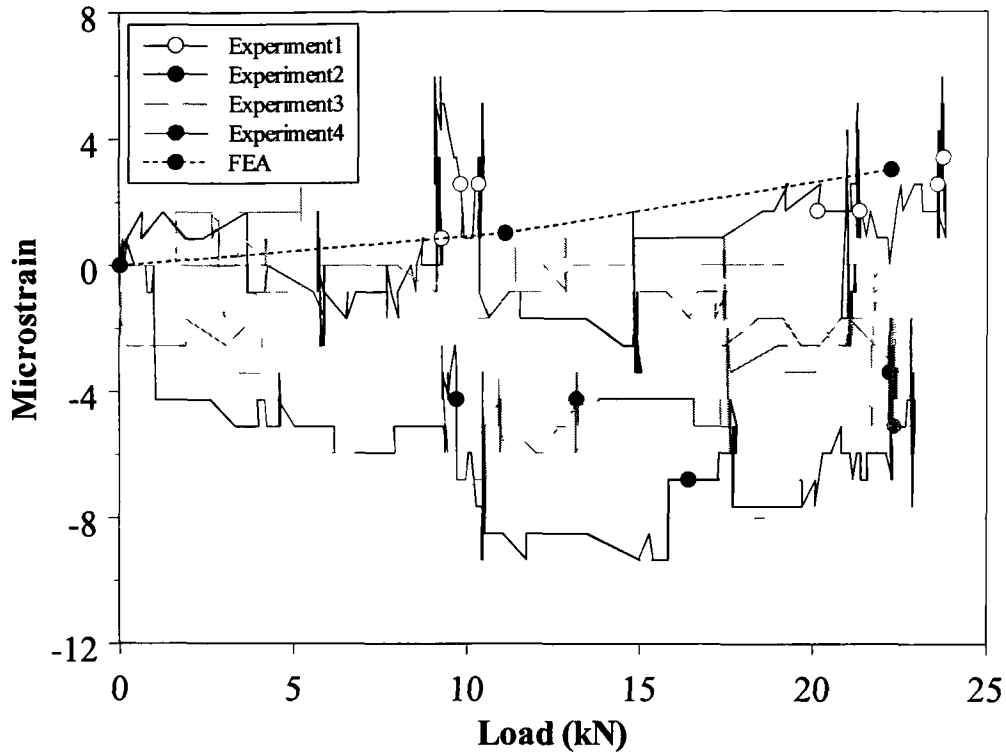


Figure 6.10. Strain versus load profile for wheel base position 2 (H8).

A significant variation existed between the results of the four experiments. Though predictions of FEA were somewhat inline with the results of the first experiment, it was not consistent with the other experiments. As with previous position H7, the average of maximum strain measured by experiments was 2 microstrain (compressive) whereas by FEA was 3 microstrain (tensile). This was the rationale behind a significant error of 250%.

For the majority of strain measurement locations, the percentage of error was less than 16%. In other locations, high percentages of error are attributed to the fact that strains were recorded to be in opposite sense (i.e., if experiments predicted tensile strain, FEA predicted compressive strain and vice versa) and were low in magnitude. The comparison of the experimental observations and numerical findings indicate that the developed finite element model of the wheel was able to predict with good level of accuracy, the deformation behaviour during the bending load application.

7. FINITE ELEMENT SIMULATION OF WHEEL CORNERING

FATIGUE TEST

7.1. Finite element model development for fatigue simulation

The development of a finite element model to perform fatigue simulations necessitated minor alterations to the previously validated wheel model. The auxiliary fixtures used in the simulation of the experiment were removed. Additionally to save further computational time, the shaft was replaced by a rigid beam with a Hughes-Liu element formulation, to which the rotary fatigue load was applied. The element formulation for the wheel components except the mounting ring was switched from a fully integrated selectively reduced solid element formulation to a constant stress solid element formulation. The mounting ring had only two elements through the thickness and this demanded the need of a fully integrated selectively reduced solid element formulation in order to effectively capture the bending stresses. Figure 7.1 illustrates the setup of the model used in fatigue analyses. Discretization of the model of wheel assembly was left unaltered from the experimental simulation. Hence the parameters representing the mesh quality were consistent with the values presented in section 5.2.1 of this thesis. The material model used here was consistent with the model used in the simulation of the experimental test.

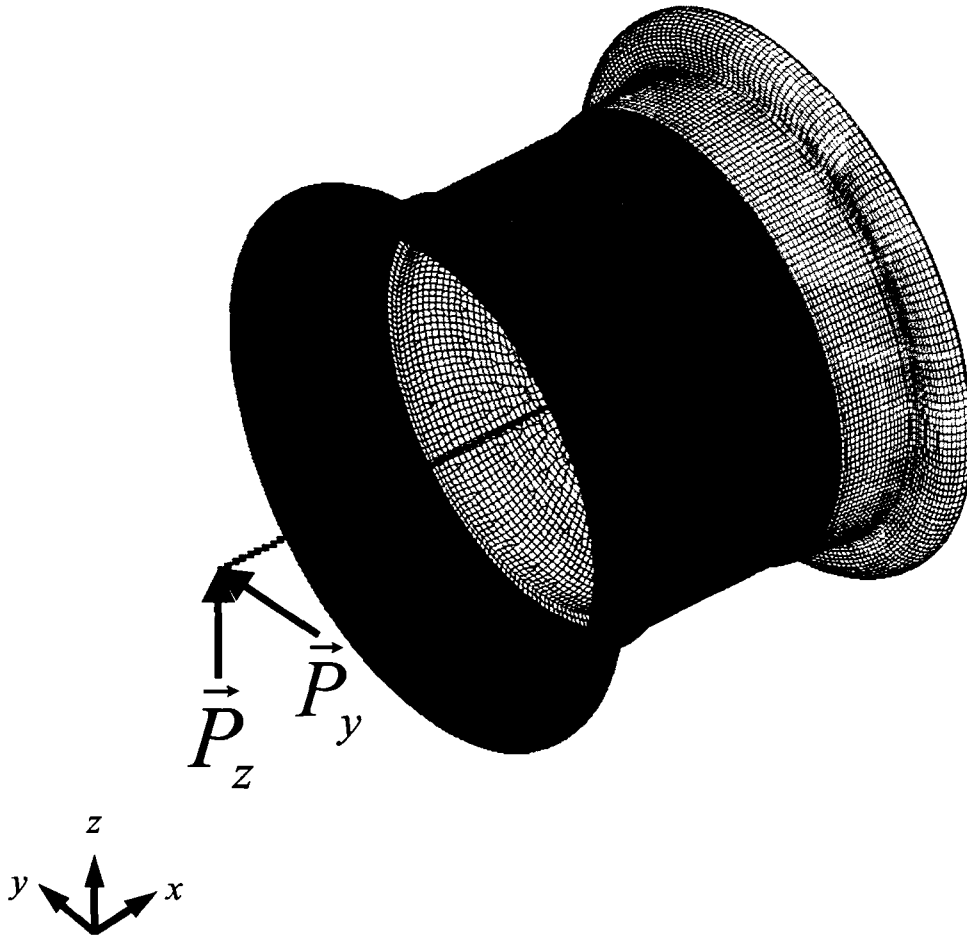


Figure 7.1. Finite element model for fatigue analyses.

7.1.1. Contact definition

An automatic surface to surface contact algorithm as previously used, was used to model the contact between various entities of the wheel assembly. The values for static and dynamic coefficients of friction were 0.35 and 0.25 which is consistent with the previous values. The value of unity for penalty scale factor was also left unaltered from the experimental simulations. A rigid nodal constraint was utilized to fasten the Hughes-Liu beam to the mounting ring of the wheel. This was done to simulate the effect of bolts holding the wheel onto the hub of the vehicle and to transmit the applied load (at the other tip of the beam) to the wheel. No excessive nodal penetrations between any contacting interfaces were observed to have occurred during the entire period of the simulation.

7.1.2. Application of boundary conditions

The outer most nodes of the flange furthest from the point of application of fatigue load were fully constrained. This was done to simulate the effect of flange being fully constrained as illustrated in Figure 2.8. The end of the rigid beam which had no applied load was constrained to the bolt holes of the mounting ring in order to effectively transmit the bending load. A dynamic rotating load was applied to the free end tip of the beam to generate a rotating bending moment on the mounting ring. This dynamic rotating bending moment was exerted on the wheel by applying two time varying perpendicular loads to the beam utilizing sine and cosine functions (represented by \vec{P}_y and \vec{P}_z) as illustrated in Figure 7.1. Mathematical representation of \vec{P} , \vec{P}_y and \vec{P}_z are denoted in equations 7.1 through 7.3.

$$\vec{P} = \vec{P}_y + \vec{P}_z \quad (7.1)$$

$$|\vec{P}_y| = |\vec{P}| \cdot \sin(\omega \cdot (t_i - t_{start})) \Rightarrow 22 \cdot \sin(62.8 \cdot (t_i - 0.035)) \cdot \text{kN} \quad (7.2)$$

$$|\vec{P}_z| = |\vec{P}| \cdot \cos(\omega \cdot (t_i - t_{start})) \Rightarrow 22 \cdot \cos(62.8 \cdot (t_i - 0.035)) \cdot \text{kN} \quad (7.3)$$

As discussed in chapter two, the load experienced by one of the rear axles, $|\vec{P}|$, was determined to be 22 kN. The angular velocity, ω , of the rotating fatigue load was specified as 62.8 rad/s consistent with the testing methodology of SAE J1992. Additionally, to simulate the effect of pressure exerted by the air inside the tire, the outer walls of the mining wheel assembly were subjected to a pressure of 827 kPa.

7.2. Simulation procedure

The fatigue simulation was solved explicitly based on the explicit time integration theory discussed in Appendix D. As the entire wheel was modeled with an isotropic elastic material, a particular position on the wheel at an identical point in the loading cycle was subjected to the same state of stress under the action of the applied rotating

bending moment after any given number of cycles. As a result, simulation to only one complete cycle was necessary to obtain the internal stress distribution within the wheel.

In order to preload the wheel assembly with appropriate bending loads, initially $|\bar{P}_z|$ was increased from 0 to 22 kN in the first 5 ms of the simulation. Further, this load was held constant until 35 ms of the simulation and during the entire duration from 0 to 35 ms, $|\bar{P}_y|$ was maintained at 0. After 35 ms, the load was gradually applied in the y direction also and this combination of $|\bar{P}_y|$ and $|\bar{P}_z|$ caused a bending load \bar{P} which began to rotate about the x -axis as represented by equation (7.1). Figure 7.2 illustrates the combination of the applied loads $|\bar{P}_y|$ and $|\bar{P}_z|$ to generate a total load of \bar{P}

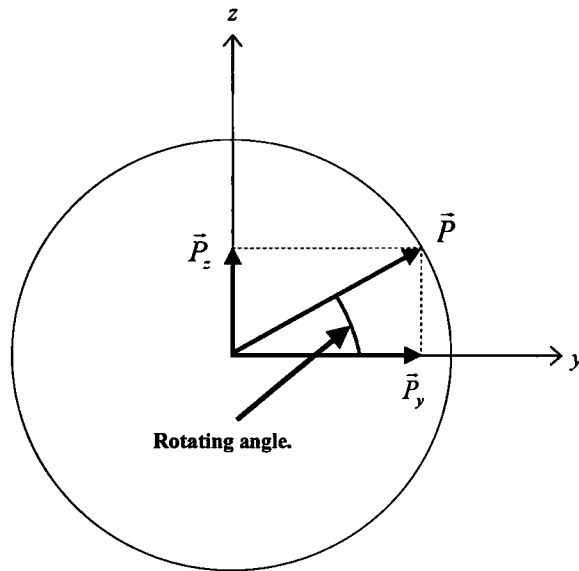


Figure 7.2. \bar{P} as an equivalent of \bar{P}_y and \bar{P}_z [42].

A technique called mass scaling was employed in the fatigue simulation to save computational time. The concept of mass scaling can be defined as adding mass, by increasing the density of the elements that do not satisfy Courant condition and there by increasing the timestep of the simulation. The timestep utilized in this integration scheme for the current problem was $0.675 \mu\text{s}$. Mass scaling can only be applied to quasi-static problems as the numerical predictions in these cases are not affected by the

inertial effects as in dynamic problems. The total mass of the wheel assembly was observed to be 214 kg and the mass added upon mass scaling was found to be no greater than 230 kg. Post processing of the results indicated that the problem was quasi-static as a result of the ratio between internal energy (strain energy) and the kinetic energy being over 2000 which justifies the application of mass scaling.

A personal computer with an AMD Opteron processor was utilized to complete the fatigue simulation. The internal clock speed of the processor was 2.19 GHz. The computer had 4 gigabytes of RAM and 250 gigabytes of hard disc space. The simulation was completed in approximately six and one half hours.

8. RESULTS AND DISCUSSIONS OF WHEEL CORNERING

FATIGUE TEST

8.1. Analysis of the results of wheel cornering fatigue test

Due to the axi-symmetric nature of the wheel model, stress fluctuations were observed only for 1/20th section of the wheel during the entire simulation period. The section chosen for analysis contained 5048 solid elements and is illustrated in Figure 8.1. The stress tensor for all these three dimensional elements was recorded at a rate of 4 kHz.

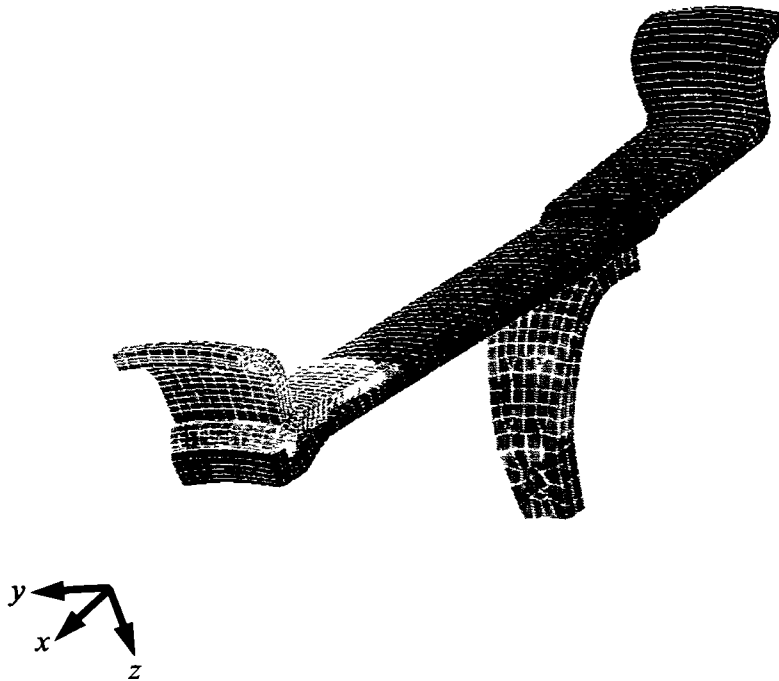


Figure 8.1. 1/20th section of the wheel with 5048 elements considered for fatigue analysis.

8.1.1. Development of fatigue analysis software

A fatigue analysis software was developed by the author along with his advisor. The software read the simulation output and calculated an element based fatigue factor of safety utilizing a number of fatigue failure theories. For every component in the stress tensor, the maximum and minimum were identified and the corresponding mean and alternating components were calculated based on equations (2.1) and (2.2). An effective

alternating and mean stress using von Mises and Sines approaches were calculated utilizing the equations (2.5) through (2.8). These effective alternating and mean stresses were applied to the modified Goodman theory of fatigue failure and fatigue factors of safety based on von Mises and Sines approaches were calculated for all the elements using equations (2.9) and (2.10). Additionally, an element based fatigue factor of safety applying a simplified damage mechanics approach (suggested by Lemaitre) as presented in equation (2.11) was calculated.

These theories of fatigue failure considered the material strength characteristics and the program required these to be specified by the user. The ultimate tensile strength of the wheel was specified as 365 MPa (consistent with material property of ASTM A40). The modified fatigue strength for the wheel assembly was specified as 129.78 MPa. Calculation of the modified fatigue factor assuming an infinite life of the wheel assembly was done assuming the following correction factors; the surface factor was specified as 0.83; the loading factor was assigned a value of 0.85; the remaining correction factors such as size factor, temperature factor, reliability factor and miscellaneous-effects factor were set to a value of unity. This fatigue analysis software outputs the finite element number, the corresponding mean and alternating stresses along with the factor of safety depending on the fatigue analysis approach selected by the user.

8.1.2. Results from the fatigue analysis software

The element based fatigue factor of safety for each of the 5048 elements was calculated utilizing the three different approaches. The four lowest fatigue factors of safety predicted by all the approaches are provided in Table 8.1. Additionally the four lowest fatigue factors of safety were calculated manually by applying a critical plane approach and are also provided in Table 8.1. The elements in each approach are arranged in increasing magnitudes of their factors of safety.

Table 8.1. Finite elements with lowest four fatigue factors of safety predicted by each approach.

<i>Element</i>	n_{vM}	<i>Element</i>	n_S	<i>Element</i>	n_{DM}	<i>Element</i>	n_{CP}
35887	1.914	111091	1.935	35885	1.157	111093	1.877
35885	1.944	111093	1.937	35889	1.174	111092	1.887
35889	1.957	111090	1.977	109291	1.259	111091	1.924
109291	1.995	111092	1.978	109289	1.324	111090	1.928

For each of the fatigue failure approaches, fatigue factors of safety for the other elements (which were predicted to have the four lowest fatigue factors of safety by other three approaches) are provided in Table 8.2 in ascending order of the element numbers. This was completed to give the reader an understanding of the difference in values of fatigue factors of safety for each element predicted by different approaches.

Table 8.2. Comparison of fatigue factors of safety predicted by different approaches.

<i>Element</i>	n_{vM}	n_S	n_{DM}	n_{CP}
35885	1.944	3.238	1.157	3.026
35887	1.914	2.881	1.374	3.522
35889	1.957	3.285	1.174	3.926
109289	2.465	4.015	1.324	4.994
109291	1.995	3.197	1.259	3.448
111090	3.190	1.977	1.494	1.928
111091	3.185	1.935	1.506	1.924
111092	3.111	1.978	1.505	1.887
111093	3.204	1.937	1.471	1.877

The positions of these elements on the model of the three-piece mining wheel are illustrated in Figures 8.2(a) through 8.2(c).

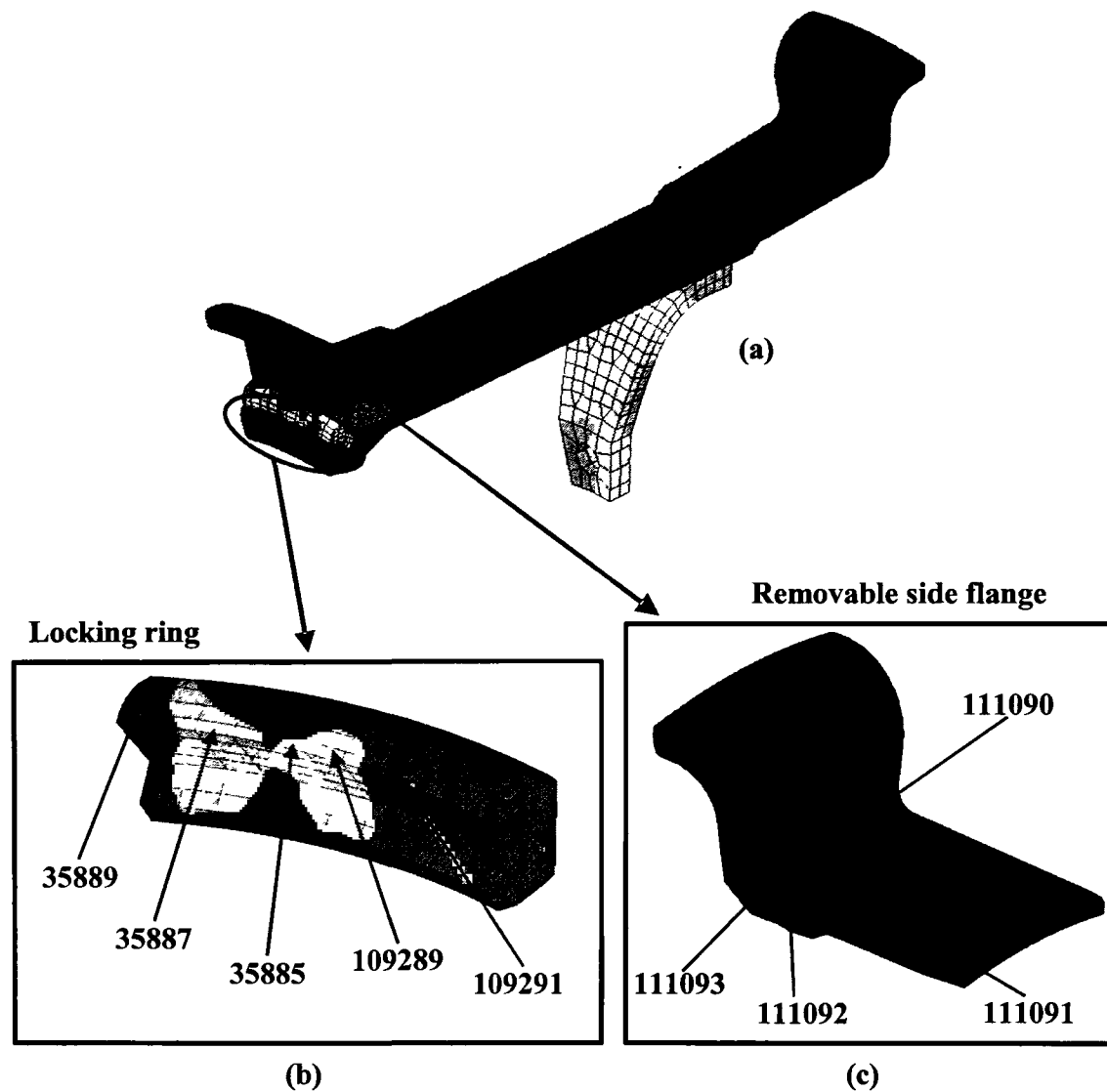


Figure 8.2. Elements with lowest four fatigue factors of safety predicted by each approach, (a) 1/20th of wheel considered for fatigue analysis, (b) & (c) magnified views of corresponding positions from (a).

8.1.3. Discussions

The fatigue factors of safety values predicted by the von Mises approach and damage mechanics approach were consistent. Similarly, predictions of the Sines approach was mostly inline with the predictions of the critical plane approach. The lowest fatigue factor of safety predicted by the von Mises (applied to the modified Goodman theory of failure), Sines (applied to the modified Goodman theory of failure), simplified damage mechanics (Lemaitre's approach), and critical plane (McDiarmid's)

approaches were determined to be 1.914, 1.934, 1.157, and 1.877 on the element numbers 35887, 111091, 35885, and 111093 respectively. These predictions indicated that an infinite life for the mining wheel should be expected as a result of the factors of safety values being greater than unity. The fatigue assessment utilizing a damage mechanics approach was considered to be the most conservative of all the four approaches. The elements with the lowest four factors of safety predicted by the von Mises and damage mechanics approaches were found to exist in the locking ring of the mining wheel assembly as illustrated in Figure 8.2(b). Additionally, as illustrated in Figure 8.2(c), elements with the lowest fatigue factors of safety calculated through the Sines and critical plane approaches were located in the removable side flange. The locations of these finite elements were in the vicinity of stress concentrations. Additionally, in the locking ring, the reason for the existence of elements with low factors of safety is attributed to the thin geometry of the locking ring and the significant contact stresses, it is subjected to.

The fatigue assessment in this investigation was completed on an undamaged wheel assembly. However in reality, the mining vehicles are often subjected to corrosive environments which will lead to degradation of the material. Additionally, during operation, any form of an impact to the wheel assembly can impart highly localized plastic strains. The effects of the environmental influence, any form of damage or misalignment imparted to the wheel during operation and wear of the wheel due to age were not implemented in the model. As a result, though this current study indicated an infinite life for the mining wheel assembly, it should be expected that the above mentioned effects will have a significant reduction in the estimated fatigue life of the wheel.

9. CONCLUSIONS

Upon completion of this research investigation dealing with the fatigue life assessment of multi-piece mining vehicle wheels, the following conclusions were made:

1. Upon complete review of the obtained literature, it was observed that the rationale behind majority of injuries and deaths in the mining industry related to servicing mining vehicle wheels is the negligence of operator or maintenance personnel to adhere to specific guidelines, rules, and requirements set out by health and safety organizations.
2. In spite of the fact that details regarding the specifics of the type of mining wheel involved in incidents were generally not available, from the limited cases where thorough documentation existed, it was established that the three-piece mining wheels were involved in the majority of incidents.
3. Experimental structural testing was completed on the three-piece mining wheel with an applied bending load of 22 kN, and within the regions measured by strain gauges, strains were observed to range from approximately 61 microstrain (compressive) to 100 microstrain (tensile) on the mining wheel. Within the wheel assembly, strains on the mounting ring were observed to be the greatest in magnitude in both compressive and tensile conditions. On the mounting ring, the largest tensile strain was observed to be 104.25 microstrain at location 1L3 and the largest compressive strain was observed to be 61.25 microstrain at location 1L1. Within the wheel base, position H7 indicated the largest tensile strain of 29 microstrain, and the other location of strain measurement. H8, illustrated a negligible strain. The removable flange illustrated minor strains with values ranging from 4.75 microstrain (compressive) at position H5 to 3.25 microstrain (tensile) at positions 1L4 and H6. For the auxiliary fixtures required in the bending load application, strains on the shaft were observed to be 592 microstrain (tensile) at position 2L1 and 494.75 microstrain (tensile) at position 2L2. The

results of the experimental testing were typically consistent through the four tests completed.

4. A numerical model of the wheel assembly utilized in the experimental testing was developed and simulated under similar loading conditions as in the experiment. A comparison of strains from the experimental and numerical methods revealed that the numerical model could predict the experimental observations in the majority of cases within 10% to 20% error with numerical methods generally under predicting the experimental observations. In cases where significant variation in the experimental and numerical findings for the maximum strain was observed, it was noted that these regions experienced a very small degree of strain and thus slight variations from experimental observations resulted in significant percentage error. Although the minority of strain measurement locations illustrated higher percentage error for the maximum strain value, it was observed that the numerical simulation predictions for strain, when compared as a function of the applied bending load, were generally within the scatter of experimental observations. Based on this validation, it was concluded that the numerical model could predict the structural response of the mining wheel very well.

5. A numerical simulation of fatigue loading incorporating SAE J1992 standard was completed on the validated numerical model of the wheel. Utilizing the results of the fatigue simulation, fatigue factors of safety for each finite element was estimated based on four different approaches namely the von Mises (applied to the modified Goodman theory), the Sines approach (applied to the modified Goodman theory), the simplified Lemaitre's approach, and the critical plane approach. The least fatigue factors of safety predicted by the approaches were 1.914, 1.934, 1.157, and 1.877 respectively, indicating that an infinite life of the mining wheel should be expected. It was noted that lower values of the factor of safety was observed for the locking ring when applying the von Mises and simplified Lemaitre's fatigue methods. Potential damage and / or misalignment to the locking ring will further reduce this factor of safety.

REFERENCES

1. The Mining Association of Canada, 'Facts and figures 2007', accessed August 27th, 2008,
<http://www.mining.ca/www/media_lib/MAC_Documents/Publications/2007_Facts_Figures/Facts_Figures_2007_E.pdf>.
2. The Mining Association of Canada, 'Aboriginal economic development and the Canadian mining industry', accessed August 27th, 2008,
<http://www.mining.ca/www/Public_Policy_Issues/Documents/Aboriginal_Economic.php>.
3. The Mining Association of Canada, 'Revenues to Governments from the Canadian Mining Industry 2002-2006', accessed August 27th, 2008,
<http://www.mining.ca/www/media_lib/MAC_Documents/Publications/English/08_05_14_EntransRpt.pdf>.
4. Gibson G., Klinck J., 'Canada's resilient north: The impact of mining on aboriginal communities', *Pimatisiwin: A journal of aboriginal and indigenous community health* 3(1), 26 pages.
5. WorkSafe BC, 'Occupational Injuries by Accident Type and Occupation in British Columbia, 1997-2006', accessed January 10th, 2008,
<http://www.worksafebc.com/publications/reports/statistics_reports/default.asp>.
6. Workers Compensation Board of Manitoba, 'Manitoba Workplace Injury And Illness Statistics Report for 2001-2004', accessed January 10th, 2008,
<http://www.wcb.mb.ca/download/current_publications/InjuryStatReport04.pdf>.

7. Saskatchewan Workers' Compensation Board, 'Statistical Supplement 1999',
accessed on January 10th 2008,
<http://www.wcsask.com/WCBPortal/ShowProperty/WCBRepository/pdfs/1999_StatSupplement>
8. Saskatchewan Workers' Compensation Board, 'Statistical Supplement 2000',
accessed on January 10th 2008,
<http://www.wcsask.com/WCBPortal/ShowProperty/WCBRepository/pdfs/2000_StatSupplement>.
9. Saskatchewan Workers' Compensation Board, 'Statistical Supplement 2001',
accessed on January 10th 2008,
<http://www.wcsask.com/WCBPortal/ShowProperty/WCBRepository/pdfs/2001_StatSupplement>.
10. Saskatchewan Workers' Compensation Board, 'Statistical Supplement 2002',
accessed on January 10th 2008,
<http://www.wcsask.com/WCBPortal/ShowProperty/WCBRepository/pdfs/2002_StatSupplement>.
11. Saskatchewan Workers' Compensation Board, 'Statistical Supplement 2003',
accessed on January 10th 2008,
<http://www.wcsask.com/WCBPortal/ShowProperty/WCBRepository/pdfs/2003_StatSupplement>.
12. Saskatchewan Workers' Compensation Board, 'Statistical Supplement 2004',
accessed on January 10th 2008,
<http://www.wcsask.com/WCBPortal/ShowProperty/WCBRepository/pdfs/2004_StatSupplement>.

13. Saskatchewan Workers' Compensation Board, 'Statistical Supplement 2005',
accessed on January 10th 2008,
<http://www.wcsask.com/WCBPortal/ShowProperty/WCBRepository/pdfs/2005_StatSupplement>.
14. Saskatchewan Workers' Compensation Board, 'Statistical Supplement 2006',
accessed on January 10th 2008,
<http://www.wcsask.com/WCBPortal/ShowProperty/WCBRepository/pdfs/2006_StatSupplement>.
15. Workplace Safety & Insurance Board, Ontario, 'Young Worker Statistics 2004',
accessed on January 11th 2008,
<[http://www.wsib.on.ca/wsib/wsibsite.nsf/LookupFiles/DownloadableFileYoungWorkerStats/\\$File/YoungWorkerStats.pdf](http://www.wsib.on.ca/wsib/wsibsite.nsf/LookupFiles/DownloadableFileYoungWorkerStats/$File/YoungWorkerStats.pdf)>.
16. Workplace Safety & Insurance Board, Ontario, 'Young Worker Statistics 2005',
accessed on January 11th 2008,
<[http://www.wsib.on.ca/wsib/wsibsite.nsf/LookupFiles/DownloadableFileYoungWorkerStats/\\$File/YoungWorkerStats.pdf](http://www.wsib.on.ca/wsib/wsibsite.nsf/LookupFiles/DownloadableFileYoungWorkerStats/$File/YoungWorkerStats.pdf)>.
17. Workplace Safety & Insurance Board, Ontario, 'Young Worker Statistics 2006',
accessed on January 11th 2008,
<[http://www.wsib.on.ca/wsib/wsibobj.nsf/LookupFiles/DownloadableFile2006YoungWorkerStats/\\$File/YoungWorkerStats2006.pdf](http://www.wsib.on.ca/wsib/wsibobj.nsf/LookupFiles/DownloadableFile2006YoungWorkerStats/$File/YoungWorkerStats2006.pdf)>.
18. Employment and Immigration, Alberta, 'A Report on Workplace Fatalities in Alberta, 1991-2004', accessed on January 12th 2008,
<http://employment.alberta.ca/documents/WHS/WHS-PUB_fatal_1991_2004.pdf>.

19. Employment and Immigration, Alberta, 'Workplace Incident Fatalities Accepted by the Workers Compensation Board in 2004', accessed on January 12th 2008, <http://employment.alberta.ca/documents/WHS/WHS-PUB_wpfatal_wcb_2004.pdf>.
20. Employment and Immigration, Alberta, 'Workplace Incident Fatalities Accepted by the Workers Compensation Board in 2005', accessed on January 12th 2008, <http://employment.alberta.ca/documents/WHS/WHS-PUB_wpfatal_wcb_2005.pdf>.
21. Employment and Immigration, Alberta, 'Workplace Incident Fatalities Accepted by the Workers Compensation Board in 2006', accessed on January 12th 2008, <http://employment.alberta.ca/documents/WHS/WHS-PUB_wpfatal_wcb_2006.pdf>.
22. Employment and Immigration, Alberta, 'Workplace Incident Fatalities Accepted by the Workers Compensation Board in 2005', accessed on January 12th 2007, <http://employment.alberta.ca/documents/WHS/WHS-PUB_wpfatal_wcb_2007.pdf>.
23. WORK SAFE ALBERTA, 2004, 'Workplace Health and Safety Bulletin - Servicing Tires Safely', Alberta Human Resources and Employment, Canada, GS003 – General Safety, 7 pages.
24. SAFEWORK, 2003, 'Servicing Tires and Wheels', SAFEWORK, Manitoba, Canada, Bulletin No. 228, 2 pages.
25. WorkSafe, 2004, 'Truck Tire Explosions claim two more lives', Saskatchewan Labour Occupational Health and Safety, Saskatchewan, Canada, 1 page.

26. Fatality Assessment and Control Evaluation, 2006, 'An apprentice mechanic died when the truck tire he was standing over exploded', California FACE, California, USA, FACE 05CA007, *7 pages*.
27. Fatality Assessment and Control Evaluation, 1996, 'Truck rental service laborer dies when struck by lock ring from exploded truck tire', Indiana FACE, Indiana, USA, FACE 96IN07101, *2 pages*.
28. WorkSafe, 1997, 'Split Ring Wheel Fatality', Department of Consumer and Employment Protection, Government of Western Australia, Toodyay, Australia, *2 pages*.
29. Fatality Assessment and Control Evaluation, 2003, 'Worker struck by side ring of multi-piece rim during wheel installation', Alaska FACE, Alaska, USA, FACE 03AK006, *13 pages*.
30. OSH, 2001, 'Worker Struck by Tire Rim', Alberta Workplace Health and Safety, Alberta, Canada, F 263477, *17 pages*.
31. Fatality Assessment and Control Evaluation, 1992, 'Owner of heavy equipment maintenance business dies after being struck by an exploding split rim of a test roller tire', Minnesota FACE, Minnesota, USA, FACE MN9208, *3 pages*.
32. Fatality Assessment and Control Evaluation, 2004, 'Laborer killed while inflating a tire mounted on a multi-piece rim wheel', Massachusetts FACE, Massachusetts, USA, FACE 03-MA-057-01, *7 pages*.
33. Mines and Aggregates Safety & Health Association, 2000, 'Take TEN for Safety', MASHA, Ontario, Canada, *5 pages*.

34. Barrick, 2007, 'Reko Diq Tyre Fatality', Flash Report, Patangaz, Pakistan, 2 *pages*.
35. Regan R., 2004, 'Queensland fatality during wheel removal', Safety Alert, Mineral Resources, New South Wales, Queensland, Australia, Report No: SA 0401, 4 *pages*.
36. Barrick, 2007, 'Kanowna Tyre Explosion', Flash Report, Kanowna Belle, Australia, 2 *pages*.
37. Porcupine / North-eastern Ontario Mines Safety Group, 2007, 'Surface Wheel Accident', Safety Bulletin, North-eastern Ontario, Canada, 1 *page*.
38. Willoughby M., 2005, 'Queensland fatality – road train rim assembly Failure', NSW Department of Primary Industries, Queensland, Australia, Mine Safety Report No: SA 14, 3 *pages*.
39. OSH, 2004, 'Tyre Fitter killed by Exploding Tyre', Occupational Safety & Health Services, Department of Labour, New Zealand, 1 *page*.
40. Wong B., Dwayne Barrett, 1998, 'Worker Struck by Truck Wheel', Alberta Labor Workplace Health and Safety, Alberta, Canada, F 328907, 23 *pages*.
41. Simpson A., 2001, 'Tractor Tyre Explosion', WorkSafe Operations, Western Australia, Australia, 2 *pages*.
42. Shigley J., Mischke C., and Budynas R., 2004, 'Mechanical Engineering Design', 7th Edition, McGraw-hill, New York, *pages 344-349*.
43. Sines G. and Waisman J., 1959, 'Behavior of metals under complex static and alternating stresses', edition G. Sines in Metal Fatigue, McGraw-Hill, New York.

44. Shigley J. E. and Mitchell L. D., 1983, 'Mechanical Engineering Design', 4th edition, McGraw-Hill, New York, *page 333*.
45. Collins J. A., 1993, 'Failure of Materials in Mechanical Design', 2nd edition, J. Wiley & Sons, New York, *pages 238-254*.
46. Sines G., 1955, 'Failure of Materials under Combined Repeated Stresses, Superimposed with Static Stresses', Technical Note 3495, NACA.
47. Smith J. O., 1942, 'The effect of Range of Stress on the Fatigue Strength of Metals', Univ. of Ill., Eng. Exp. Sta. Bull., (334).
48. Lemaitre J., 1992, 'A Course on Damage Mechanics', Springer, *pages 276-282*.
49. McDiarmid D. L., 1991, 'A general criterion for high cycle multiaxial fatigue failure', *Fatigue Fract. Engng Mater. Struct. Vol. 14, No. 4, pages 429-453*.
50. McDiarmid D. L., 1994, 'A shear stress based critical-plane criterion of multiaxial fatigue failure for design and life prediction', *Fatigue Fract. Engng Mater. Struct. Vol. 17, No. 12, pages 1475-1484*.
51. Society of Automotive Engineers, 1993, 'Wheel Cornering Fatigue Test Standard SAE J1992 Nov93', SAE Handbook, 2000, 400 Commonwealth Drive, Warrendale, PA.
52. Shang S., 2006, 'Finite Element Modeling of Dynamic Impact and Cornering Fatigue of Cast Aluminium and Forged Magnesium Road Wheels', A Dissertation for requirements of the Degree of Doctorate of Philosophy in Mechanical Engineering at the University of Windsor.

53. GOM mbH, 'ARAMIS User Manual v5.4.1', Mittelweg 7-8, D-38106 Braunschweig, Germany.
54. Matweb – Material Property Data, 'Steel ASTM A40, Grade 40 Hot Rolled Carbon Steel, Structural Quality, Mechanical Properties', accessed on November 11th 2007,
<<http://www.matweb.com/search/DataSheet.aspx?MatGUID=adac6f5ff5fa4652a3532dbc819cf121&ckck=1>>
55. Bathe K. J., 1990, 'Finite Element Procedures in Engineering Analysis', Prentice Hall of India Private Limited, New Delhi, *pages 501-512*.

APPENDIX A

A.1. Design of the shaft

The bending load application problem was approximated as a cantilever beam problem with a concentrated load at its free tip (similar to the shaft in the experimentation). Based on this approximation, a cantilever beam having a span of 0.7 m with a point load of 22 kN was utilized and the corresponding shear force and bending moment diagrams are presented in Figure A.1.

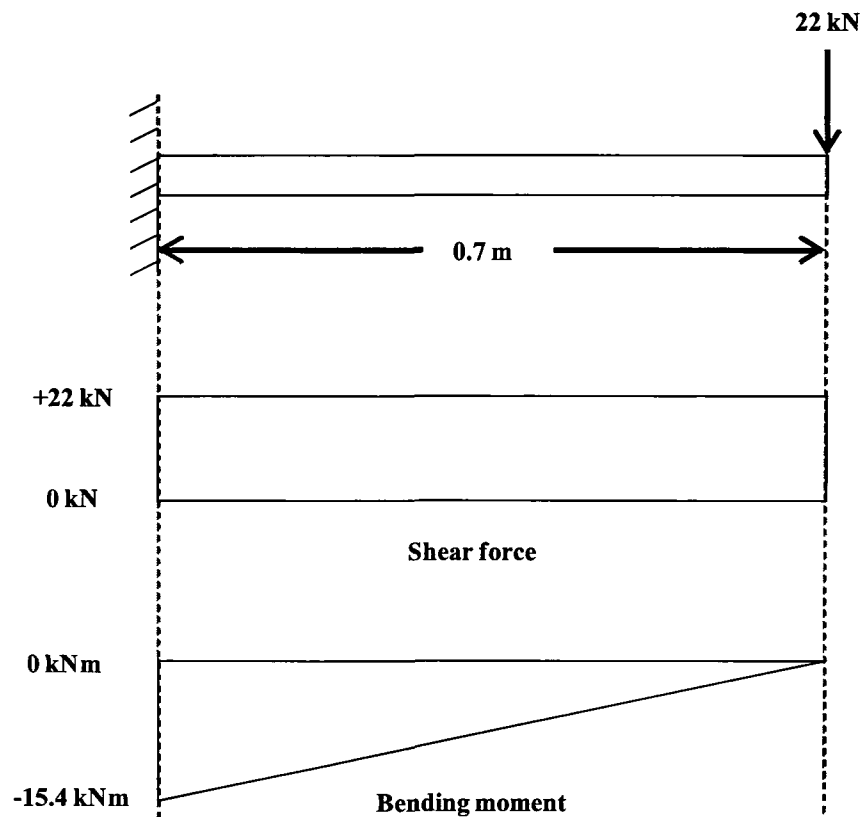


Figure A.1. Shear force and bending moment diagrams.

The length of the shaft was obtained as 700 mm from the SAE J1992 protocol. The diameter of the shaft was assumed to be 100 mm to perform the design calculations.

The maximum normal stress on the shaft is estimated utilizing the formula;

$$\sigma = \frac{M \cdot y}{I}$$

where, σ is the maximum normal stress on the shaft, M is the maximum bending moment (15.4 kNm) obtained from the bending moment diagram, y equals half times the diameter for a solid circular shaft, and I is equal to $(\pi d^4/64)$.

Upon substituting the values for M , y , and I , as -15400 Nm, 0.05 m, and $5E^{-06} \text{ m}^4$ respectively, the value of σ was obtained as -154 MPa.

For a solid circular shaft subjected to bending, maximum shear stress is given by;

$$\tau = \frac{4 \cdot V}{3 \cdot A}$$

where, τ is the maximum shear stress, V is the maximum shear force on the shaft, and A is the cross-sectional area of the shaft. The values of V and A were substituted as 22 kN and $7.85E^{-03} \text{ m}^2$ respectively to obtain the value of maximum shear stress. The calculated value of τ was 11.21 MPa.

The formula to obtain the principal stresses is;

$$\sigma_1, \sigma_2 = \frac{\sigma_x + \sigma_y}{2} \pm \sqrt{\left(\frac{\sigma_x - \sigma_y}{2}\right)^2 + \tau_{xy}^2}$$

Upon substituting the values for σ_x , σ_y , and τ_{xy} as -154 MPa, 0 MPa, and 11.21 MPa, respectively, the values of principal stresses obtained were -154.81 MPa and 0.81 MPa. The principal stresses are lower than the yield strength (220 MPa) of the material and hence the design of the shaft is considered safe.

A.2. Design of the adapter plate

The shaft had a diameter of 100 mm. The adapter plate was to be attached to the mounting ring utilizing the bolt holes on the mounting ring. Hence, the diameter of the adapter plate was assumed to be 350 mm which is slightly larger than the bolt circle diameter of the mounting ring. The adapter plate had a thickness of 120 mm. These assumptions were made based on the safe design of the shaft (i.e. 350 mm diameter is significantly larger than 100 mm diameter and hence the adapter plate would transfer the load without failure).

A numerical model of the adapter plate with the above assumptions was developed and utilized in the simulation of the experimental testing. The predictions of the simulations illustrated that the maximum stress experienced by the adapter plate was 58.71 MPa which is lesser than the yield strength of the material proving the design safe.

A.3. Design of the wheel supporting fixtures

The wheel supporting fixture had a cross-sectional area of approximately $(68 \times 210) \text{ mm}^2$ on the curved surface of the fixture. These areas were in contact with the flanges of the wheel. From the numerical predictions, it was observed, that there were significant contact stresses associated with the fixtures. However, the maximum stress experienced by the fixture at the bottom flange (in simulations) which was closer to the point of load application (expected to experience the maximum among all three fixtures) was 111.50 MPa. As a result of this stress being lower than the yield strength of the material, the design was considered safe.

APPENDIX B

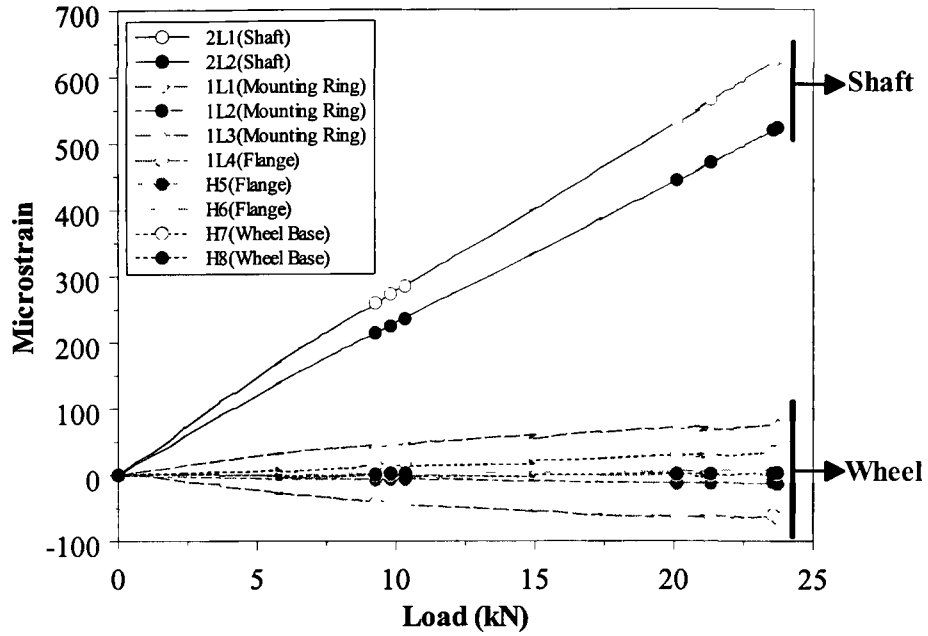


Figure B.1(a). Strain versus load profiles for all ten strain gauge positions from the first experiment.

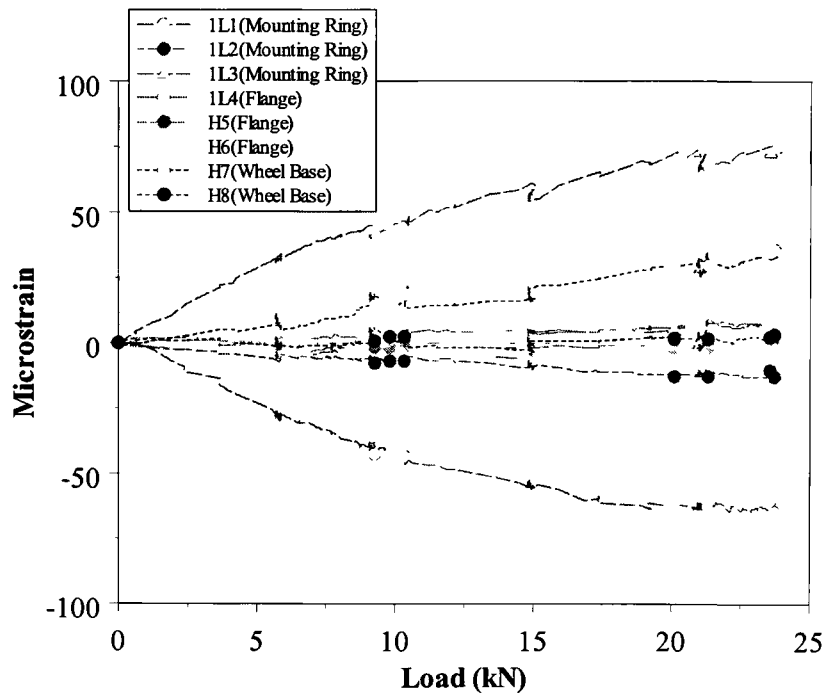


Figure B.1(b). Strain versus load profiles for strain gauge positions (wheel assembly) from the first experiment.

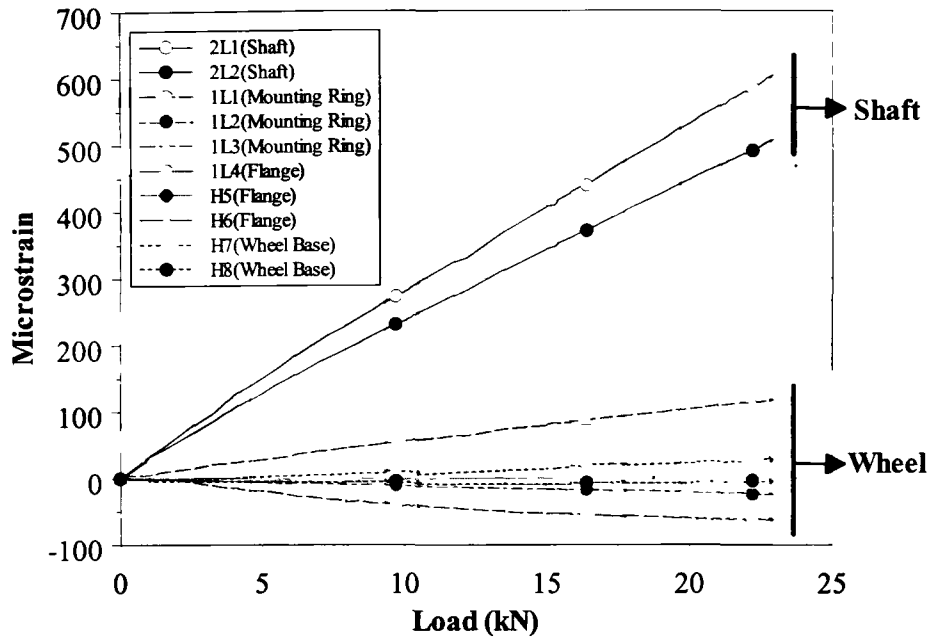


Figure B.2(a). Strain versus load profiles for all ten strain gauge positions from the second experiment.

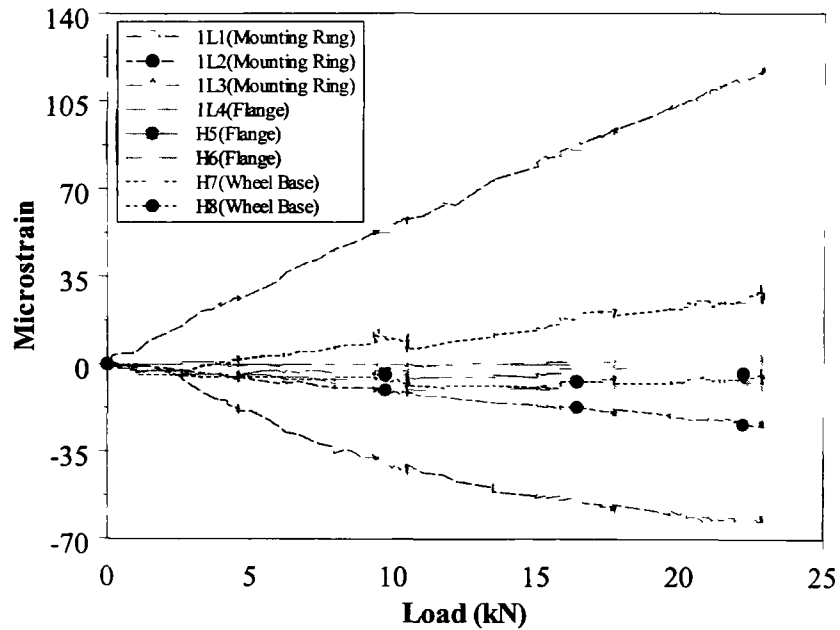


Figure B.2(b). Strain versus load profiles for strain gauge positions (wheel assembly) from the second experiment.

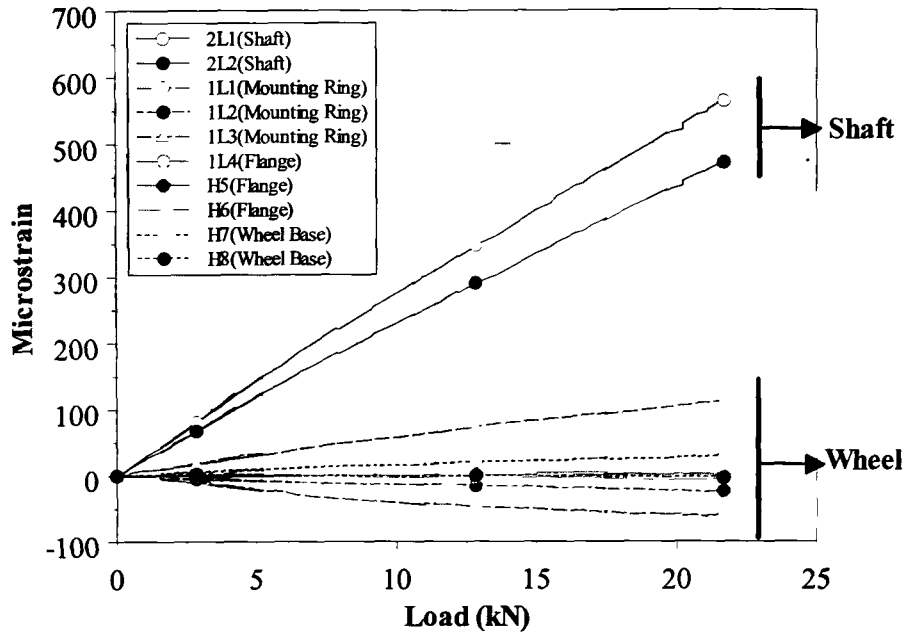


Figure B.3(a). Strain versus load profiles for all ten strain gauge positions from the third experiment.

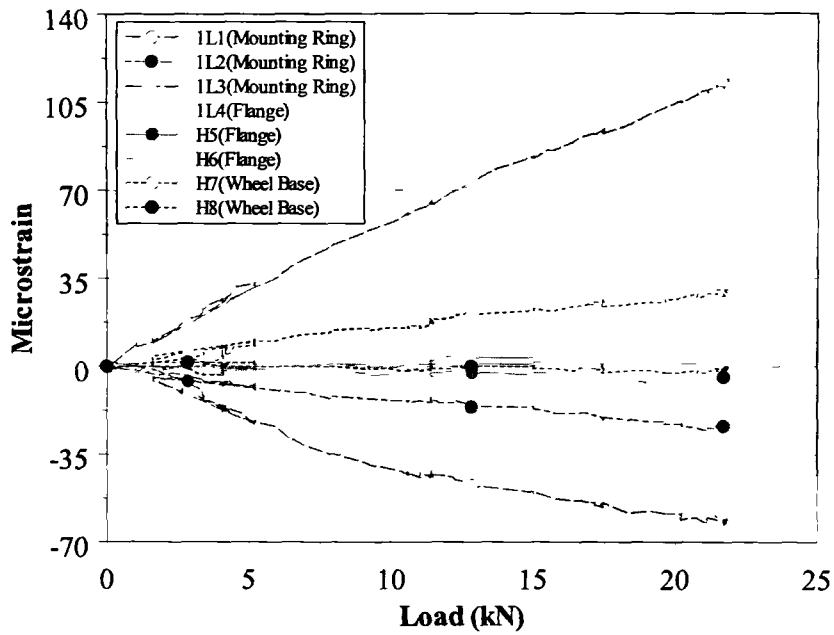


Figure B.3(b). Strain versus load profiles for strain gauge positions (wheel assembly) from the third experiment.

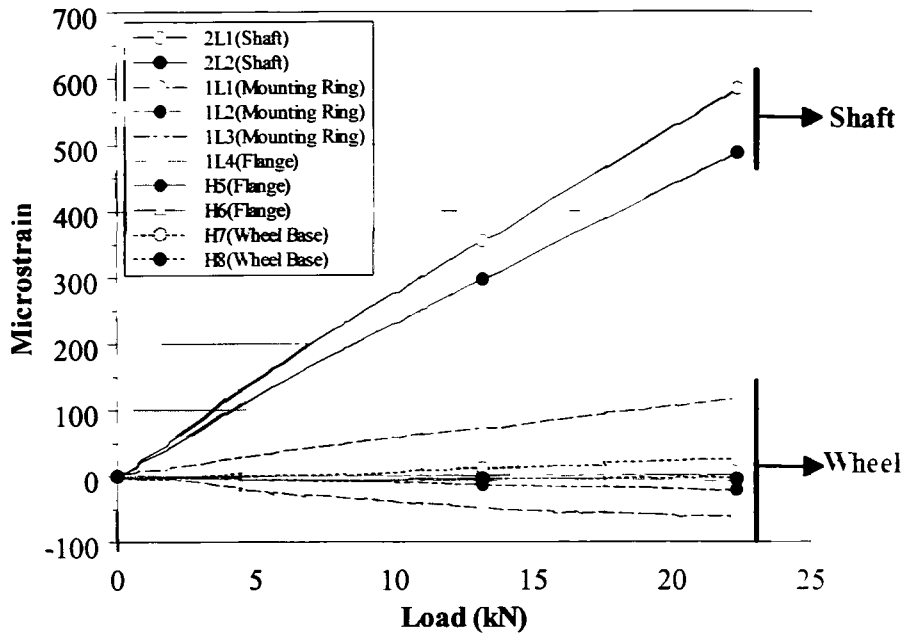


Figure B.4(a). Strain versus load profiles for all ten strain gauge positions from the fourth experiment.

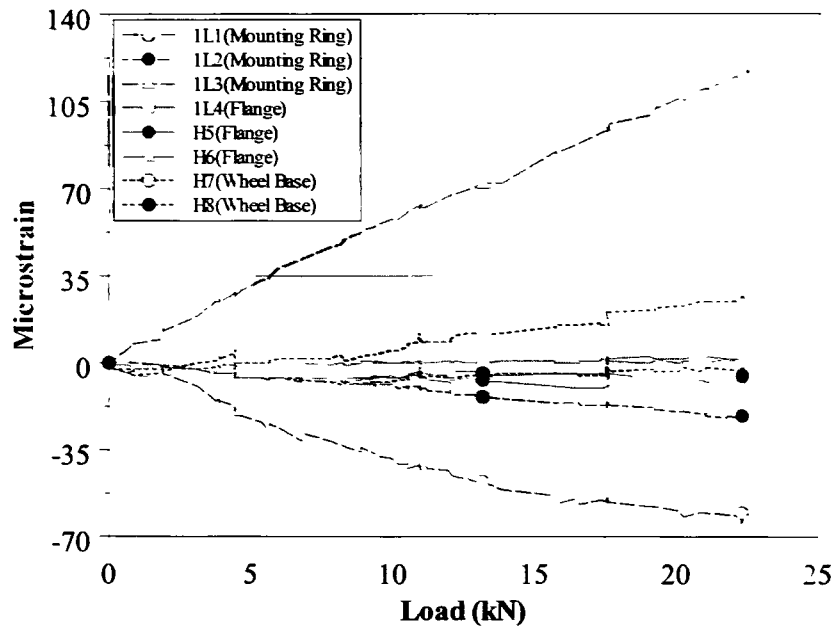


Figure B.4(b). Strain versus load profiles for strain gauge positions (wheel assembly) from the fourth experiment.

APPENDIX C

C.1. Implicit integration scheme

Numerical analyses of the experimental tests were solved utilizing an implicit time integration scheme with in LS-DYNA. The Newmark integration scheme [55] is used in LS-DYNA to solve problems implicitly. The assumptions made for velocity and displacement at any instant of time according to this scheme are presented in equation (C.1) and (C.2) respectively. The velocity at any instant of time is dependent on the velocity and acceleration of the previous timestep and acceleration of the current timestep (Δt). The parameters which influence the displacement as illustrated in equation (C.2) are displacement, velocity, and acceleration of the previous timestep and acceleration of the current timestep.

$$\dot{U}_{t+\Delta t} = \dot{U}_t + [(1 - \delta) \cdot \ddot{U}_t + \delta \cdot \ddot{U}_{t+\Delta t}] \cdot \Delta t \quad (C.1)$$

$$U_{t+\Delta t} = U_t + \dot{U}_t \cdot \Delta t + [(0.5 - \alpha) \cdot \ddot{U}_t + \alpha \cdot \ddot{U}_{t+\Delta t}] \cdot \Delta t^2 \quad (C.2)$$

Appropriate selection of values for α and δ are critical to obtain a stable and accurate solution for any given problem.

Additionally, to solve for displacements, velocities, and accelerations at timestep $t+\Delta t$, the equilibrium equation governing the linear dynamic response of a system of finite elements as represented in equation (C.3) is utilized.

$$[M] \cdot \{\ddot{U}_{t+\Delta t}\} + [C] \cdot \{\dot{U}_{t+\Delta t}\} + [K] \cdot \{U_{t+\Delta t}\} = \{R_{t+\Delta t}\} \quad (C.3)$$

where,

$[M]$ is the mass matrix

$[C]$ is the damping matrix

$[K]$ is the stiffness matrix

$\{R_{t+\Delta t}\}$ is the external force of the system at that instant resulting from body forces, externally applied loads, and forces from contacting entities
 $\{\ddot{U}\}$, $\{\dot{U}\}$ and $\{U\}$ are the vectors to denote nodal accelerations, velocities, and displacements respectively

APPENDIX D

D.1. Explicit time integration scheme

An explicit time integration scheme was utilized to solve the finite element simulations involving fatigue loading of the wheel model implementing the SAE J1992 wheel cornering fatigue test standard. One of the most commonly used explicit time integration schemes is the central difference method. An approximation for acceleration at a time instant 't' based on the central difference method is presented in equation (D.1) [55].

$$\ddot{U}_t = \frac{1}{\Delta t^2} \cdot (U_{t-\Delta t} - 2 \cdot U_t + U_{t+\Delta t}) \quad (\text{D.1})$$

The acceleration at any timestep is dependent on displacement at that current timestep and the displacements of one step before and after the current timestep as illustrated in equation (D.1). An error on the order of Δt^2 is associated with the expansion of acceleration equation. The instantaneous velocity is defined as in equation (D.2) to have the same order of error.

$$\dot{U}_t = \frac{1}{2\Delta t} \cdot (U_{t+\Delta t} - U_{t-\Delta t}) \quad (\text{D.2})$$

The velocity at time 't' is dependent on the displacements of the previous and future timesteps. The equilibrium equation at time instant 't' as in equation (D.3) is further considered to obtain a solution for displacement at $t + \Delta t$. Equations (D.1) and (D.2) are substituted in equation (D.3) and the resulting equation can be used to solve for $U_{t+\Delta t}$ [55].

$$[M] \cdot \{\ddot{U}_t\} + [C] \cdot \{\dot{U}_t\} + [K] \cdot \{U_t\} = \{R_t\} \quad (\text{D.3})$$

where,

$[M]$ is the lumped mass matrix

$[C]$ is the damping matrix

$[K]$ is the stiffness matrix

$\{R_i\}$ is the external force of the system at that instant of time resulting from body forces, externally applied loads, and forces from contacting entities

$\{\ddot{U}_i\}$, $\{\dot{U}_i\}$, and $\{U_i\}$ are the nodal accelerations, velocities, and displacements respectively

An important consideration for explicit time integration scheme is the value for Δt . It is required that this value is smaller than the critical value for timestep (Δt_{cr}) [55].

$$\Delta t \leq \Delta t_{cr} = \frac{l_c}{c} \quad (\text{D.4})$$

where,

l_c is the characteristic length of the smallest element in the finite element assemblage and c is the speed of sound in the corresponding material medium

VITA AUCTORIS

NAME	Vivek Vijayan
PLACE OF BIRTH	Chennai, Tamil Nadu, India
DATE OF BIRTH	February 11 th 1984
EDUCATION	University of Windsor, Windsor, ON, Canada 2006 – 2008 Master of Applied Science (Mechanical) Anna University, Chennai, Tamil Nadu, India 2001 – 2005 Bachelor of Engineering (Mechanical)